

YEAR END TECHNICAL REPORT

September 29, 2020 to September 28, 2021

Chemical Process Alternatives for Radioactive Waste

Date submitted:

December 3, 2021

Principal Investigator:

Leonel E. Lagos, Ph.D., PMP®

Florida International University Collaborators:

Dwayne McDaniel, Ph.D., P.E. (Project Manager)

Anthony Abrahao, M.S.

Aparna Aravelli, Ph.D.

Amer Awwad, M.S., P.E.

Mayren Echeverria Boan, Ph.D.

Shervin Tashakori, Ph.D.

Mackenson Telusma, M.S.

DOE Fellows

Submitted to:

U.S. Department of Energy

Office of Environmental Management

Under Cooperative Agreement DE-EM0005213



Applied Research Center

FLORIDA INTERNATIONAL UNIVERSITY

Addendum:

This document represents one (1) of five (5) reports that comprise the Year End Reports for the period of September 29, 2020 to September 28, 2021 prepared by the Applied Research Center at Florida International University for the U.S. Department of Energy Office of Environmental Management (DOE-EM) under Cooperative Agreement No. DE-EM0005213.

The complete set of FIU's Year End Reports for this reporting period includes the following documents:

Project 1: Chemical Process Alternatives for Radioactive Waste
Document number: FIU-ARC-2020-800012997-04b-009

Project 2: Environmental Remediation Science and Technology
Document number: FIU-ARC-2020-800013918-04b-004

Project 3: Waste and D&D Engineering and Technology Development
Document number: FIU-ARC-2020-800013919-04b-008

Project 4: DOE-FIU Science & Technology Workforce Development Initiative
Document number: FIU-ARC-2020-800013920-04b-017

Project 5: Long-Term Stewardship of Environmental Remedies: Contaminated Soils and Water and STEM Workforce Development
Document number: FIU-ARC-2020-800013922-04b-007

Each document will be submitted to OSTI separately under the respective project title and document number as shown above. In addition, the documents are available at the DOE Research website for the Cooperative Agreement between the U.S. Department of Energy Office of Environmental Management and the Applied Research Center at Florida International University: <https://doeresearch.fiu.edu>

DISCLAIMER

This report was prepared as an account of work sponsored by an agency of the United States government. Neither the United States government nor any agency thereof, nor any of their employees, nor any of its contractors, subcontractors, nor their employees makes any warranty, express or implied, or assumes any legal liability or responsibility for the accuracy, completeness, or usefulness of any information, apparatus, product, or process disclosed, or represents that its use would not infringe upon privately owned rights. Reference herein to any specific commercial product, process, or service by trade name, trademark, manufacturer, or otherwise does not necessarily constitute or imply its endorsement, recommendation, or favoring by the United States government or any other agency thereof. The views and opinions of authors expressed herein do not necessarily state or reflect those of the United States government or any agency thereof.

TABLE OF CONTENTS

TABLE OF CONTENTS.....	i
LIST OF FIGURES	v
LIST OF TABLES	x
PROJECT 1 EXECUTIVE SUMMARY.....	11
MAJOR TECHNICAL ACCOMPLISHMENTS	16
TASK 17: ADVANCED TOPICS FOR HLW MIXING AND PROCESSES	18
Subtask 17.2: Evaluation of Pipeline Flushing Requirements for HLW at Hanford and Savannah River Site	18
Subtask 17.2: Introduction	18
Subtask 17.2: Objectives.....	19
Subtask 17.2.: Methodology	19
Subtask 17.2: Results and Discussion.....	23
Subtask 17.2: Conclusions	28
Subtask 17.2: References	28
TASK 18: TECHNOLOGY DEVELOPMENT AND INSTRUMENTATION EVALUATION.....	30
Subtask 18.2: Development of Inspection Tools for DST Primary Tanks	30
Subtask 18.2: Introduction	30
Subtask 18.2: Objectives.....	30
Subtask 18.2.1: Preparation for Deployment of Miniature Rover at Hanford.....	31
Subtask 18.2.1: Methodology	31
Subtask 18.2.1: Results and Discussion.....	36
Subtask 18.2.1: Conclusions	36
Subtask 18.2.1: References.....	36
Subtask 18.2.4a: 6-inch Crawler Development	37
Subtask 18.2.4a: Methodology	37
Subtask 18.2.4a: Results and Discussion.....	45
Subtask 18.2.4a: Conclusions	48
Subtask 18.2.4a: References	48
Subtask 18.2.4b: Crawler Development for SST Lateral Gamma Scans	49
Subtask 18.2.4b: Methodology	49
Subtask 18.2.4b: Results and Discussion.....	54
Subtask 18.2.4b: Conclusions	57

Subtask 18.2.4b: References 57

Subtask 18.3: Evaluation of Coatings for the H-Canyon Exhaust Tunnel.....58

 Subtask 18.3: Introduction 58

 Subtask 18.3: Objectives..... 59

 Subtask 18.3.1: Development and Construction of an Omnidirectional Robotic Mobile Platform..... 59

 Subtask 18.3.1: Methodology 59

 Subtask 18.3.1: Results and Discussion..... 62

 Subtask 18.3.1: Conclusions 64

 Subtask 18.3.1: References 64

 Subtask 18.3.2: Development of a Coating Application System..... 65

 Subtask 18.3.2: Methodology 65

 Subtask 18.3.2: Results and Discussion..... 66

 Subtask 18.3.2: Conclusions 67

 Subtask 18.3.2: References 67

Subtask 18.4: Long-Term Surveillance of Nuclear Facilities and Repositories
 using Mobile Systems68

 Subtask 18.4: Introduction 68

 Subtask 18.4: Objectives..... 68

 Subtask 18.4.1: Surveillance Literature Review and Assessment 68

 Subtask 18.4.1: Methodology 69

 Subtask 18.4.1: Results and Discussion..... 71

 Subtask 18.4.1: Conclusions 82

 Subtask 18.4.1: References 83

TASK 19: PIPELINE INTEGRITY AND ANALYSIS84

 Subtask 19.1: Pipeline Corrosion and Erosion Evaluation84

 Subtask 19.1: Introduction 84

 Subtask 19.1: Objectives..... 85

 Subtask 19.1.1: Evaluation of SRNL Stainless Steel Coupons for Erosion Testing 85

 Subtask 19.1.1: Methodology 85

 Subtask 19.1.1: Results and Discussion..... 87

 Subtask 19.1.1: Conclusions 91

 Subtask 19.1.1: References 92

Subtask 19.1.2: Design and Development of a Bench Scale Flow Loop for Caustic Simulant Testing..... 92

Subtask 19.1.2: Methodology 92

Subtask 19.1.1: Results and Discussion..... 94

Subtask 19.1.2: Conclusions 97

Subtask 19.1.2: References 97

Subtask 19.2: Evaluation of Nonmetallic Components in the Waste Transfer System97

Subtask 19.2: Introduction 97

Subtask 19.2: Objectives..... 98

Subtask 19.2.: Phase 3 Testing for HIHTL..... 98

Subtask 19.2: Methodology 98

Subtask 19.2: Results and Discussion..... 100

Subtask 19.2: Conclusions 101

TASK 20: Corrosion Protection and Characterization of EM Infrastructure102

Subtask 20.1: Evaluation of Coatings for the H-Canyon Exhaust Tunnel.....102

Subtask 20.1: Introduction 102

Subtask 20.1: Objectives..... 102

Subtask 20.1.1: Execution of Test Plan for Aging Concrete Surfaces 103

Subtask 20.1.1: Methodology 103

Subtask 20.1.1: Results and Discussion..... 105

Subtask 20.1.1: Conclusions 110

Subtask 20.1.1: References 110

Subtask 20.1.2: Development and Execution of a Test Plan for Coatings Evaluation 111

Subtask 20.1.2: Methodology 111

Subtask 20.1.2: Results and Discussion..... 113

Subtask 20.1.2: Conclusions 114

Subtask 20.2: Corrosion Evaluation of Steel Canisters for Hanford Integrated Disposal Facility114

Subtask 20.2: Introduction 114

Subtask 20.2: Objectives..... 114

Subtask 20.2.1: Literature Review for Steel Corrosion Study at Hanford..... 114

Subtask 20.2.1: Methodology 114

Subtask 20.2.1: Results and Discussion..... 115

Subtask 20.2.1: Conclusions 120

Subtask 20.2.1: References 120

Subtask 20.2.2: Development of a Test Plan and Initial Testing for the Steel Corrosion Study
..... 121

Subtask 20.2.2: Methodology 121

Subtask 20.2.2: Results and Discussion..... 124

Subtask 20.2.2: Conclusions 124

CONFERENCE PARTICIPATION, PUBLICATIONS, AWARDS &
ACADEMIC MILESTONES125

ACKNOWLEDGEMENTS127

APPENDIX.....128

LIST OF FIGURES

Figure 1. CAD Model of the 165-foot pipeline used for flushing experiments.....	19
Figure 2. Constructed 165-foot pipeline used for flushing experiments.	20
Figure 3. (a) CAD Model of 330-foot flushing loop used for second round of testing; (b) Assembled 330-foot flushing loop.....	21
Figure 4. (Left) HopeWind VFD; (Right) AMT 427B-95 15 HP Slurry Pump.	22
Figure 5. (Left) Krohne Optimass 1000 Coriolis Meter; (Right) VEGAPULS 11 level sensor...	22
Figure 6. Density-mass flow plots for 10 % vol (top), 15 % vol (middle), and 20 % vol (bottom) kaolin-water simulants in the fully-flooded condition.....	24
Figure 7. Density-mass flow plots for 10 % vol (top), 15 % vol (middle), and 20 % vol (bottom) kaolin-water simulants in the gravity-drained condition.	25
Figure 8. Density-mass flow plots for 15 % vol at one-week of sedimentation (top) and at two- weeks of sedimentation (bottom) of kaolin-water simulants for the gravity-drained condition.	26
Figure 9. Density-mass flow plots for 15 % vol at one day sedimentation of kaolin-water simulants for the gravity-drained pulsation mode.....	26
Figure 10. Current miniature rover design.....	31
Figure 11. Magnetic wheels.....	31
Figure 12. Wheel fender/scoops.	32
Figure 13. TPU material installed in frame.	32
Figure 14. Final control box design.	32
Figure 15. Durability test mockup.	33
Figure 16. Tether details.	35
Figure 17. Oblique/Blunt weld seam.	35
Figure 18. Corroded surface test.	36
Figure 19. Leak detection systems at Hanford's DSTs.	37
Figure 20. Proposed inspection.....	38
Figure 21. Child inspection rover.	38
Figure 22. Magnetic detaching mechanism.	38
Figure 23. Inspection rover overall schematic.....	39
Figure 24. Instrumentation electronics schematic.	40
Figure 25. Onboard printed circuit board.	40
Figure 26. Instrumentation rover current model footprint.....	40
Figure 27. Peristaltic delivery pipe crawler prototype.....	41

Figure 28. Drainpipe existing sediments and buildup. 41

Figure 29. Housing module..... 42

Figure 30. Overhead deployment ramp. 42

Figure 31. Retractable deployment ramp..... 43

Figure 32. Track-driven delivery pipe crawler conceptual design. 43

Figure 33. Tank suspension design..... 43

Figure 34. Model of the rover in housing module with deployable ramp. 44

Figure 35. DST's full-scale sectional mockup. 44

Figure 36. FIU's DST's full-scale sectional mockup..... 45

Figure 37. Child inspection rover. 46

Figure 38. Magnetic detaching mechanism. 46

Figure 39. Instrumentation rover current prototype..... 46

Figure 40. Retractable deployment ramp prototype. 47

Figure 41. Tank track prototype..... 47

Figure 42. Housing module with ramp prototype. 47

Figure 43. Control box's GUI. 48

Figure 44. Single shell tank's laterals..... 49

Figure 45. Gamma logging sonde detectors. 50

Figure 46. FIU's existing 3-inch crawler. 50

Figure 47. Proposed demonstration deployment at Hanford. 51

Figure 48. Crawler current design. 51

Figure 49. Redesigned intermodular flexible connection bellows..... 52

Figure 50. Tether quick-disconnect for quick detachment. 52

Figure 51. Crawler's power over internet data transmission..... 53

Figure 52. Schematic of IMUs communication..... 53

Figure 53. Pipe Crawler Full-Scale Mockup. 54

Figure 54. Current pipe crawler prototype..... 54

Figure 55. Improved guides. 54

Figure 56. Electronics module with a forward-facing camera and range finder. 55

Figure 57. Pipe crawler bench-scale testing. 55

Figure 58. Pipe crawler portable control box..... 56

Figure 59. Tether reel and potential slip-ring. 56

Figure 60. Ethernet slip-ring integration..... 57

Figure 61. Tether assembly..... 57

Figure 62. Single EDF based platform. 60

Figure 63. Control system breakdown for the single EDF platform..... 60

Figure 64. Multi-fan omnidirectional platform..... 61

Figure 65. Top view of multi-fan platform with control box unit. 61

Figure 66. Front view of omnidirectional platform. 61

Figure 67. Completed control system unit..... 62

Figure 68. Self-locking safety mechanism secured on testing wall..... 62

Figure 69. Power delivery setup to multi-fan platform..... 63

Figure 70. Smooth-like or pristine surface condition. 63

Figure 71. Rough wall condition with surface debris. 63

Figure 72. Multi-fan system with 3D printed chassis. 64

Figure 73. Multi-fan system with chassis fabricated using carbon fiber sheets. 64

Figure 74. CAD design of coating mechanism..... 65

Figure 75. Timing belt and pulley-based coating application system. 65

Figure 76. Lead screw-based coating application system..... 65

Figure 77. Partially assembled coating mechanism with portable power supply..... 65

Figure 78. Enclosure unit for the secondary axis motor setup..... 66

Figure 79. Internal configuration of the gear motor setup for the second axis. 66

Figure 80. Coating mechanism. 66

Figure 81. New gear motor module..... 66

Figure 82. Hanford's Tank Farm retrieval operations in September 2016 (left) and 2018 (right).69

Figure 83. Mobile platform integration. 70

Figure 84. FIU's mobile platforms..... 71

Figure 85. Indoor (left) and outdoor (right) colored point cloud topographic maps. 71

Figure 86. High density colored point cloud from Intel Realsense D435 Depth Camera. 72

Figure 87. Improved object detection. 72

Figure 88. Environmental mapping using the installed depth camera..... 73

Figure 89. Preliminary hallway map..... 73

Figure 90. Improved captured map by fused data from a 3D camera..... 74

Figure 91. RTK GPS (left), mobile unit (center), and fixed base station (right)..... 74

Figure 92. Waypoint autonomous surveillance. 75

Figure 93. Waypoint navigation algorithm preliminary test..... 75

Figure 94. Mid-range LiDAR integration. 76

Figure 95. Original ICP point cloud (left) and improved map fusing IMU (right). 76

Figure 96. Captured maps from FIU's corridors. 77

Figure 97. Closed loop failure in the localization algorithm. 77

Figure 98. Implemented state machine using SMACH library..... 78

Figure 99. FIU's all-terrain platform with a manipulator..... 78

Figure 100. Handheld mapping device and captured raw datasets. 79

Figure 101. Processed data after cleaning and registration..... 79

Figure 102. Path of different sources of odometry. 79

Figure 103. FIU's Robotics Laboratory original point cloud (left) and reconstructed surfaces (right). 80

Figure 104. Original (left) and improved (right) "boxy" handheld mapping device. 80

Figure 105. Surface variation histogram a point cloud before (left) and after (right) preprocessing. 81

Figure 106. FIU's Robotics Laboratory VR headset system..... 81

Figure 107. Preliminary virtual reality immersion tests. 82

Figure 108. a) SRNL coupon b) dimensions and c) experimental pipe loop..... 86

Figure 109. Borescope images of the coupons in the pipe loop. 86

Figure 110. a) UT sensor calibration and b) real-time coupon thickness measurement..... 87

Figure 111. Eroded Coupon surfaces removed from the elbow and bottom sections of the pipe. 88

Figure 112. Results of Coupon Erosion Test 1 and Test 2. 90

Figure 113. Results of Coupon Erosion Test 3 and Test 4. 91

Figure 114. Results of Coupon Erosion Test 5 and Test 6. 91

Figure 115. a) Bench scale loop development CAD drawing and b) assembled loop..... 93

Figure 116. a) Bench scale loop, b) water testing and c) pipe leak. 94

Figure 117. SRNL coupon immersion tests initial (Day 1) (left) and current (Day 35) (right).... 95

Figure 118. Visual corrosion inspection of the CS and SS coupons (2M). 95

Figure 119. Mass change in 2M and 6M solutions..... 97

Figure 120. HIHTL burst pressure test apparatus..... 99

Figure 121. Tensile strength test apparatus..... 99

Figure 122. Tensile strength results for dog-bones aged with 25% NaOH. 100

Figure 123. Hose burst pressure for specimens aged with 25% NaOH..... 100

Figure 124. Schematic of test setup for concrete exposition to acid solutions. 104

Figure 125. Comparative images of the top view of concrete specimens before and after enhanced aging conditions of Test 7, Test 8, Test 11 and Test 12. The arrow on Test 11 points to the exposed rebar. 106

Figure 126. Images of the top view of concrete specimens before and after the end of each standard aging cycle of Test 5, Test 6, Test 9 and Test 10..... 108

Figure 127. XRD spectra of concrete matrix samples before (reference) and after (Test 5 and Test 7) aging. 1-Silicon oxide (Quartz), SiO₂, 2-Calcium hydroxide (Portlandite), Ca(OH)₂ and 3-Calcium sulfate hydrate (Gypsum), CaSO₄(H₂O)₂. 110

Figure 128. Features of the Integrated Disposal Facility [3]. 116

Figure 129. Schematic of the crevice corrosion [7]. 118

Figure 130. Large areas of macroscopic pitting on lid surface of B-25 container [10]. 119

Figure 131. Coating blisters on the surface of B-25 container (a) Intact blisters, (b) broken blisters, (c) broken blisters showing intact primer [10]. 120

Figure 132. Experimental setup (left) and the sample (right) for electrochemical measures. 123

Figure 133. Schematic of the Faraday cage. Image of similar cage (left), Side view (middle) and front view (right). 124

LIST OF TABLES

Table 1. Flush-to-Line Volume Ratio Results, One-Day Sedimentation 27

Table 2. Flush-to-Line Volume Ratio Results, Variable Sedimentation and Pulsation..... 27

Table 3. Heating the Channel for Two Hours..... 34

Table 4. Temperature Drop after Removing One Fan 34

Table 5. Erosion Test results for SRNL Coupons..... 87

Table 6. SRNL Coupon Test Results (Images)..... 88

Table 7. Coupon Geometry and Weight Conditions (Pre-Test) 89

Table 8. Coupon Geometry and Weight Conditions (Post-Test)..... 89

Table 9. Test Matrix for the Engineering Scale Coupon Testing 90

Table 10. Test Matrix for Salt Simulant Testing of the SRNL Coupons..... 93

Table 11. Static Immersion Test Results (Test 1)..... 95

Table 12. Static immersion visual test results of the SRNL coupons. 96

Table 13. pH Variation in 2M, 4M and 6M Solutions..... 96

Table 14. Test Plan for Accelerated Aging of Concrete 103

Table 15. Test plan for the Accelerating Aging of Coatings 111

Table 16. Details of Bench-Scale Testing Measurements 113

Table 17. Vadose Zone Pore Water Simulant [5] 117

Table 18. Test Matrix for Corrosion Study of Canister/Container Materials 122

PROJECT 1 EXECUTIVE SUMMARY

The Department of Energy's (DOE's) Office of Environmental Management (EM) has a mission to clean up the contaminated soils, groundwater, buildings and wastes generated over the past 60 years by the R&D and production of nuclear weapons. The nation's nuclear weapons complex generated complex radioactive and chemical wastes. This project is focused on tasks to support the safe and effective storage, retrieval and treatment of high-level waste (HLW) from tanks at Hanford and Savannah River sites. The objective of this project is to provide the sites with modeling, pilot-scale studies on simulated wastes, technology assessment and testing, and technology development to support critical issues related to HLW retrieval and processing. Florida International University (FIU) engineers work directly with site engineers to plan, execute and analyze results of applied research and development.

Although a number of tasks have been initiated and completed over the course of the cooperative agreement, at the end of this past year, there were 4 active tasks. These tasks are listed below and this report contains a detailed summary of the work accomplished for FIU's Performance Year 1.

Task 17: Advanced Topics for HLW Mixing and Processes

In U.S. Department of Energy (U.S. DOE) complexes, pipelines that carry high-level radioactive waste must be properly flushed to ensure proper cleaning without any residue. Current guidelines exist that establish a minimum flush volume and velocity of water required for post-transfer flushing operations to achieve a satisfactory cleaning of pipelines. However, the Defense Nuclear Facilities Safety Board (DNSFB) has indicated the need for vigorous investigations on the technical basis for prescribing flush velocity and flush volumes in pipelines. Consequently, further studies are being investigated that will significantly assist the U.S. DOE in waste remediation by optimizing the operational conditions that will assist in minimizing the flush volume and consequent downstream waste, which will in turn assist these DOE waste remediation sites by preserving tank storage, preventing additional waste processing, and minimizing dilutions and changes to waste chemistry.

To perform these investigations, a 165-foot, 3-inch carbon steel experimental pipe loop capable of expansion was developed and constructed at Florida International University (FIU) to study the flushing of non-Newtonian slurries. The testbed was designed to create sediment beds of various materials and bed heights to investigate parameters that affect the efficiency of flushing operations at various concentrations and with various flush volume and flush modes to determine the effect of flush volumes for each configuration. Testing was then done with various kaolin-water slurry simulant concentrations with repeatable sediment beds inside the pipeline for fully-flooded conditions with one day sedimentation, gravity-drained conditions with one day, one week, and two-week sedimentation, and pulsation. The objective is to find flush velocity values/modes using repeatable sediment beds inside the pipeline for the fully-flooded and gravity-drained conditions which lead to satisfactory cleaning of transport lines of varying length with a minimum amount of flush water consumption.

This report presents the efforts towards flush analyses to determine the efficiency of flushing with the varied configurations of the 165-foot loop. Results showed that the fully-flooded conditions with one day sedimentation, gravity-drained conditions with one day, one week, and two week sedimentation, and gravity-drained pulsation flush modes utilized approximately 1.05 – 1.17 flush-to-line volume (FTLV). In addition, the loop was extended to 330 feet to study the effects of pipe

length of FTLV ratios by comparing the FTLV results from the 330-foot experiments to the FTLV results from the 165-foot experiments.

Task 18: Technology Development and Instrumentation Evaluation

Integrity issues in the double-shell tanks (DST) at Hanford have motivated the need for developing innovative tools that can provide information regarding the health of the tanks. These issues include the primary linear failure of AY-102 and recent concerns of thinning in the DST secondary liners. Other concerns include erosion or corrosion on transfer lines and processing pipes. In recent years, FIU has supported DOE-EM by developing tools that can assist in understanding the health of tanks and the waste transport system at Hanford.

FIU has developed a miniature rover that can be deployed through small risers and gain access to refractory slots in the Hanford DSTs. The rover traverses through the slots on the primary liner, via magnets to avoid debris in the slots. The redesigned rover uses bevel gears in order to create right angle motors which allows for side-by-side motorized wheels that give the unit enough clearance height in its middle so that it can traverse over weld seams on the liner. Using bevel gears to make right angle motors makes it possible to utilize micro motors with higher stall torques (140 oz.in). In addition, the design of the control box of the rover was finalized and assembled. The new control system makes it possible to utilize stronger DC motors and allows for the use of a longer tether cable.

Prior to deploying the mini rover at Hanford, FIU worked with engineers at Washington River Protection Solution (WRPS) to develop a test plan that introduces the rover to harsh and strenuous environments in FIU's DST mockup. The test plan is comprised of four tests that include a durability test, emergency retrieval test, weld seam test, and corrosion test. Each test is designed to challenge the rover in conditions that could be encountered onsite during the actual deployment.

To address the secondary liner issue of the DSTs, FIU has continued to develop a marsupial robotic system. It includes a 6-inch peristaltic pipe crawler that operates similar to the previous pipe crawlers developed at FIU that houses a small rover. The objective for this system is to navigate through the 6-inch drain lines, and deploy the rover at the entrance of the drain slots. The rover is designed with a scissor lift chassis that allows it to navigate on the tank floor or in the slots. A deployment module has also been developed to house the rover until the crawler reaches the tank foundation from the drain line. The module sits at the front of the crawler and provides the means for the rover to enter into the drain slots.

FIU was also asked to investigate the use of an existing 3-inch crawler for its ability to traverse through 3-inch diameter lines underneath single shell tanks (SSTs) and potentially carry a radiation sensor that can be used to inspect for leaks under the tanks. The crawler is a pneumatic system that navigates through pipes using multiple modules that move with a peristaltic-type motion. Multiple aspects of the crawler were upgraded that included adding guides on the modules and simplifying the control panel. A mockup of the SST line was also developed at FIU and the unit has been able to transvers through the bend and straight sections.

In addition, FIU is supporting the Savannah River Site (SRS) facility by investigating technologies to evaluate the H-Canyon exhaust tunnel for degradation and potentially assist in avoiding further degradation. Robotic inspections of the tunnel revealed significant degradation of the reinforced concrete structure that was primarily associated with acid attack, and could compromise the

structural stability of the tunnel. Thus, the identification and evaluation of potential coatings that could be applied on the degraded walls to mitigate and prevent further degradation is of significant interest to the Department of Energy and the Savannah River representatives. To assist in this effort, FIU is investigating the development of a platform to deploy the potential coatings. A wall crawler system is being developed to climb the walls of the canyon tunnel and will house a mechanism to apply the protective coating. Different adhesion mechanisms have been evaluated and a ducted fan has been selected to provide the adhesion force necessary to adhere to the jagged walls of the tunnel. A prototype has been developed and has proven to be capable of navigating up the walls as well as on the ceiling. A spray mechanism is also being developed that could potentially be used to apply the coatings that are being considered.

FIU has also recently initiated tasks related to the characterization of EM infrastructure. These tasks will assist DOE-EM and site engineers with understanding various aspects of EM-related sites by using autonomous systems to gather information related to safety and the environmental conditions. Robotic platforms will be developed with an array of sensors that can autonomously provide radiation, LiDAR and other types of maps of the sites while keeping personnel out of harm's way.

Task 19: Pipeline Integrity and Analysis

Structural health of waste transfer and storage infrastructure is of utmost importance to DOE and communities surrounding the active sites. A Fitness-for-Service (FFS) program for the Waste Transfer System has been implemented by the U.S. Department of Energy (DOE) through the contractor - Washington River Protection Solutions (WRPS), for the purposes of evaluating and quantifying the structural integrity of critical components such as the pipelines, tanks and tank farm waste transfer system. The purpose of the program was to inspect primary piping, encasements, and jumpers for corrosion/erosion, which has been accomplished in the previous years. Various sensor systems have been investigated, down selected and tested in the past. These included the evaluation of the Ultrasonic sensor system from Permasense for the measurement accuracy and performance under high temperature and humidity conditions and studying the feasibility of radiation effects on the Permasense ultrasonics sensors. An additional sensor system was also investigated for the leak and fault detection in pipe loops using the fiber optic electro acoustic principles. This system is called the Fiberstrike Sensor System from Cleveland Electric Limited (CEL). This task had stemmed due to the collaborative talks between DOE, industry (sensor vendor (CEL)), WRPS and FIU. The sensor vendor leased the system to FIU in order to investigate the faults and leak detection in carbon steel pipe loops and validate their technology on an engineering scale, for potential deployment at the DOE sites. FIU conducted the experiments and results indicated that the system was successfully able to detect pipeline faults, leaks, pump malfunctions and valve blockage issues related to the waste transfer system and is capable of the cold test demonstrations at the sites. Further, SRNL has tasked FIU with lab, bench and engineering scale testing of their patented mass loss coupon technology for small scale wear detection in pipes and transfer lines. The coupons are used to measure slight changes in mass loss due to erosion and to quantify the thinning in the pipe diameter on a precise level using the UT pencil sensor probes. The coupons were able to provide the visual erosion when inspected under the microscope/SEM. This past year, the task concentrated on completing the carbon steel coupon and stainless coupon testing on the engineering scale loop and talks were conducted on the caustic simulant testing. Based on the customized simulant recipe provided by SRNL scientists, a bench scale pipe loop has been designed and constructed at FIU. The loop will use chemical simulants

for corrosion testing of the SRNL carbon and stainless-steel coupons. Simultaneously, static immersion testing of the coupons has been initiated and 6 months of data (visual, mass change and thickness) has been collected for corrosion evaluation of the coupons. Dynamic and static corrosion testing will be continued this year.

Structural integrity of non-metallic materials is also being investigated under the current research work. Nonmetallic materials used in the Hanford Site Tank Farm waste transfer system include the inner primary hoses in the hose-in-hose transfer lines (HIHTLs), Garlock® gaskets, ethylene propylene diene monomer (EPDM) O-rings, and similar other nonmetallic materials. These materials are exposed to radiation, caustic solutions and elevated temperature and pressure stressors. While the individual effect of these stressors has been well established, their combined effect is of significance to the Hanford site. FIU has been supporting this task by developing a test loop and testing the non-metallic materials under simultaneous stressor exposures.

The objective of this task is also to provide the Hanford Site with data obtained from experimental testing of the hose-in-hose transfer lines, Teflon® gaskets, EPDM O-rings, and other nonmetallic components used in their tank farm waste transfer system under simultaneous stressor exposures. The experiments will be limited to various combinations of simultaneous stressor exposure to caustic solutions, high temperatures and high pressure. Evaluation of baseline materials will be conducted for comparison to materials that have been conditioned with the various simultaneous stressors.

Previous testing included aged HIHTL and material coupons for 6 months and 1 year using elevated temperatures and exposure to caustic material as well as exposure to water only at 170°F for 1 year. The mechanical and material properties of the samples were characterized and compared with those of the unexposed samples (baseline). Evaluations included burst pressure tests of the EPDM hose-in-hose transfer lines and material tensile strength tests of EPDM dog-bone coupons. It was observed that both the tensile strength of the EPDM material dog-bones and the burst pressure of the HIHTLs significantly decreased with the increasing temperature and increasing exposure time. This phase of testing includes aging of HIHTL and EPDM dog-bone specimens at various concentrations of NaOH as well as water only at the elevated temperatures. Four test loops were developed at FIU allowing for the aging of HIHTL as well as dog-bone specimens utilizing 6.25%, 12.5% and 25% NaOH and only water respectively at 170°F.

This task will provide information that will assist engineers with understanding the wear rates in metal pipes and transfer lines along with the effect of various stressors on nonmetallic components. The research will aid in determining the remaining useful life of both metallic and non-metallic components by establishing more detailed/accurate guidelines and avoiding unexpected failures in transfer lines.

Task 20: Corrosion Protection and Characterization of EM Infrastructure

As noted in Task 18, FIU is assisting with investigations that can assist in the mitigation of degradation of the concrete walls in the H-Canyon exhaust tunnel. The degradation observed could compromise the mechanical strength of the structure. Hence, the search for solutions to mitigate and prevent further degradation is necessary. The application of a protective coating on the degraded tunnel walls could mitigate and prevent further degradation, which constitutes the main goal of the investigation. The investigation has been divided into different phases: 1) development and evaluation of aged concrete under accelerated aging conditions (preliminary results included

in this report) and, 2) evaluation of potential coatings applied on aged and non-aged concrete under accelerated aging conditions.

During last year, efforts were focused on the development and evaluation of aged and non-aged concrete surfaces through accelerated aging conditions and the development of a test plan for the evaluation of potential coatings for the protection of the HCAEX tunnel. In order to do this, a comprehensive test plan for the evaluation of the concrete surfaces was developed and executed. Also, accelerated aging procedures, combining the action of acid solutions, erosion, aging mode and other parameters, were developed and implemented. In addition, based on the literature review findings and preliminary aging tests, a test plan for the evaluation of potential coatings was developed. Major findings during this year included the development and characterization of aged concrete surfaces with protruded aggregates, exposed rebar and chemical damage. These surfaces will be the substrate to evaluate potential coatings. Also, accelerated aging procedures for concrete degradation were designed and tested. Finally, potential coatings for the tunnel protection were identified and a test plan to evaluate the coatings was developed.

FIU is also working on a new task with the Hanford site. A current challenge for DOE and relevant DOE sites is to understand the durability of the steel canisters/containers that will contain low-activity waste (LAW) and secondary waste forms, encapsulated in glass and grout respectively, and that will be placed within the Integrated Disposal Facility (IDF) at Hanford. Currently, corrosion data of the steel and weld regions of the canisters at Hanford that is exposed to groundwater is limited. In addition, there is limited information on groundwater in contact with waste forms. The primary technical need is to study the corrosion rate of the steel canister's exterior that is exposed to Hanford groundwater and determine how well it shields the waste form that is inside the canister from exposure. During last year, efforts were concentrated on conducting a literature review for steel corrosion at Hanford and the development of a test plan. The literature review for the steel corrosion study was completed and the main corrosion mechanisms of the typical canister and container materials were identified and studied. A recipe for the preparation of Hanford groundwater in the Integrated Disposal Facility, where the canisters will be stored, was found and reviewed and will be used for the corrosion testing. A test plan for the corrosion study of potential materials for the canister/container was prepared. Also, chemicals and materials were procured for the beginning of electrochemical testing of canister materials and initial samples of 304 SS were prepared for the beginning of testing.

MAJOR TECHNICAL ACCOMPLISHMENTS

Task 17: Advanced Topics for HLW Mixing and Processes

- Testing was completed for 10, 15 and 20% Kaolin/water slurries for both fully-flooded and gravity-drained conditions. Results indicate that a maximum volume of 1.1 - 1.2 of the line volume is needed to completely flush the line.
- The loop was expanded to 330-feet and improvements to the loop's data acquisition unit were completed.

Task 18: Technology Development and Instrumentation Evaluation

- A marsupial crawler system is being developed for the inspection of the secondary liner of DSTs at Hanford. The crawler has been optimized after testing in a 6-inch bench scale mockup. A rover is also being finalized that can traverse on the bottom of the tank or on with the drain slot underneath the secondary liner. The rover will be deployed from the 6-inch crawler when the system traverses through the drain line and reaches the foundation drain slots.
- A miniature rover was developed and deployed in a DST at Hanford to assist in understanding the health of the primary liners. Based on feedback from the testing, modifications were made to the unit that included incorporating a flexible chassis, moving the magnets to the wheels and integrating a mechanism to remove the rust as it accumulates. The plan is to redeploy the system in early spring.
- A 3-inch robotic crawler has been improved for use in navigating through the single shell tank transverse lines that sit under the tanks. The intention is for the crawler to navigate through the line, carrying a radiation sensor that can be used to assist in determining where leaks have occurred in the SSTs. The unit is set to be deployed in early spring.
- A wall crawler that utilizes a ducted fan has been developed to assist in addressing issues with the H-Canyon exhaust tunnel. The crawler was capable of navigating on corroded concrete vertical surfaces. Based on this concept, a larger crawler was developed using 5 ducted fans with a much larger payload capacity.

Task 19: Pipeline Integrity and Analysis

- Erosion tests on the engineering scale test loop using SRNL coupons have been completed. Both carbon steel and stainless-steel mass loss coupons have been evaluated for in-situ erosion characteristics based on material and simulant particle sizes and concentrations using sand water mixtures. Results indicate that SRNL coupons are capable of detecting minute erosion levels and can be used as in-situ erosion probes in the waste transfer systems without interrupting the flow.
- Static immersion testing of the SRNL coupons to investigate chemical corrosion have been initiated. The recipe developed by SRNL scientists provides realistic waste characteristics for accurate caustic testing.
- Design and development of a customized bench scale test loop for chemical corrosion tests using SRNL coupons and other materials has been completed. The pipe loop is a closed system made of 2- and 3-inch diameter pipe sections to circulate chemical simulants between a tank and a pump.
- Completed one year aging of HIHTL and EPDM dog-bone specimens.

- Began burst pressure testing of HIHTL as well as tensile strength of EPDM dog-bone specimens.

Task 20: Corrosion Protection and Characterization of EM Infrastructure

- Concrete specimens similar to the HCAEX tunnel walls were developed and characterized.
- Aged concrete surfaces with protruded aggregates, exposed rebar and chemical damage were developed, evaluated and will be the substrate to evaluate coatings.
- Accelerated aging procedures for concrete degradation were designed and tested.
- Potential coatings for the tunnel protection have been identified.
- A literature review for the steel corrosion study was completed.
- A test plan for the corrosion study of potential materials for the canister/container was prepared.
- A potentiostat for getting electrochemical corrosion data of canister materials was procured.
- Chemicals and materials were procured for the beginning of electrochemical testing of canister materials.
- Initial samples of 304 SS were prepared for the beginning of testing

TASK 17: ADVANCED TOPICS FOR HLW MIXING AND PROCESSES

Subtask 17.2: Evaluation of Pipeline Flushing Requirements for HLW at Hanford and Savannah River Site

Subtask 17.2: Introduction

U.S. DOE sites across the Department of Energy – Environmental Management (DOE-EM) complex must abide by guidelines that establish a minimum flush volume and flush velocity of water required to ensure proper cleaning of transfer pipelines that carry high-level radioactive waste without any residue that would be left behind during the transfer process. These guidelines are meant to establish these minimum values to ensure that the post-transfer flushing operations result in a satisfactory cleanliness of the pipes. However, despite these guidelines, the Defense Nuclear Facilities Safety Board (DNSFB) has indicated a need for vigorous investigations on the technical basis for prescribing flush velocity in pipelines [1] because, for optimal performance at the Department of Energy sites, pipelines that transfer radioactive waste must be operated above the critical velocity of fluid flow to prevent residual formations from solids sedimentation within the pipe bed. These formations can form partial or full granular plugs and build-up of H-gasses, which result in process upsets, costly delays and potential need for line repair or line abandonment, equipment overloads, or possible destruction of equipment such as a rupture at the pump or within the pipeline. The pretreatment facility design strategy requires that each slurry transfer in the process lines be followed by a flush with water to minimize the chances of a partial or full line plug.

Previous reports related to pipeline flushing of several simulants were reviewed. The studies revealed that, in several tests, the minimum required flush volumes were more than minimum required values provided by certain design guidelines. In a study at Pacific Northwest National Laboratory (PNNL), the flush velocity that was recommended for a slurry up to 30 Pascals of yield stress is 10 ft/sec to adequately flush the system. Flush velocities in the pipeline exceeded the maximum velocity stated in the flushing guidelines [2] that ensure that the interior of the pipeline does not erode due to the solid particles within the slurry that are agitated during transfer and flushing. In the same study, it was demonstrated that “a flush-to-line volume ratio (FTLV) of 3 was needed to remove sediment bed whereas the design guide provides a minimum flush-volume ratio of 1.7” [3]. In the design guidelines and according to the study, the minimum flush volume within the guidelines was prescribed at 1.7 times the volume of the pipeline, whereas the actual required flush volumes to ensure the pipelines are properly cleaned was closer to nearly triple the amount.

This effort is intended to determine effective flushing operations using a minimal amount of water usage and provide additional guidelines in support of recently developed flushing standards indicated by TFC-ENG-STD-26 [4]. Successful execution of the current work requires creation and characterization of sediment beds, flushing in different modes, and evaluation of operational effectiveness through measurement of post-flush pipeline residues. To extend previous flushing studies, the focus was to create different case studies targeting different materials and pipe lengths. In each round of testing, focus was on influential parameters set for one simulant in a fixed pipe length. These parameters include varying the initial conditions of the sediment such as the concentration of the solid and its corresponding settlement height, settlement time of one day, one

week, and two weeks, flush operation (fully-flooded and gravity-drained), and pump operation mode (continuous and pulsation).

Subtask 17.2: Objectives

The objective of this effort is to provide a technical basis for flush volume used in the waste transfer process. This includes:

- Implementing optimal flush operations that minimizes waste production, pipeline erosion, and ensures satisfactory cleaning of pipelines based on an established criterion for thorough discussions between FIU and personnel at the waste sites and national laboratories.
- Developing a correlation for flush parameters based on characteristics of the system at the start of flushing (initial conditions). Data and correlations will be useful for determination of pumping requirements improving existing guidelines.

Subtask 17.2.: Methodology

Test Loop

The experimental set up consists of a test loop composed of 3-inch schedule 40 carbon steel pipes and fittings (Figure 1 and Figure 2). This test loop can perform various functions such as slurry circulation, pump cleaning, flushing, sediment and water retrieval, filtration, and post-flush circulation. The pipeline was sloped at the rate of 0.15% (to emulate conditions at Hanford site and facilitate gravity draining).

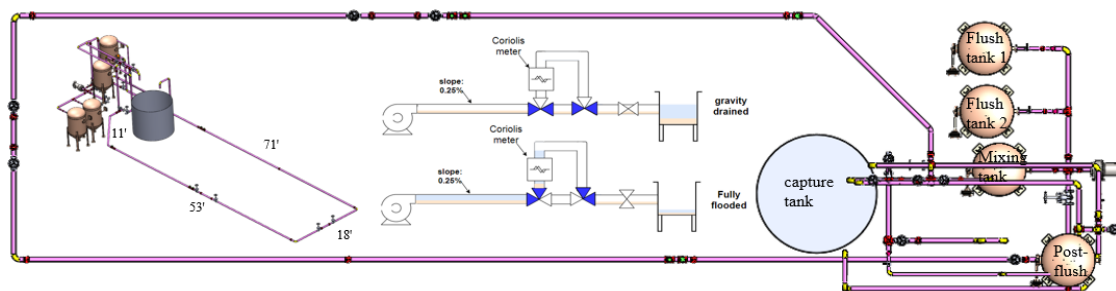


Figure 1. CAD Model of the 165-foot pipeline used for flushing experiments.



Figure 2. Constructed 165-foot pipeline used for flushing experiments.

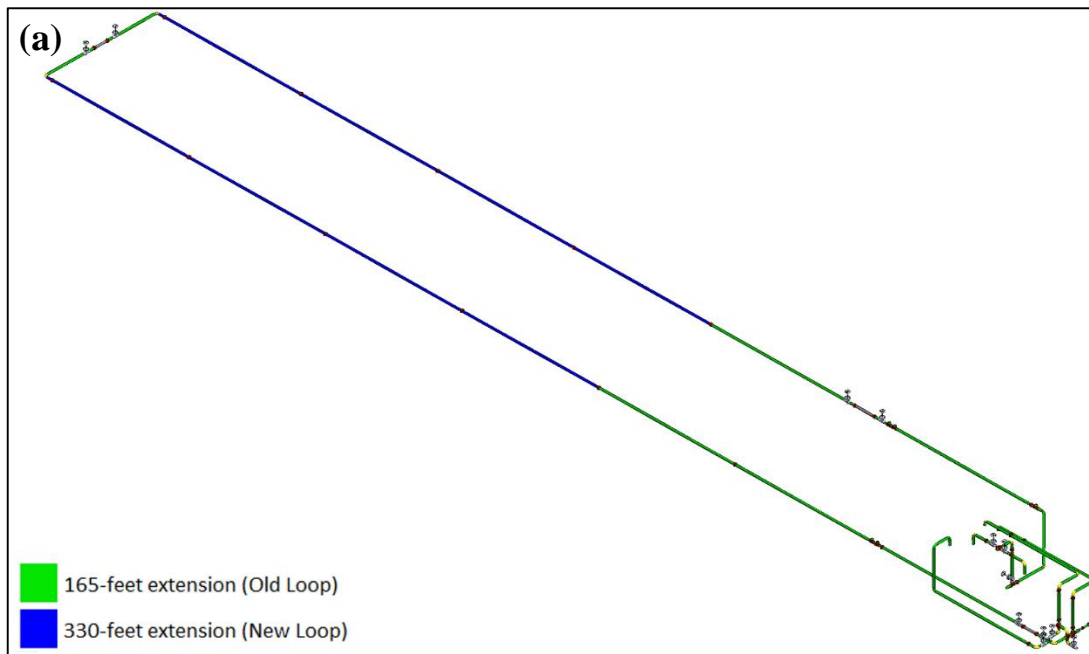




Figure 3. (a) CAD Model of 330-foot flushing loop used for second round of testing; (b) Assembled 330-foot flushing loop.

To circulate, flush, and conduct post-flush analyses, a 15 HP slurry pump (AMT 427B-95) (Figure 4) capable of delivering up to 230 GPM of water at 93 feet of head was used. This pump was controlled through a HopeWind variable frequency drive (VFD) (Figure 4) to reduce ramp-up and ramp-down times to 0.5 seconds, which is the time to reach 1,750 RPM and vice-versa, such that the ramp-up and ramp-down times and fluid velocities could be set to the limits defined by the TFC-ENG-STD-26 and flushing recommendations outlined in the various studies from PNNL. Additionally, controlling the fluid velocity from the VFD increases the longevity of the system as solids travelling beyond 10 ft/s could potentially erode the pipe wall [2].

Visualization of the flow was achieved using visual and instrumental tools. The loop was also equipped with three clear sections in the beginning, middle, and end locations for visualization purposes. The clear sections assist with characterization of initial and final conditions of sediment bed height and also allow for real-time monitoring of bed variations during flushing operations. A Krohne Optimass 1000 Coriolis meter (Figure 5) is also attached to the end of the loop, which houses sensors that measure mass flow rate, linear flow velocity, and fluid density. These sensors which output a 4-20mA current, were connected to a data acquisition device and measured to obtain fluid density and mass flow rate values. To achieve the required concentrations, kaolin or water was adjusted accordingly using density data obtained from the Coriolis meter values.

Lastly, a fluid/water level sensor (VEGAPULS 11) (Figure 5) was used to determine the volume of water flushed through the pipeline. The level sensor works by emitting a continuous, frequency-modulated radar signal through its antenna. The emitted signal is reflected by the medium and

received by the antenna as an echo with modified frequency. The frequency change is proportional to the distance and is converted into the level. The radar sensor was attached to the top of the main water flush tank during both fully-flooded and gravity-drained flush operations. Before commencing the operations, the initial height was captured manually. During the operation, the sensor's output (4-20 mA range) was captured using Bluetooth function on the VEGA mobile app and a data acquisition device (DAQ). Upon completion of the test, the final level was captured. The linear interpolation graphs were then used to convert the output to a fluid level output.



Figure 4. (Left) HopeWind VFD; (Right) AMT 427B-95 15 HP Slurry Pump.



Figure 5. (Left) Krohne Optimass 1000 Coriolis Meter; (Right) VEGAPULS 11 level sensor.

Flushing Operation

EPK kaolin with a 2.65 specific gravity was used in tests with both the gravity-drained and fully-flooded conditions. Flushing tests were conducted with system loads of 10, 15, and 20% vol of kaolin-water mixtures using a pump frequency of 35Hz to target a flow velocity below 10 ft/s. Tests were performed using two initial conditions: a fully-flooded condition and a gravity-drained condition. In the fully-flooded condition, the test loop was flooded with a simulant of a specified concentration and left to settle for approximately one day after stopping the slurry pump and without any changes to configurations or system environment. After the settling period, water from flush tanks was flushed through the system using the 15HP pump into a 500-gallon collection tank. In the gravity-drained condition, similar to the fully-flooded condition, the test loop was flooded

with a simulant of specified concentration and left to settle for one day for nominal testing.

For the 15% gravity-drained condition, studies were also conducted with variable settling times to determine the effect of prolonged sedimentation times on flush volume requirements. In these trials, the gravity-drained condition was created as described above, but the settling time was increased to one and two weeks before being drained and the test conducted. After the amount of time has passed, a drain valve was opened to remove the water from the settled kaolin, leaving behind a layer of sediment exposed to air within the pipeline. Water was then flushed through the system back into the collection tank.

To determine the effect on flush volume requirements when the flow is pulsated, a trial was conducted for the 15% gravity drained case by varying the pump's VFD from 0 to 35 Hz over 2 seconds in the ramp-up and ramp-down stages. During each pulse, 35 Hz was maintained for 7 seconds, and 0 Hz was maintained for 1 second before beginning the next pulse. This process was then repeated until the pipe was considered flushed.

Subtask 17.2: Results and Discussion

During the trials, the slurry pump was run long enough to ensure complete flushing, and the data collected was analyzed to determine the actual volume required to clean the system. The calculation of the flush-to-line volume ratio is shown in the next section. For the analysis, the clean condition was determined by the Coriolis meter's density reading (showing approximately the density of water). Flow quantities such as mass flow rate and density were also recorded using a data acquisition (DAQ) module (FieldPoint 2010) and a PRO-FLO200 totalizer. Results from the gravity-drained condition are shown in Figure 6 and results from the fully-flooded condition are shown in Figure 7. The plots show both the density and flow rates verses time for the three concentrations and for each initial condition.

For the three fully-flooded tests, the density curve starts at just above 1000 kg/m^3 , increases as more fluid with solid particles flows through the Coriolis meter and decreases to approximately the density of water after all the particles are removed. For the gravity-drained condition, the density starts at zero and increases as the slurry moves through the meter. When the pipe is flushed, the density again returns to just below 1000 kg/m^3 .

Results from the 10% gravity-drained condition (Figure 7, top) shows a strange initial oscillatory behavior in the mass flow rate, and consequently, a decrease in material density. This behavior ceases after approximately 12 seconds before it returns to the expected flow pattern. This trial was conducted multiple times, each time, resulting in the same pattern. It is likely that there was either air trapped in the system or unexpected turbulent flow, but it is not clear why this only occurred for the 10% trial. This behavior will be investigated in future trials. In addition, the flow rate for the 20% gravity-drained trial (Figure 7, bottom) was higher than expected for the pump VFD setting of 35 Hz. Results show a quicker return to the nominal density of water, however, as discussed in the next section, the FTLV ratio was consistent with other trials.

Figure 8 and Figure 9 show the results for the extended settling time and pulsation trials. For the one- and two-week settling trials, the results are similar to the 15% gravity drained trial with one day of settling time. In the pulsation trial, it is clear from the flow rate data that the flow is oscillating from 0 to the maximum allowable flow rate. Results of the density curve are similar to those of the standard pump operation mode.

Fully-Flooded Condition

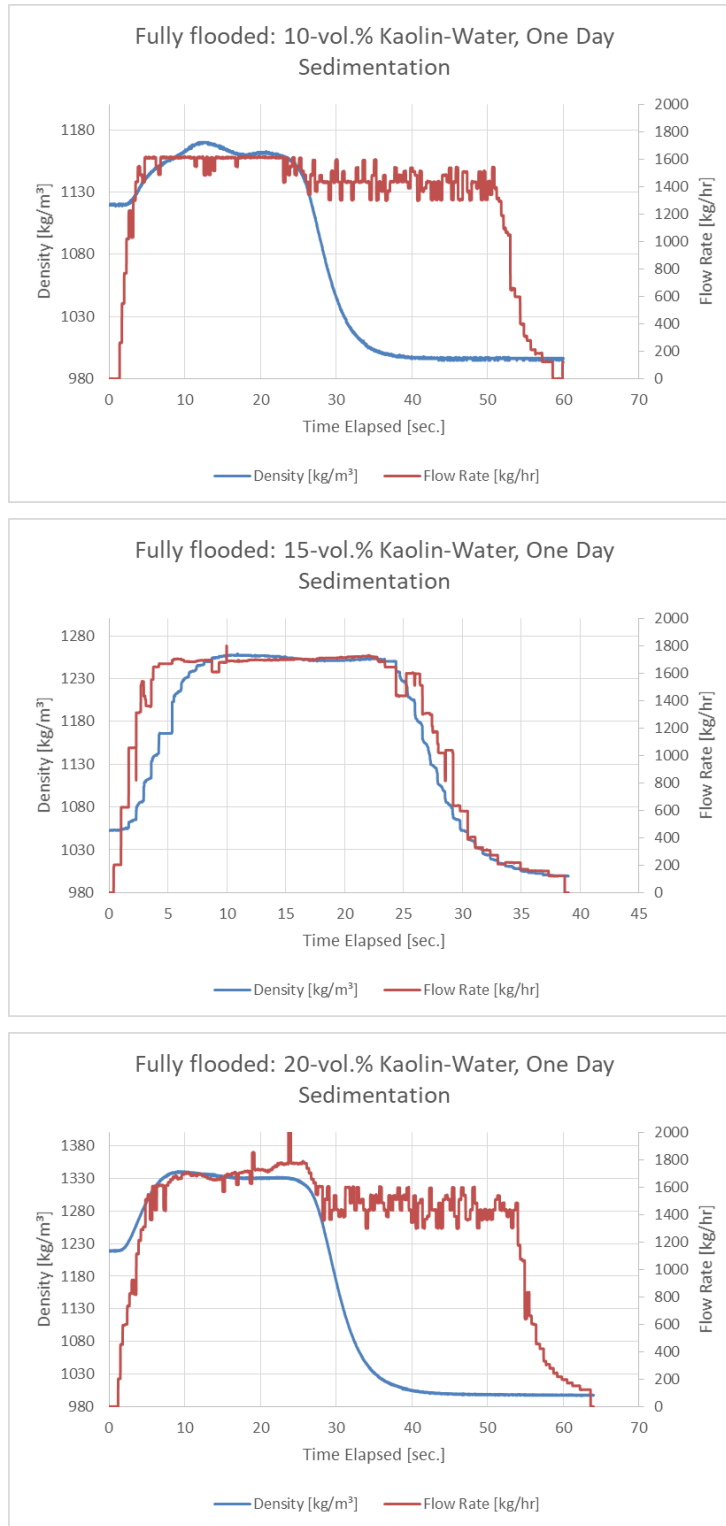


Figure 6. Density-mass flow plots for 10 % vol (top), 15 % vol (middle), and 20 % vol (bottom) kaolin-water simulants in the fully-flooded condition.

Gravity-Drained Condition

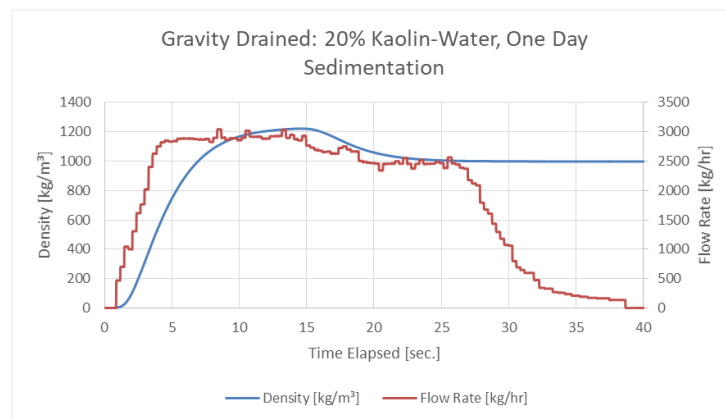
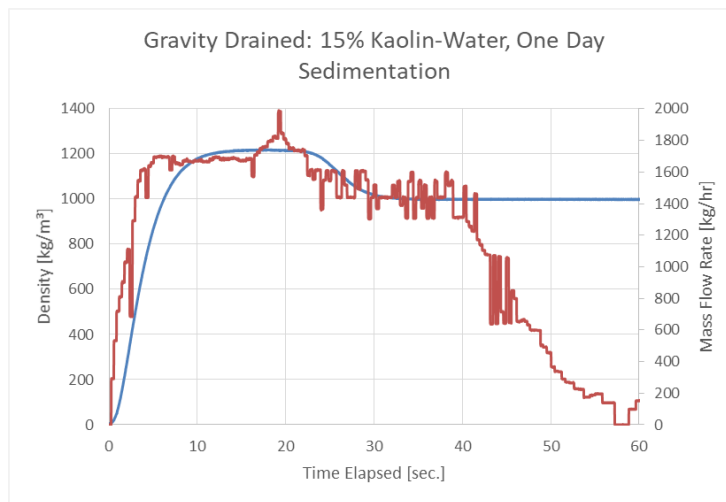
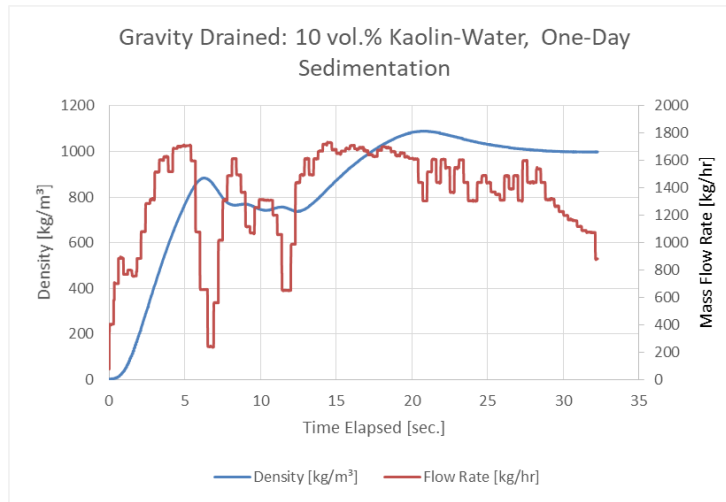


Figure 7. Density-mass flow plots for 10 % vol (top), 15 % vol (middle), and 20 % vol (bottom) kaolin-water simulants in the gravity-drained condition.

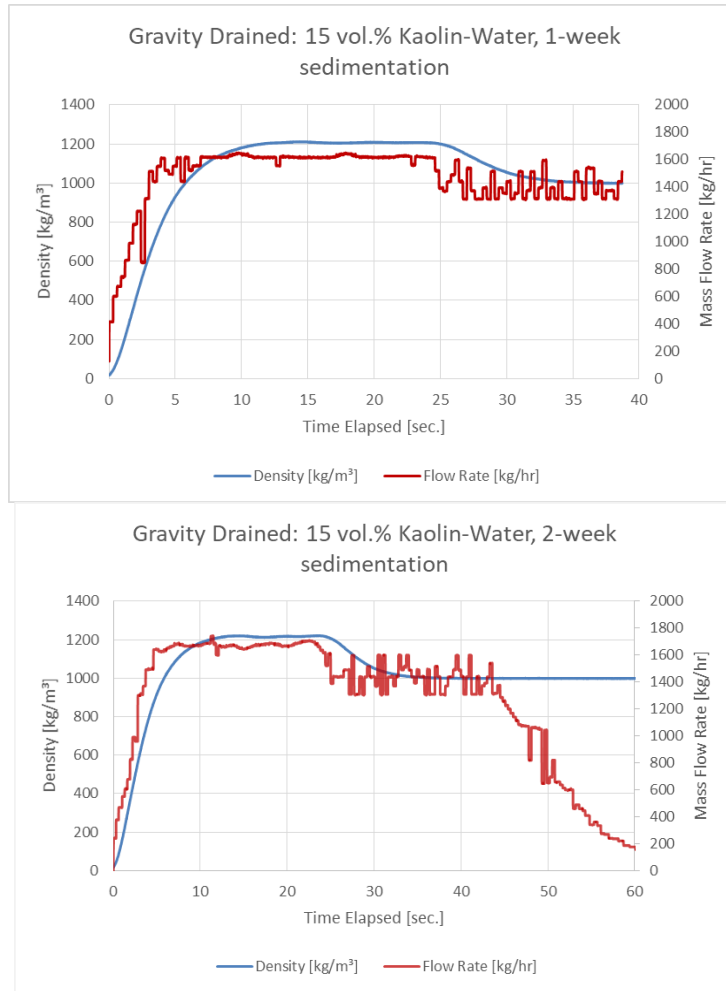


Figure 8. Density-mass flow plots for 15 % vol at one-week of sedimentation (top) and at two-weeks of sedimentation (bottom) of kaolin-water simulants for the gravity-drained condition.

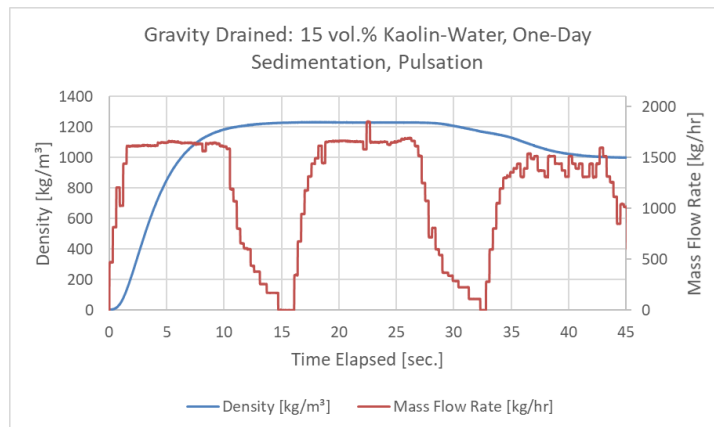


Figure 9. Density-mass flow plots for 15 % vol at one day sedimentation of kaolin-water simulants for the gravity-drained pulsation mode.

Flush-Line Volume Ratio

The flush-to-line volume ratio is a ratio of the volume of water being used to flush the line, with respect to the volume of the pipeline.

$$FTLV = \frac{\text{volume used to flush}}{\text{pipeline volume}}$$

The VEGAPULS 11 level sensor was installed on the supply tank and can be utilized to determine the volume of water used to flush by detecting a change of water level within the water tank. However, due to the limitations of hardware availability for some of the trial runs during the fully-flooded conditions and the gravity drain at 20%, a MATLAB script was generated to determine an approximate flush-to-line volume ratio. To determine when the system was “clean”, the condition of having the flow density achieve 99% of the density of water (~998 kg/m³) was arbitrarily used. The point at which the density reached this threshold was estimated using the flow rate and density curves generated for all trials using the MATLAB script. The FTLV can then be compared to the FTLV determined using the level-sensor data when applicable.

The script operates by importing the data set into the MATLAB workspace and separating the dataset into three individual variables – time, density, and flow rate. Using series of conversions on the mass flow rate dataset, the volume used could be determined at each instant of time. Results (Table 1 and Table 2) indicate that there is no substantial change to the flush-line volume ratio for the range of trials evaluated. For the conditions evaluated, the FTLV obtained was 1.2 or below. The conditions included varied volume concentrations (10, 15 and 20%), test conditions (fully-flooded and gravity-drained), variable sedimentation (1 day, 1 week and 2 weeks), and pulsation (1 day).

Table 1. Flush-to-Line Volume Ratio Results, One-Day Sedimentation

	Fully-flooded	Gravity-drained
10%	1.09	1.17
15%	1.05	1.11
20%	1.09	1.17

Table 2. Flush-to-Line Volume Ratio Results, Variable Sedimentation and Pulsation

Settlement Time	FTLV
One Day	1.11
Pulsation	1.17
1 Week	1.08
2 Weeks	1.10

Loop Expansion and Improvements

After obtaining the values for the FTLV ratio with the 165-foot configuration of the flushing loop, efforts shifted toward expanding the loop from 165 feet into the next increment of 330 feet. To determine what was required for the extension, the 165-foot CAD model was loaded on SOLIDWORKS and was expanded to the 330-foot. In total, eight 20-foot sections and eight steel

unions were procured. Upon arrival, the components were placed into approximate locations, joined together by the eight unions and placed onto two support structures composed of a 4x4 wooden beam and a Unistrut structure that allowed the pipe's height to be adjusted. These support structures were placed approximately nine feet apart in the previous performance period, and adjustments were made as necessary according to the pipe extension section's requirements due to uneven terrain. Once each pipe was safely placed onto the support, the support structure's height was adjusted to ensure that the sloping of the pipe was correct, and the support was then fixed using a rebar that was hammered into the ground.

After the loop extension was constructed, leak tests on the 330-ft extension were conducted. The test was conducted by filling the water reservoirs to its maximum capacity of 300 gallons (600 gallons total for both reservoirs), and activating the 15 HP pump operating at 25 Hz until flow into the collection tank was achieved. Once flow into the tank was certain, pump operation was ceased and the main line closed to trap water in the loop. Each union and the 90-degree elbows were then thoroughly investigated to determine if there were leaks. Each of the eight unions and both of the 90-degree bends were sealed tightly with ½" Teflon during construction of the loop – consequently, no leaks were seen.

Other improvements to the loop's data acquisition systems were procured and implemented. Over the years of use, the current data acquisition device, the NI FieldPoint, has experienced a failure or malfunction in 4 of the 7 channels on the analog, causing them to no longer be acceptable for use; with the NI FieldPoint having been officially discontinued by National Instruments, it was determined that procuring a new data acquisition device was necessary. A study was done on which to obtain based on availability, ease of use, and access to LabVIEW, which was necessary to output data legibly as density and mass flow rate values from the loop. A NI USB-6001 USB Analog/Digital I/O data acquisition device was selected due to its ease of use, plug-and-play compatibility with latest versions of LabVIEW, and affordability.

Subtask 17.2: Conclusions

Results were presented that demonstrate flushing of 10% vol, 15% vol, and 20% vol concentrations of kaolin-water slurry sediments within a 3-inch diameter, 165-foot pipe loop using fully-flooded and gravity-drained conditions. Results demonstrated that flushing with these conditions required a flush-line volume ratio of approximately 1.1-1.2. This ratio was determined by plotting the density and mass flow rate against time and observing the density behavior during flushing. Using data from the Coriolis meter, flush-line volumes were determined. Future work for this research effort includes incorporating improvements to the test loop by implementing technologies to increase the efficiency of data collection, condition setup, and recapturing of the simulant. To evaluate the effect of pipe length on the flushing operations, the loop was expanded to 330 ft. without altering the general configuration of the loop, and preliminary data will be gathered over the next year.

Subtask 17.2: References

1. R. Kazban, A., "Plugging and Wear of Process Piping at The Waste Treatment and Immobilization Plant", DNFSB/TECH-40 (2016)
2. A. Poloski, M. L. Bonebrake, A. M. Casella, M. D. Johnson, P. J. MacFarlan, J. J. Toth, H. E. Adkins, J. Chun, K. M. Denslow, M. L. Luna, J. M. Tingey, "Deposition Velocities of

- Newtonian and Non-Newtonian Slurries in Pipelines”, PNNL-17639, WTP-RPT-175 Rev. 0, (2009)
3. S. T. Yokuda, A. P. Poloski, H. E. Adkins, A. M. Casella, R. E. Hohimer, N. K. Karri, M. Luna, M. J. Minette, J. M. Tingey, “A Qualitative Investigation of Deposition Velocities of a Non-Newtonian Slurry in Complex Pipeline Geometries”, PNNL-17973, WTP-RPT-178 Rev. 0, (2009)
 4. N. Hall, “Minimum Flow Velocity for Slurry Lines”, 24590-WTP-GPG-M-0058, Rev 0 (2006)
 5. Kazban, A., “Plugging and Wear of Process Piping at The Waste Treatment and Immobilization Plant”, DNFSB/TECH-40 (2016)

TASK 18: TECHNOLOGY DEVELOPMENT AND INSTRUMENTATION EVALUATION

Subtask 18.2: Development of Inspection Tools for DST Primary Tanks

Subtask 18.2: Introduction

As part of the Hanford Site DST integrity program review, engineers at Hanford are investigating robotic technologies that can be used for the evaluation of DST tank floors. The technologies are intended to provide video feedback of the tank's primary and secondary liners so that an assessment can be made regarding the structural integrity of the tank bottom. There are three paths of access to the liners: 1) refractory air slots through the annulus, 2) a 4-in annulus air supply pipe to the central plenum, and 3) a 6-in leak detection pit drain from the central sump. In previous years, FIU has developed inspection tools that can traverse through the refractory slots and through the air supply lines. FIU has also constructed a mock-up of the DSTs for cold testing of the inspection systems.

Issues also continue at Hanford to understand the integrity of the SSTs. A previously developed 3-inch pipe crawler for use in the DST air supply line was requested to be modified for use in the lateral lines under the SSTs and to potentially provide data regarding radiation levels.

Subtask 18.2: Objectives

The objective of this task is to develop inspection tools that can provide information regarding the DST bottoms from within the insulation refractory pads and concrete foundation leading to the tank liners. FIU engineers will continue to work directly with site engineers to develop and test systems that can assist in the health assessment of the tanks. After the technologies have successfully demonstrated specified capabilities, FIU will work with site engineers to meet requirements for deployment at the sites. Specific subtasks include:

- Improvement of the design concepts that will allow for the navigation of a remotely controlled device through the refractory pad channels and/or the drain slots of DST tanks and provide visual feedback. The miniature rover system has been successfully tested in a full-scale sectional mock-up test bed and initially deployed at the sites. Additional modifications have been made and FIU will work with engineers to improve the design and support deployment. FIU will also continue to improve on a rover that can provide point thickness measurements of the tank floor from within the slots.
- Retrofitting a previously developed crawler to navigate through the lateral lines underneath the single shell tanks (SSTs) and provide information regarding potential leaks.
- Testing and improvement of the design for a 6-inch crawler that can navigate through the drain lines to the concrete foundation of the DSTs. A new miniature rover housed in the 6-inch crawler will then be deployed to inspect the secondary liners.

Subtask 18.2.1: Preparation for Deployment of Miniature Rover at Hanford

Subtask 18.2.1: Methodology

One of the primary challenges in the development of the mini rover was its ability to traverse over surfaces with weld seams. Some of the initial design concepts for the rover led to systems that had difficulty traversing the seams. After numerous tests, design changes and modifications, the current version of the rover was developed (Figure 10). Upon completion of the mini rover's first deployment at Hanford, newly acquired information has come into play. The orientation of the DST weld seams was not in a perpendicular orientation within the refractory slots of the tanks causing the mini rover to detach itself from the tank. In addition to the orientation causing the rover to fall, the makeup of the structure itself has a blunter characteristic versus a rounder transition. With this newly acquired information, FIU made modifications to incorporate minor changes to the design of the mini rover to overcome these hurdles.

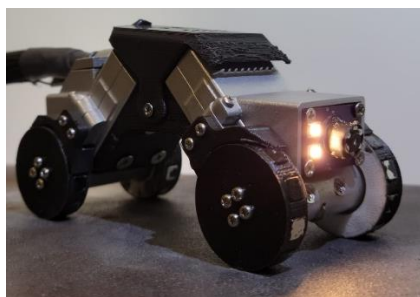


Figure 10. Current miniature rover design.

The current rover uses magnet wheels (Figure 11) to keep it attached to the metallic surface. The number of the required magnets and size of the wheels were calculated based on the torque of the motors as well as space available. The incorporation of the magnetic wheels was tested against blunt objects. It was shown that the rover can now overcome 90-degree angled obstructions with ease. The pull-off force of the rover increased from 5 to 9 lbs due to the orientation of the magnetic poles within the wheels.

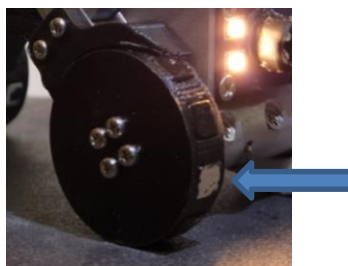


Figure 11. Magnetic wheels.

When the magnets were relocated to the wheels, a new challenge was noted due to the attraction of corrosive materials adhering to the wheels causing the rover's pull-off force to drastically decrease. With this in mind, a fender-like scoop assembly was developed that is installed over each wheel. This addition is a passive mechanism that removes the corrosion from the rover's wheels allowing the pull-off force of the rover to be sufficient and stay attached to the tank (Figure 12).

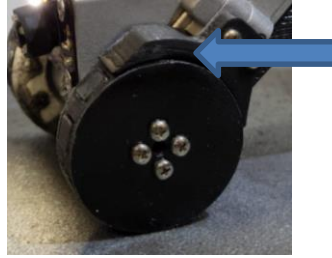


Figure 12. Wheel fender/scoops.

For the mini rover to be successful in overcoming weld seams in an oblique orientation, the rover's chassis must be flexible and capable of twisting along the longitudinal axis of the body to keep all four wheels adhered to the surface. To address this issue, TPU (Thermoplastic polyurethane) was incorporated in the frame (Figure 13) which allows the rover to flex.

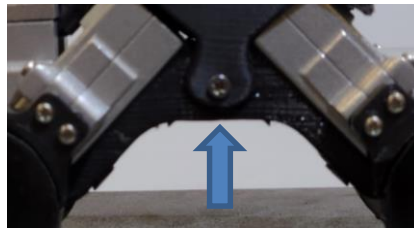


Figure 13. TPU material installed in frame.

With the long tether requirement, power was lost due to the voltage drop. Video quality was also reduced for similar reasons. In order to address this issue, the current control box for the mini rover was designed to utilize stronger DC motors and a longer tether. The new control box includes a RoboClaw 2X7A as a digital controller and is controlled through serial communication using a python library. The computer receives the commands from the Xbox controller and sends the commands to the motor controller through the serial communication. The RoboClaw also receives its power from the power supply, which can go up to 34V and generate a 34V PWM signal to control the DC motors. To be able to deploy the miniature rover system at DOE facilities, an electrical safety inspection is required for the control box. After the control box design was finalized and fabricated, it was subjected to an electrical safety check and received the required certification to be considered for use at Hanford. The inspection validated the capabilities of the control box and ensured safe operating conditions.



Figure 14. Final control box design.

FIU has also worked with engineers from Washington River Protection Solutions (WRPS) to develop a test plan that will ensure that the mini rover is safe and can complete the necessary tasks when deployed. A test plan was developed in conjunction with WRPS that includes four areas of testing and validation: durability, emergency retrieval, weld seam traversal and corrosion surface testing. The following sections highlight the procedure for each of the tests.

Durability Testing

The durability test will assess the durability of the mini rover while subjected to a thermal load. For this test, the rover will be driven inside one of the mockup’s channels from the annulus until it reaches the central plenum and then return to the channel entrance. Multiple trips will be conducted to ensure the components on the rover can withstand long-term operation. During the testing, the channels will be heated to emulate the conditions with the slots of typical tanks.

The process of heating will include blowing hot air into the channel using two heating fans placed at the central plenum and annulus. The blower’s temperature and flow rate will be adjusted to attempt to maintain roughly 130°F in the channel. Side channels (branches) will be blocked using a thermal insulation foam and filler material. The gaps between the primary liner plates and the space between the plates and the concrete sections along the air slot channel will be sealed using insulation foam. Thermocouple probes will be inserted into the channel via the side channel gaps and insulation at four points (C0, C1, C2 and C3 in Figure 15). These four points will be used to obtain real-time temperature measurements. K-type thermocouples with 4 feet bendable metal probes connected to a USB-UTC 8-channel data acquisition system will be used for temperature monitoring.

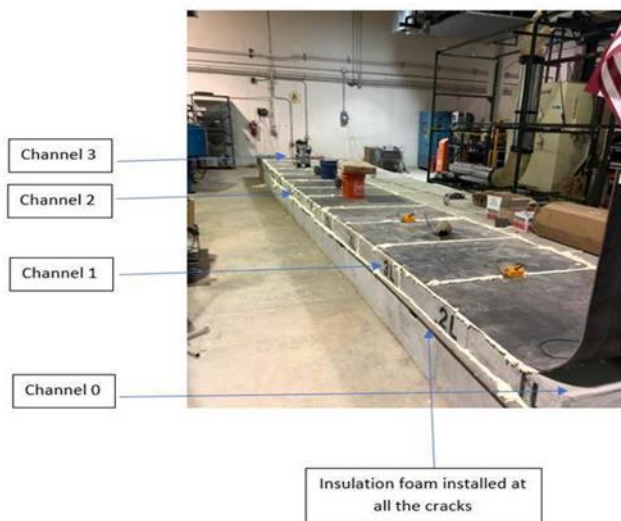


Figure 15. Durability test mockup.

To evaluate the process, the channel was heated with the two heating fans installed at the two ends. Table 3 shows the temperature measured at four locations for two hours.

Table 3. Heating the Channel for Two Hours

Time	C0	C1	C2	C3
10:45	73.88	76.2	76.13	76.30
11:00	128.24	89.48	105.72	156.12
11:15	131.80	94.28	112.46	158.21
11:30	133.52	97.53	116.52	158.44
11:45	134.57	99.71	120.7	159.56
12:00	134.92	101.05	121.76	159.62
12:15	136.57	103.35	123.64	161.08
12:30	137.32	104.82	125.01	161.32
12:45	137.23	105.97	126.07	160.38

The heating fan was then removed at the entrance and the temperature drop was monitored for 15 minutes (the time that rover needs to go all the way to the end of the channel and come back). After 15 minutes, the heating fan was reinstalled, and it took 8 minutes to get back to the temperature before removing the fan.

Table 4. Temperature Drop after Removing One Fan

Time	C0	C1	C2	C3
12:45	137.23	105.97	126.07	160.38
12:47	123.48	101.72	126.32	161.12
12:49	122.29	101.53	125.98	161.57
12:51	120.31	101.86	126.60	161.25
12:53	118.84	102.03	126.42	160.86
12:55	117.61	102.38	127.27	161.55
12:57	116.52	102.50	127.15	161.41
12:59	115.48	102.42	127.33	162.08

Emergency Retrieval Testing

The emergency retrieval test will assess if the rover is capable of being withdrawn from within the channel in the event of a unit failure, or if the unit falls from the tank. To assist with emergency retrieval, the rover is equipped with a tether that is secured with a locking cap. The tether consists of the main cable, a stainless-steel wire cable for strength support and expandable braided sleeve (Figure 16). The stainless-steel wire cable has up to 368 lbs. of load before failing. The tether may be pulled manually from grade through the riser, annulus, and refractory to retrieve the unit. The test will evaluate whether the tether and locking cap can withstand the loads applied to the crawler during the retrieval process.

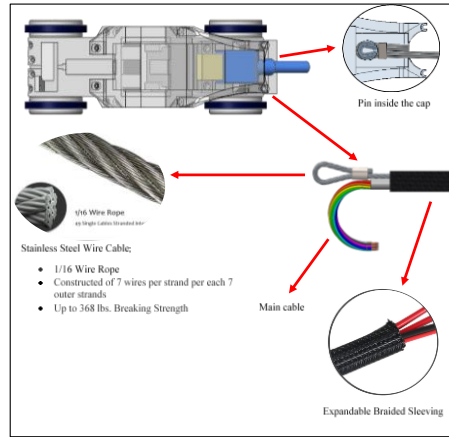


Figure 16. Tether details.

Oblique/Blunt Weld Seam Testing

The weld seam test will assess the mini rover’s ability to traverse weld seams on the primary liner of the tank. Shown below is the oblique/blunt weld seam test which challenges the rover’s capabilities to overcome the orientation of seams in the worst-case scenario. The weld seam plates will be placed near the central plenum. The rover will be required to traverse the weld seams while pulling the tether, extending the entire length of the mockup.



Figure 17. Oblique/Blunt weld seam.

Corroded Surface Testing

The corroded surface test will assess the rover’s ability to traverse corroded surfaces (Figure 18) without change in the unit’s performance. A critical issue will be the observation of corroded material accumulation on the magnets and its effect on performance. Now that the magnets have been relocated to the wheels, the fenders/scoops system will be observed to ensure functionality.



Figure 18. Corroded surface test.

Subtask 18.2.1: Results and Discussion

The newly built rover was designed with two challenges to address: overcoming oblique/angled weld seams and traversing over blunt obstructions. The test plan was also updated to challenge the rover in this capacity. Upon completion of the implementation of the TPU material into the frame of the rover, the test plan was executed. The newly TPU outfitted rover was able to overcome blunt obstacles. The second design change was the incorporation of the magnetic wheels. It was shown that the rover can now overcome 90-degree angled obstructions with ease which will aid in overcoming any weld seam orientation. The pull-off force of the rover increased as well from 5 lbs to 9 lbs due to the orientation of the magnetic poles within the wheels. It was noted that if the magnets are orientated with the poles alternating, a greater pull-off force was obtained due to the magnetic flux from the alternating poles not interacting with each other's similar fields. The addition of the fender/scoop mechanism to each wheel also performed as designed. The corrosive material was being knocked off the wheel assemblies passively allowing the rover to remain magnetically attached to the surface. The current design of the mini rover passed each of the tests in the modified test plan.

Subtask 18.2.1: Conclusions

After completion of the mini rover's first deployment, newly acquired information has come into play. The design changes have been made to the mini rover and has passed all tests in accordance with the WRPS test plan. Currently the newly designed mini rover transfer paperwork has been approved and the unit is scheduled to be deployed in mid-January 2022 at Hanford site.

Subtask 18.2.1: References

1. J. R. Bontha, H. E. Adkins, K. M. Denslow, J. J. Jenks, C. A. Burns, P. P. Schonewill, G. P. Morgen, M. S. Greenwood, J. Blanchard, T. J. Peters, P. J. MacFarlan, E. B. Baer, W. A. Wilcox, "Test Loop Demonstration and Evaluation of Slurry Transfer Line Critical Velocity Measurement Instruments", PNNL-19441 Rev. 0 (2010)
2. K.M. Denslow, J. J. Jenks, J. R. Bontha, H. E. Adkins, C. A. Burns, P. P. Schonewill, N. N. Bauman, D. F. Hopkins, "Hanford Tank Farms Waste Certification Flow Loop Phase IV: PulseEcho Sensor Evaluation", PNNL-20350 FINAL (2011)

Subtask 18.2.4a: 6-inch Crawler Development

The subtask's primary goal is to develop robotics technologies adequate for inspecting secondary liner bottoms in double-shell tanks. In July, efforts were shifted based on site needs to retrofit FIU's existing 4-inch pipe crawler to house a gamma scanner that can traverse through horizontal pipes (lateral) installed underneath Hanford's single-shell tanks to map potential radiation. The appearance of gamma activity in a lateral would indicate a possible tank leak. The development efforts in both crawlers are reported in Subtasks 18.2.4a and 18.2.4b, respectively.

Subtask 18.2.4a: Methodology

Recent concerns about the structural integrity of the containment liner of double-shell tanks at Hanford site have prompted Florida International University (FIU) to continue developing specialized tools. The primary concern is the significant thinning of the secondary liner. In some tanks, measurements in the annulus floor show thinning up to 70%.

The only viable access to the secondary liner, under the refractory region, is through the leak detection system. In most Hanford tanks, the system consists of a leak detection pit connected to a DN 150 (NPS 6) drain pipeline providing access to drain slots in the concrete foundation under the secondary liner. The drain slots in the foundation consist of a maze of channels about 115 mm (4.5 inches) with 65 mm (2.5 inches) high. As illustrated in Figure 19, most configurations use an entry manifold that slopes up from the drain pipeline to the plenum in the middle of the tank [1].

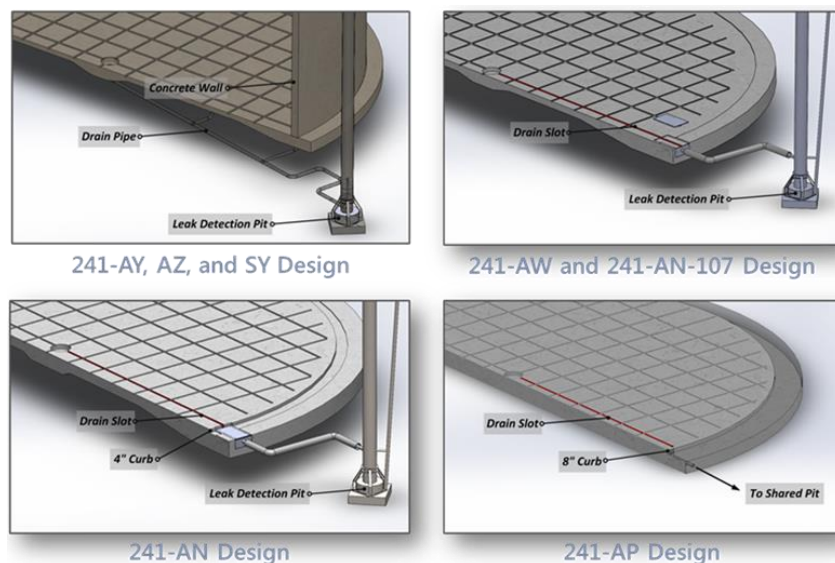


Figure 19. Leak detection systems at Hanford's DSTs.

Marsupial System

The tool FIU has been developing is a robotic marsupial system that uses a mother pipe crawler to navigate through the drain pipeline and deploys a miniature child rover into the drain slots to inspect the bottom of the secondary liner while providing live video feedback, as illustrated in Figure 20. There are also plans to integrate an ultrasound probe for point thickness measurements.

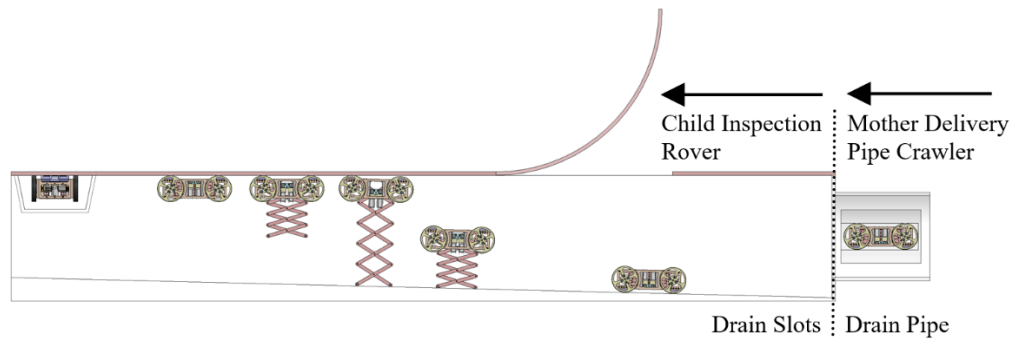


Figure 20. Proposed inspection.

Currently, the focus is on integrating the inspection rover into the delivery pipe crawler, as well as full-scale testing, necessary deployment arrangements, and payload customization.

Miniature Child Inspection Rover

The child inspection rover is a modified version of other magnetic miniature rovers previously developed at FIU. The unit can travel on the bottom of the drain slots or magnetically attach to the top secondary liner, extending and pulling itself using magnetics attachments installed in a scissor lift mechanism. Figure 21 shows a functional prototype of the inspection rover.

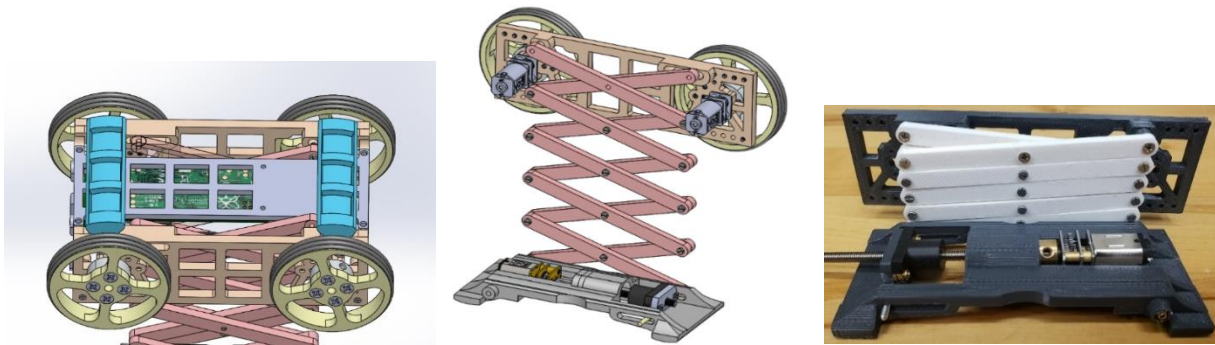


Figure 21. Child inspection rover.

Figure 22 shows a release mechanism, a miniature linear actuator, that pushes the magnets away from the secondary liner during disengagement and unit retrieval synchronized with the opening of the scissor lift mechanism.

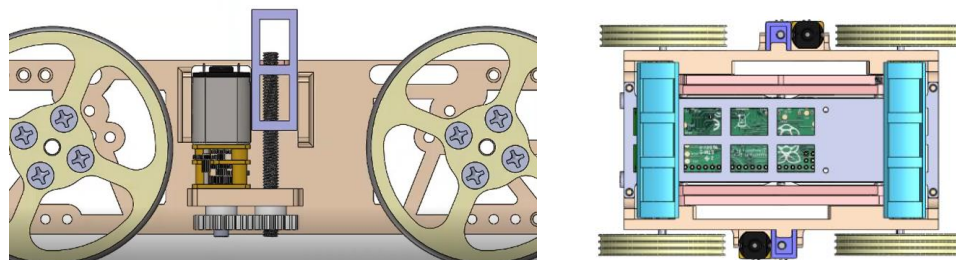


Figure 22. Magnetic detaching mechanism.

In addition to the miniature electric motors, the instrumentation rover's original embedded electronics includes a) motor controllers for the wheels, scissor lift, and detaching mechanism, b)

camera modules at the front, rear, top, bottom, and sides of the frame, c) analog video multiplexer, d) voltage regulators, e) an ethernet module for communication, and f) the main microcontroller.

Figure 23 depicts the rover's original overall system diagram. In the chart, a tether distributes power (12 volts) and ground, two communication lines for the CAN bus module, and one line dedicated to analog video signals selected by the analog video multiplexer.

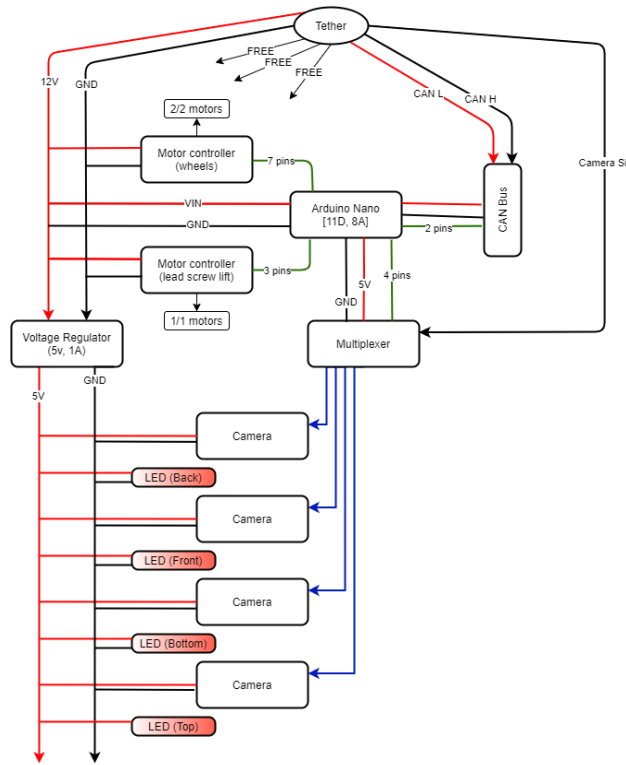


Figure 23. Inspection rover overall schematic.

The current prototype is tethered by a Category 6 Ethernet cable, which provides data communication and video feedback and supplies power to an embedded computer, onboard electronics, and motors, rather than the original design using a microcontroller interfaced by CAN-BUS. Upgrading from a design based on a microcontroller to a single board onboard computer module is a more flexible architecture allowing asynchronous digital communication, camera, and sensor streaming instead of relaying by adding dedicated analog lines.

Figure 24 shows the schematic layout of the onboard electronic components, including a 5V step-down voltage regulator, the embedded onboard computer, an Ethernet to SPI adaptor, and two dual-motor controllers. One motor controller moves the frame's wheels, and the other controls the detaching and scissor lift mechanisms on the rover.

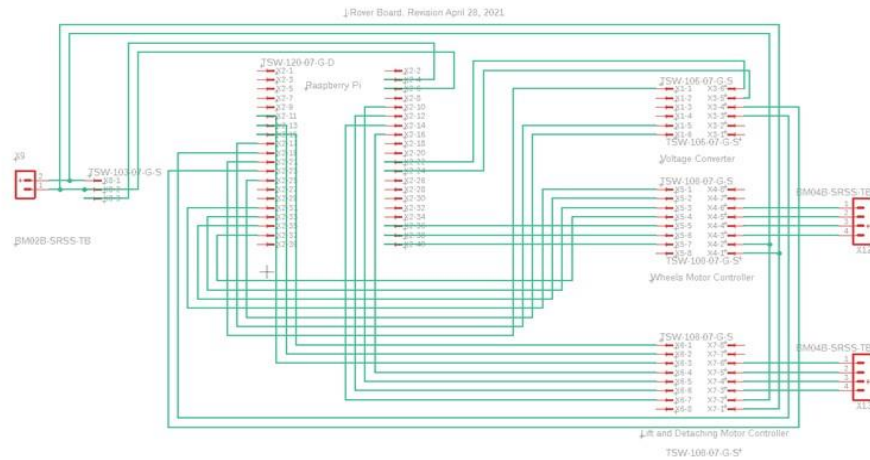


Figure 24. Instrumentation electronics schematic.

Figure 25 shows the rovers printed circuit board (PCB) that connects all electronics onboard. The PCB layout places the components as closely as possible to minimize the rover frame footprint.

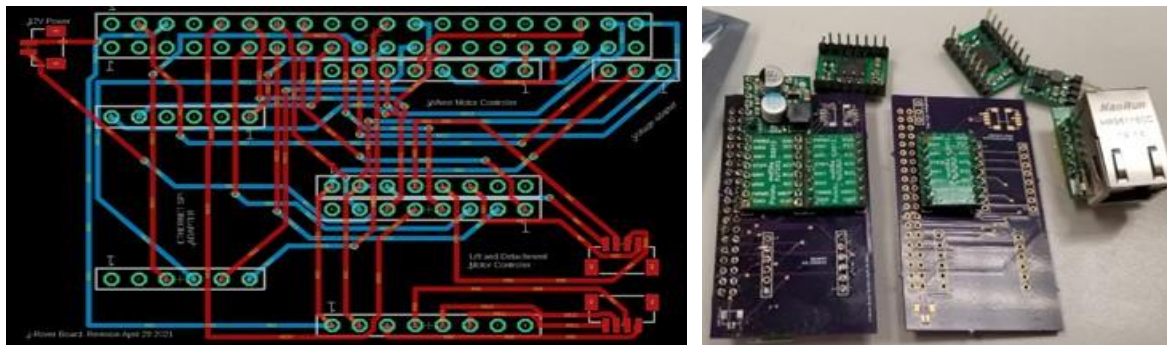


Figure 25. Onboard printed circuit board.

Figure 26 shows a 3D model of the instrumentation rover, displaying the current layout of the onboard electronic components and PCB.

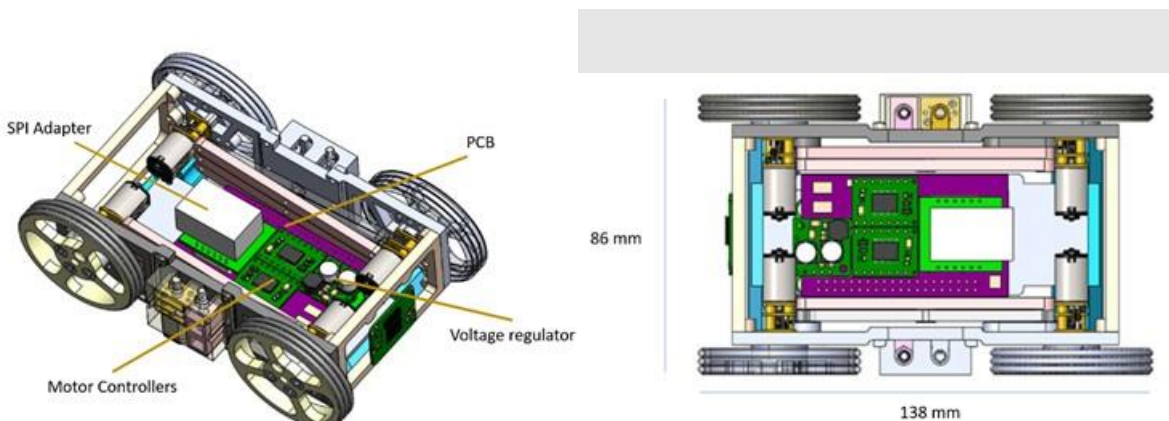


Figure 26. Instrumentation rover current model footprint.

Mother Delivery Pipe Crawler

The mother pipe crawler has multiple functions, including traversing the entry drain pipeline, deploying the miniature child rover, managing the tethers of both units, and rescuing the miniature tool in case of failure.

During this performance period, the crawler's development activities focused on designing the pipe crawler's frontal housing modules to deploy the child miniature inspection tool into the foundation drain slots. Efforts were also dedicated to designing an alternative track-driven pipe crawler instead of previous versions using peristaltic locomotion, such as the one shown in

Figure 27.

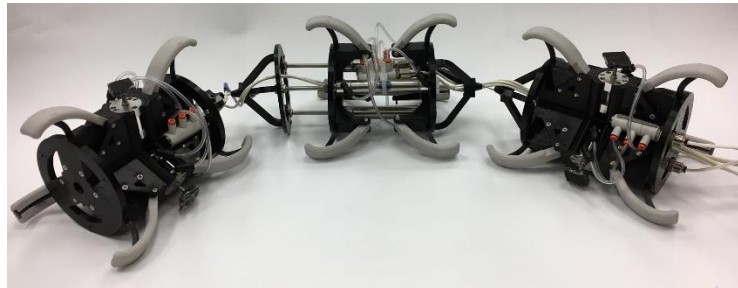


Figure 27. Peristaltic delivery pipe crawler prototype.

The peristaltic crawler operates using pneumatic actuators on the same peristaltic principles of other inspection tools previously developed at FIU [3]. The crawler's current design has front and back grippers and a middle expansion module. The modules are attached with articulating joints that allow the unit to maneuver through pipe bends. The actuators are radially distributed in each module, allowing a hollow core convenient for carrying payloads, instrumentation, and cabling. The crawler also uses spring-loaded guides that assist in passing through the harsh environments found in the existing DST's drain pipeline with significant sediments, buildup, and scaling. Figure 28 shows the drain lines' current conditions from previous unsuccessful inspections at Hanford. The guides drastically reduce the crawler drag while minimizing potential sediment accumulation and bulldozing effect during inspections.

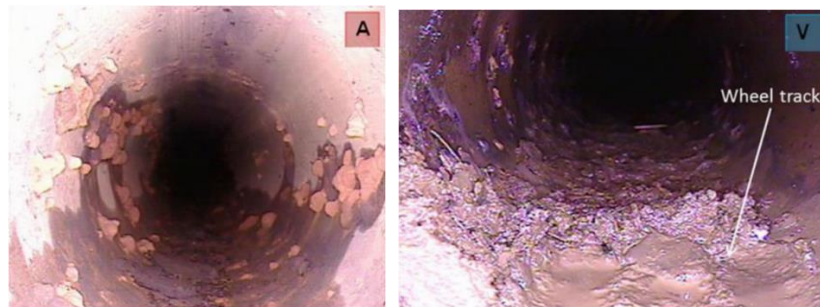


Figure 28. Drainpipe existing sediments and buildup.

As illustrated in Figure 29, at drain slot entry, the distance between the rover and the floor is about 3.5 inches (89 mm), which requires a deployment apparatus to deliver the inspection rover from the housing module to the floor of the leak detection manifold. The pipe crawler modules are about 4 inches in diameter and are centered by guides to avoid existing sediment and buildup in the leak detection pipeline.

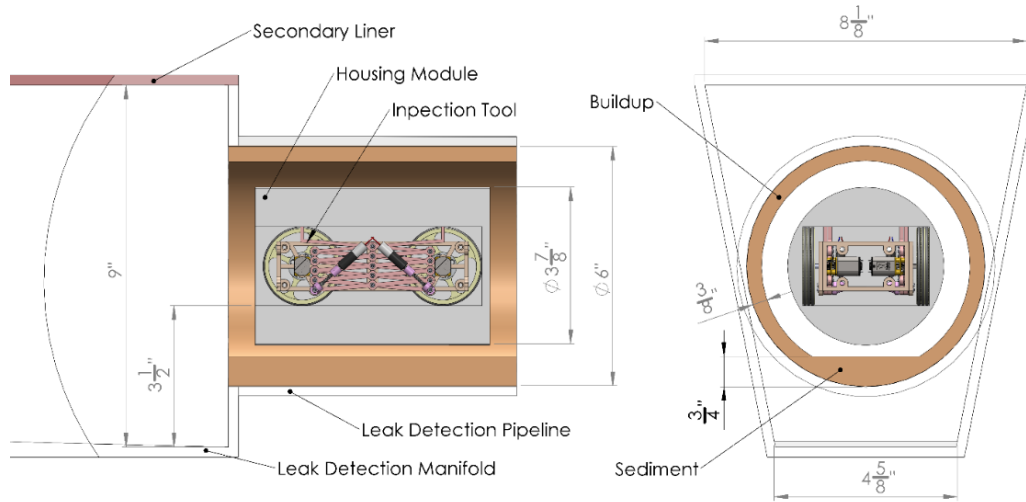


Figure 29. Housing module.

One of the considered deployment options is using an overhead ramp. As illustrated in Figure 30, the scissor lift magnet attaches to the ramp that deploys and retrieves the unit using the scissor lift mechanism.

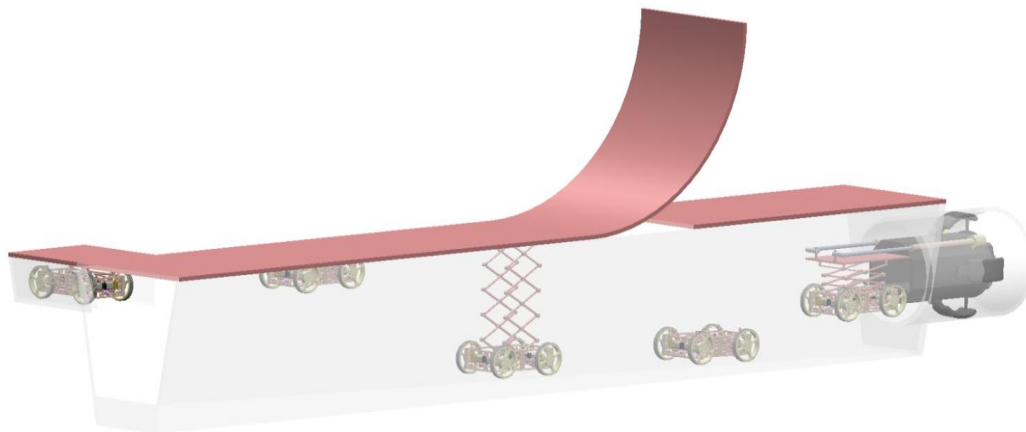


Figure 30. Overhead deployment ramp.

A more reliable option has been considered using a retractable ramp, allowing the rover to drive in and out of the module, as illustrated in Figure 31. The ramp uses a sequence of three foldable panels, the first one operated by actuators, the second by guides and gravity, and the third one by springs and followers, illustrated by the multibody dynamics simulation.

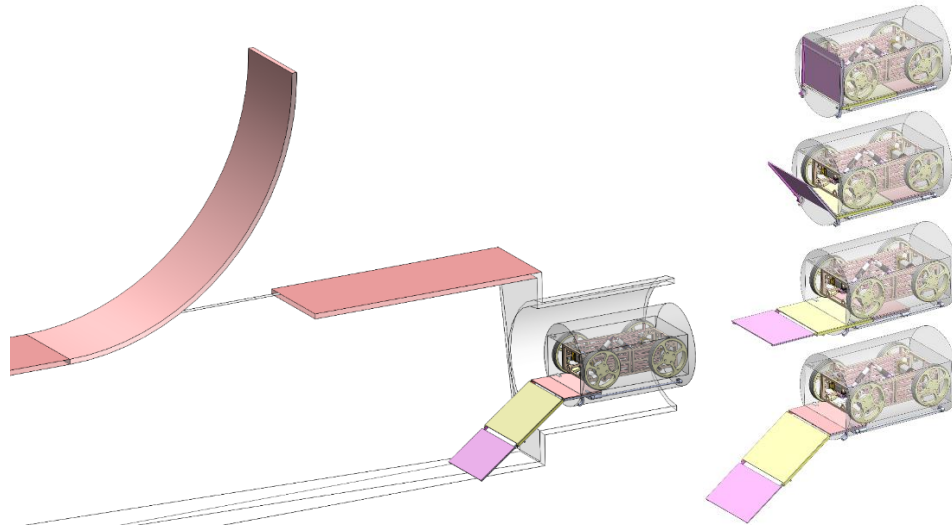


Figure 31. Retractable deployment ramp.

Finally, as illustrated in Figure 13, an electric version of the delivery pipe crawler using tracks can have a more compact design with fewer moving parts than the previous peristaltic crawlers. The proposed electric crawler carries the inspection rover using a system of three tracks. The tracks design considers a 3/4-inch tall deposit of sediment accumulated at the bottom of the pipe.

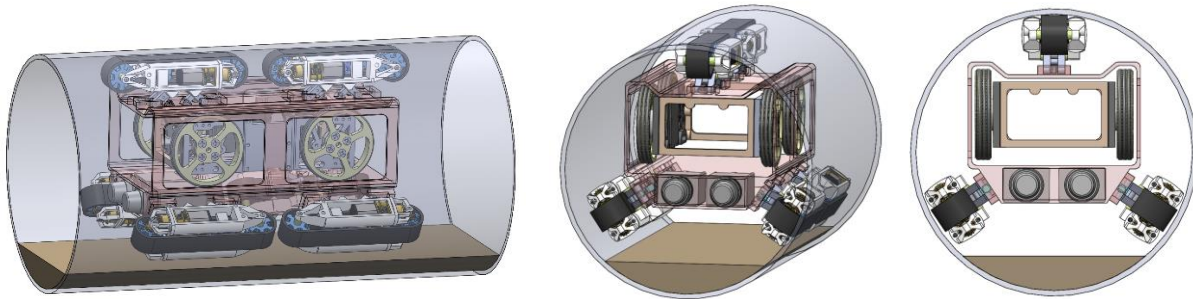


Figure 32. Track-driven delivery pipe crawler conceptual design.

Figure 33 illustrates the current design of the track-driven suspension. The track uses two lateral geared motors powered by a bevel gear transmission. The track tension is adjusted by tightening or loosening screws at the gears' bearing mount. The independent tracks are attached to the crawler's frame using a scissor link suspension. The spring suspension provides an extra degree of freedom, allowing the tracks to push up and down and tilt, always keeping traction against bends, depressions, and eventual buildups.

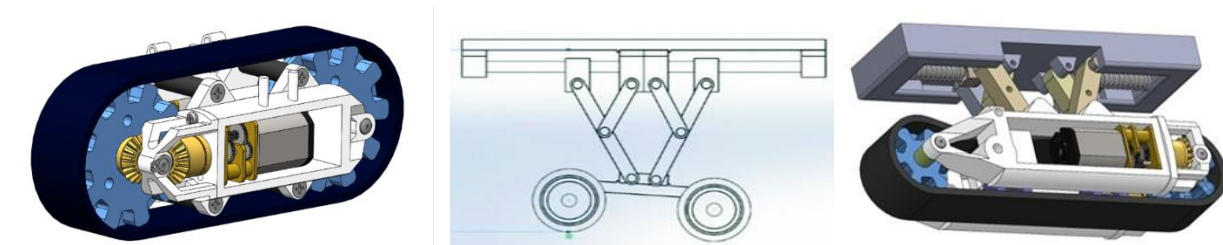


Figure 33. Tank suspension design.

Figure 34 illustrates the all-electric marsupial system, including the housing module and the instrumentation rover.

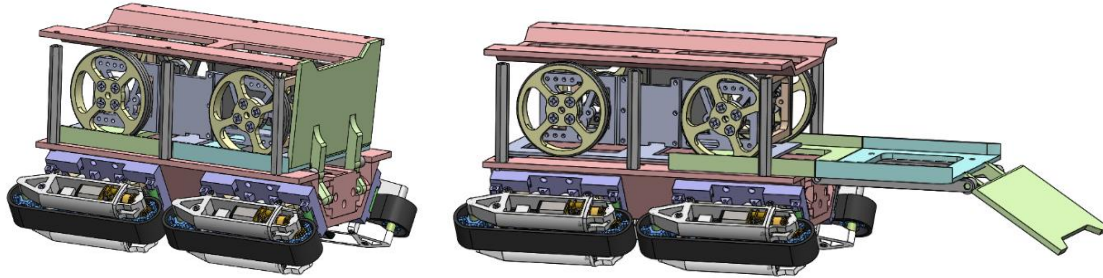


Figure 34. Model of the rover in housing module with deployable ramp.

Mockups and Testing

Exhaustive full-scale tests were designed to verify and validate the secondary liner inspection tool using the FIU's full-scale sectional mockup. The mockup, illustrated in Figure 35, is intended for real-scale tests and evaluation of robotics and sensor technologies [2].

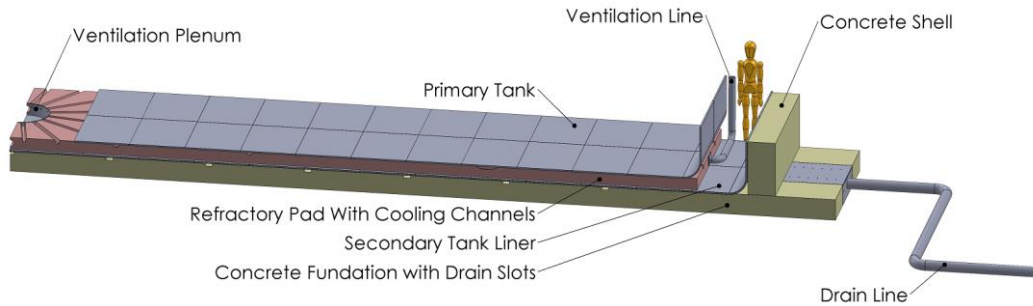


Figure 35. DST's full-scale sectional mockup.

As illustrated in Figure 76, the mockup will cover approximately 7% of the DST's foundation.

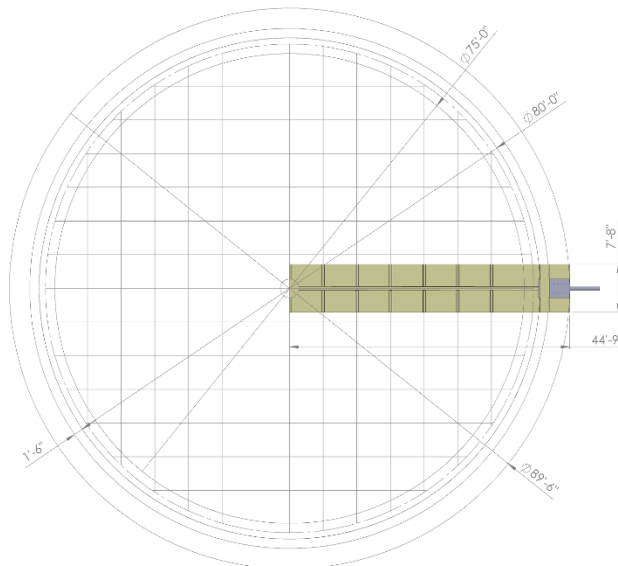


Figure 76. Foundation drains channels layout.

Figure 77 shows the layout of the concrete foundation in the mockup under the secondary tank liner. The foundation leak detection system has a maze of sloped drains. The drains are precisely sloped and angled according to the DST's shop drawings in the mockup.

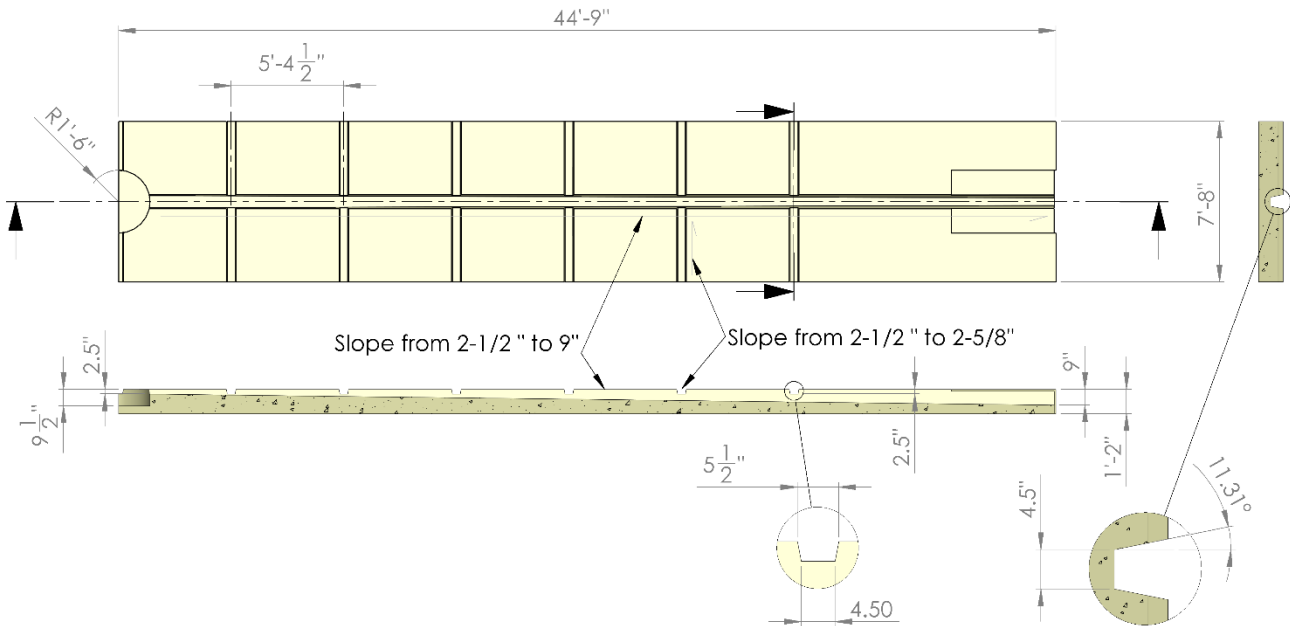


Figure 77. Concrete foundation with drain slots.

The mockup foundation and refractory pad are wood, coated with concrete held together by a metal mesh. As shown in Figure 36, this combination provides a modular and lighter structure combined with surface properties similar to the DST ones.

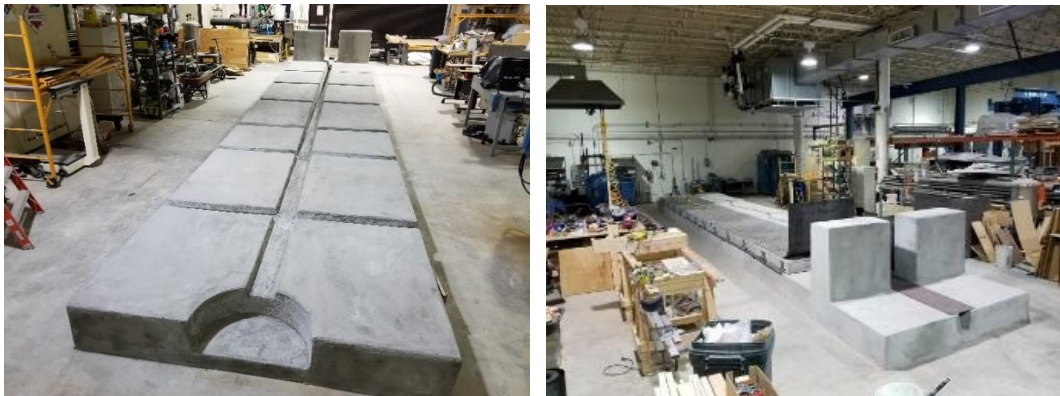


Figure 36. FIU's DST's full-scale sectional mockup.

Subtask 18.2.4a: Results and Discussion

Figure 21 shows a functional prototype of the inspection rover tested traveling magnetically attached to a top metal plate and extending and pulling itself up using its scissor lift mechanism.

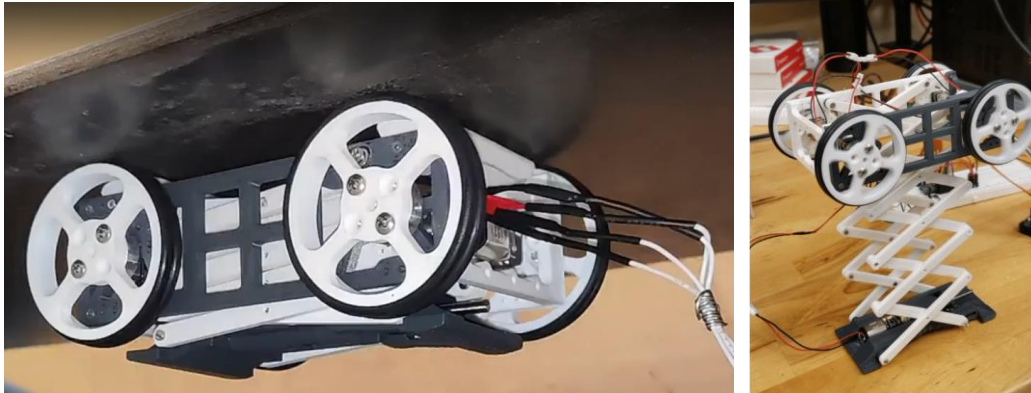


Figure 37. Child inspection rover.

Figure 22 shows the release mechanism tested, pushing the magnets away from a top metal plate magnetically disengaging itself for unit retrieval.

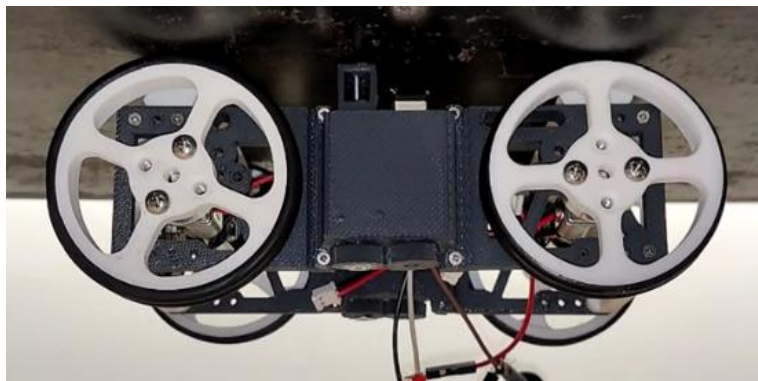


Figure 38. Magnetic detaching mechanism.

Figure 39 shows the rover prototype, where all onboard electronics were tested successfully, receiving controls, asynchronously streaming video and data simultaneously over a 200 ft of tether, with minimal feedback delay.

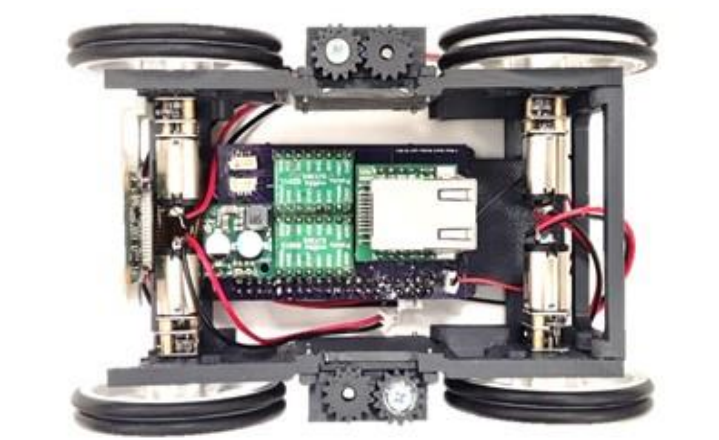


Figure 39. Instrumentation rover current prototype.

Figure 40 shows a deployment ramp prototype that uses a lead screw to carry the ramp assembly forward and back and a series of guide pins and springs that let the ramp deploy, retract, and close the first section of the ramp as a lid.

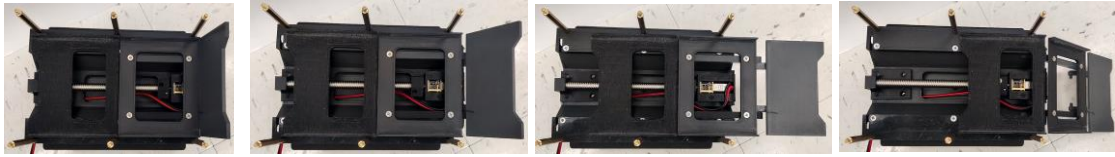


Figure 40. Retractable deployment ramp prototype.

Figure 41 shows a track prototype currently being used for testing. Each track uses two robust micro metal geared motors in a bevel gear for transmission. The track has a bottom spring-suspension system that increases rubber tension and improves traction.

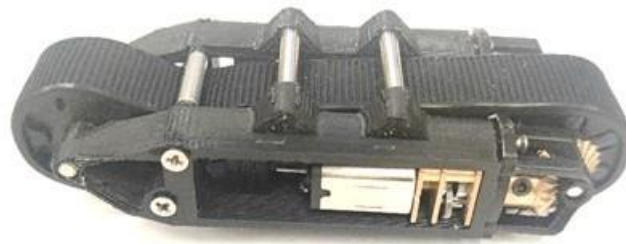


Figure 41. Tank track prototype.

Figure 42 shows tests of the current prototype deploying the instrumentation rover using a retractable ramp. The rover successfully drives out the module; however, it requires designing a foldable guide that would funnel the rover back inside the module using the narrow ramp without precise reverse maneuvers.



Figure 42. Housing module with ramp prototype.

Figure 43 shows a seminal graphical user interface (GUI) developed for the system's control box. The current version is operating system agnostic and can visualize and record all cameras attached to the box's embedded computer. In addition, the GUI is tailored to interact with the operator using touchscreen monitors, suitable for field operations, not needing a keyboard or mouse. The GUI will also be used in other inspection tools currently being developed at FIU.



Figure 43. Control box's GUI.

Subtask 18.2.4a: Conclusions

The design efforts will continue streamlining the marsupial system, incorporating improvements in the mother delivery crawler, the child inspection rover, and the control box, based on exhaustive full-scale tests. The improvements will include better cable management, power, communication, and controls. A prototype of the housing module will be finalized and seamlessly integrated. There are also plans to integrate additional sensors, such as an ultrasound probe for thickness measurement, a lidar module for channel mapping, and temperature and humidity sensors for environmental characterization. Eventual modifications will be made based on the engineering-scale test results, incorporating Hanford deployment requirements coordinated with the site engineers.

Subtask 18.2.4a: References

1. Engeman, J.K., Girardot, C.L., Harlow, D.G., Rosenkrance, C.L. , 2012, Tank 241-AY-102 Leak Assessment Report, Washington River Protection Solutions, RPP-ASMT-53793, Rev. 0
2. DiBono, M., Abrahao, A., McDaniel, D., Lagos, L. and Tan, Y., 2018, Engineering Scale Testing of Robotic Inspection Tools for Double Shell Tanks at Hanford, Proceedings of the Waste Management Symposia 2018, Phoenix, AZ.
3. Abrahao, A., Fekrmandi, H., Gocke, E., Sheffield, R. and McDaniel, D., (2016) Development of Inspection Tools for the AY-102 Double-Shell Tank at the Hanford DOE Site, Proceedings of the Waste Management Symposia 2016, Phoenix, AZ.

Subtask 18.2.4b: Crawler Development for SST Lateral Gamma Scans

The subtask's primary goal is to retrofit FIU's existing 4-inch pipe crawler to house a gamma scanner that can traverse through horizontal pipes (laterals) installed underneath Hanford's single-shell tanks to map potential radiation.

Subtask 18.2.4b: Methodology

In the 1960s, to enhance tank leak detection capabilities, caissons were dug in both the A and SX tank farms with horizontal pipes installed under the tanks to allow gamma logging [1]. As illustrated in Figure 44, these horizontal pipes (laterals) were routinely monitored for gross gamma activity. The appearance of gamma activity in a lateral would indicate a possible tank leak. The laterals were installed about 10 ft below the bottom of the tanks after the tanks were constructed. Each lateral is a 3-in. pneumatic stainless steel tubing and is enclosed in a 4-in. carbon steel pipe. The laterals are horizontal and extend radially from a large caisson (12-ft diameter) that is located between up to four tanks. The access to each lateral is through a separate vertical tube (also made of 3-in. pneumatic stainless steel) that extends up to the floor of the lateral shack. The lateral tube transitions from vertical to horizontal at the bottom of the caisson through a 90° elbow with a 4-ft bend radius.

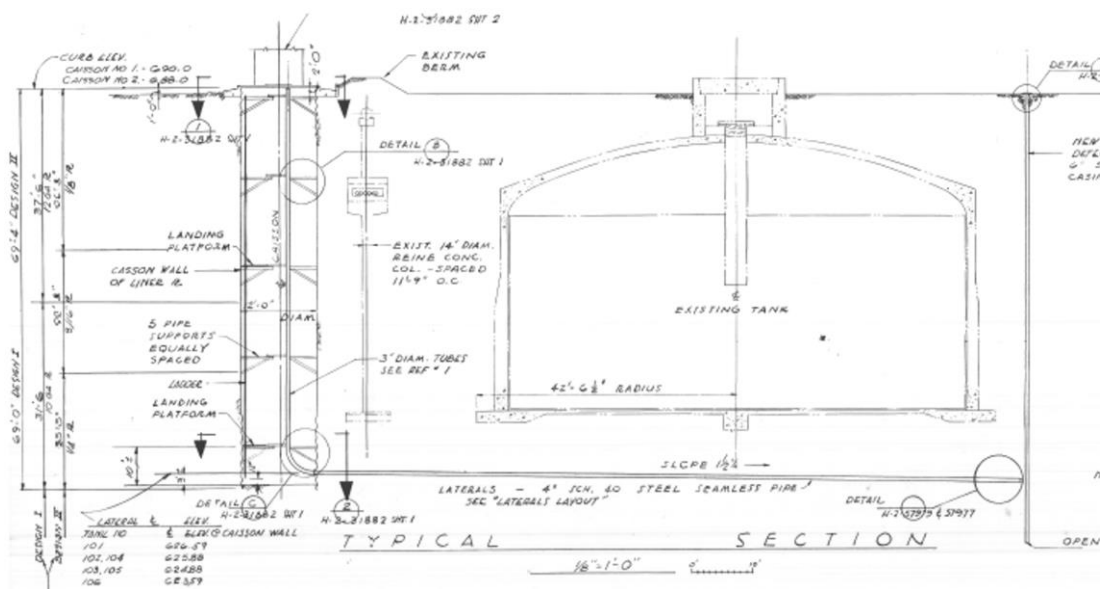


Figure 44. Single shell tank's laterals.

Figure 45 shows the gamma detector used in 2005 gross activity monitoring and preliminary kinematic analysis. The modules are about 2-inches in diameter and 18 inches long. The total weight for the four segments was approximately 13 pounds, including the sensors, electronics, connectors, wiring between sensors, and sensor housing.

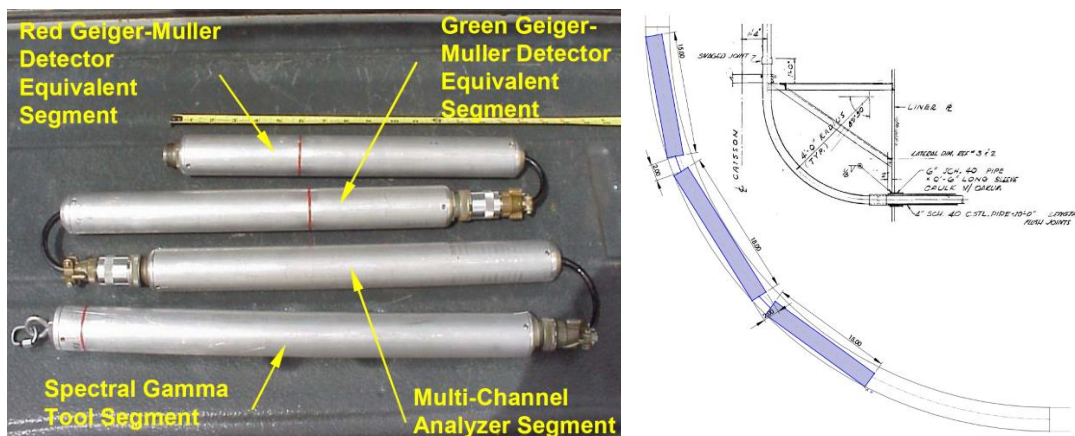


Figure 45. Gamma logging sonde detectors.

Figure 46 shows the existing 4-inch pipe crawler that was originally designed to navigate through DST air supply lines and provide a visual inspection of the central tank plenum. Requested by WRPS, the system has been tweaked to navigate through the laterals, crawling the vertical lines connected by 4-foot radius bends to horizontal lines running under the tank. The tweaking in the existing system consists of streamlining the overall crawler design, retrofitting the embedded electronics, integrating payload, and incorporating automated cable management.

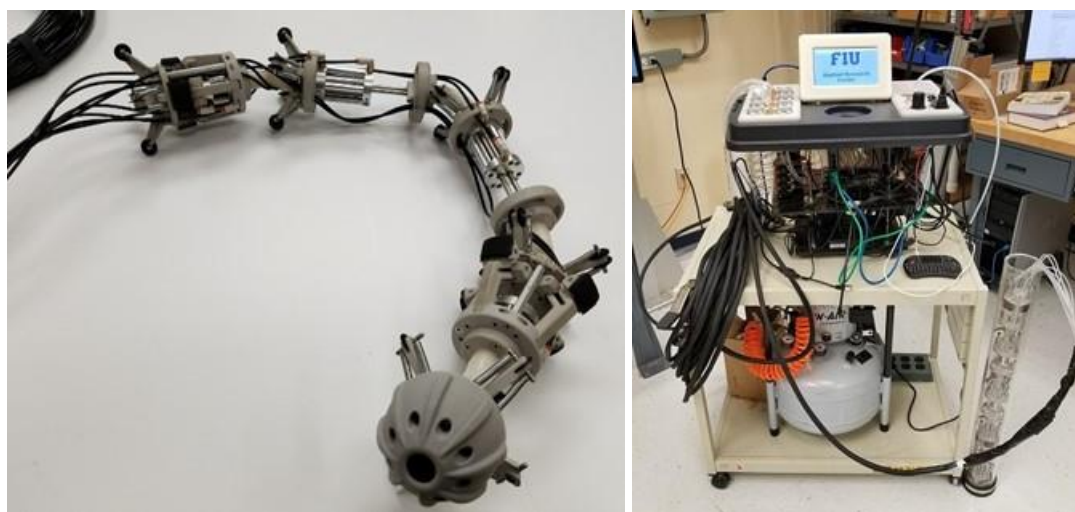


Figure 46. FIU's existing 3-inch crawler.

To demonstrate the technology potential, FIU has coordinated with WRPS site engineers to deploy the tool at Hanford's tank farm. As illustrated by Figure 47, the tool will be deployed at the lateral shacks by WPRS' site technicians and operated remotely by FIU scientists during the proposed demonstration.

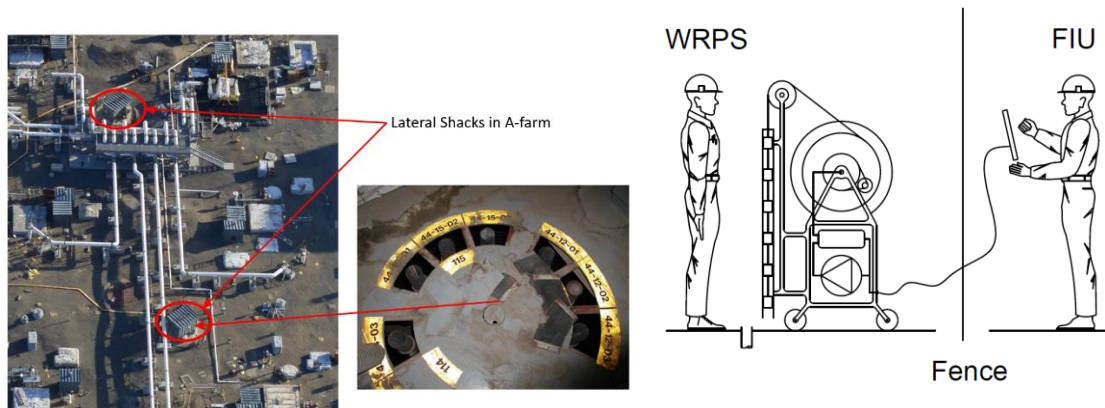


Figure 47. Proposed demonstration deployment at Hanford.

The coordinated efforts include a series of testing procedures to prepare for the demonstration at Hanford's Tank Farm, starting with laboratory bench-scale tests and in-house full-scale tests at FIU, leading to an initial deployment at WRPS' Cold Testing Facility this upcoming Fall. The overall functionality and robustness of the inspection tool will continue to be improved along with each subsequent test.

Crawler Design Streamline

As shown in Figure 48, the module guides were streamlined, and the two gripper and two extender modules were fitted with more robust components. The crawler guides were oriented toward the 3-inch diameter, expanding to a natural position in a 4-inch pipe. The guides contract with the reach of the extended members and fold flush into the crawler.



Figure 48. Crawler current design.

The guide mechanism consists of a torsional spring, two support arms, the guide, and a block to join the assembly to a flange. Compared to the previous suspension, this version is similar in function; however, it is much more modular and has a greater range of motion. It folds flush to the crawler modules and does not compromise room between units, potentially freeing up space for bends or unexpected obstacles in the pipe.

Efforts were also focused on managing the pneumatic line powering the pistons throughout the crawler's modules and routing wires for cameras and eventual sensors. In the current improved

design, the pneumatic tubes and electrical wires run in holes drilled in the pneumatic cylinders' flanges, concealing and keeping lines away from moving parts and preventing collisions with the modules' guides or the guide gripper's locking mechanism.

All dowel pins that hold the gripper module's arms were firmly secured with set screws attached to heat sets embedded on the frame. The redesigned locking mechanism is robust to cyclical loading compared to threaded standoffs used as down pins in previous versions.

The intermodular flexible connection was also redesigned. Figure 49 illustrates the new connections that enclose the supply lines streamlining cable management.

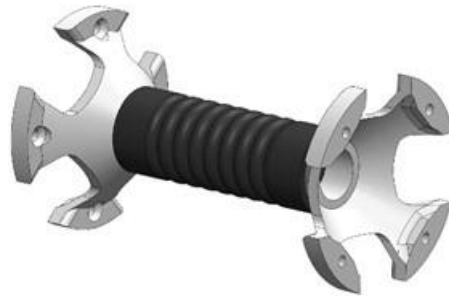


Figure 49. Redesigned intermodular flexible connection bellows.

A quick-disconnect module shown in Figure 50 was designed to disconnect the pipe crawler from the tether. The main housing (large cylinder) seals the components with a lid secured by four screws along the circumference. Tubes and wiring will remain within the crawler to avoid removing each pneumatic fitting. The steel rope will be secured with two loops, the tether and the crawler's, joined with a shorter length than other cables to ensure tension is only on the steel cable.

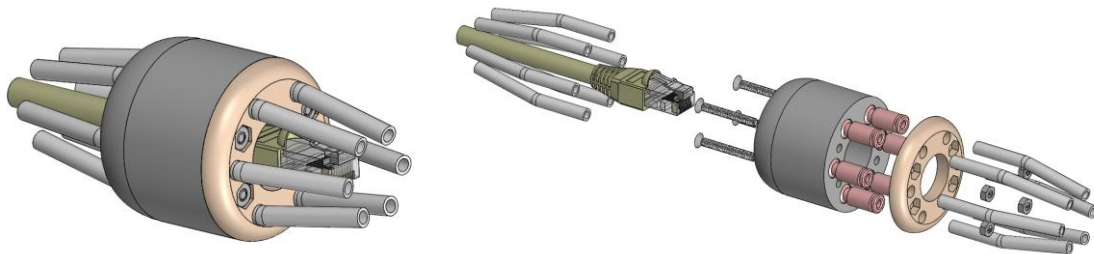


Figure 50. Tether quick-disconnect for quick detachment.

Retrofitted Embedded Electronics

As illustrated in Figure 51, the unit is tethered by a Category 6 Ethernet cable, which provides data communication, video feedback, supplies power to the embedded computer and its onboard auxiliary electronics. All embedded electronics are hosted in a front camera module. The front module uses the same hardware and software architecture retrofitted from the secondary liner crawler.

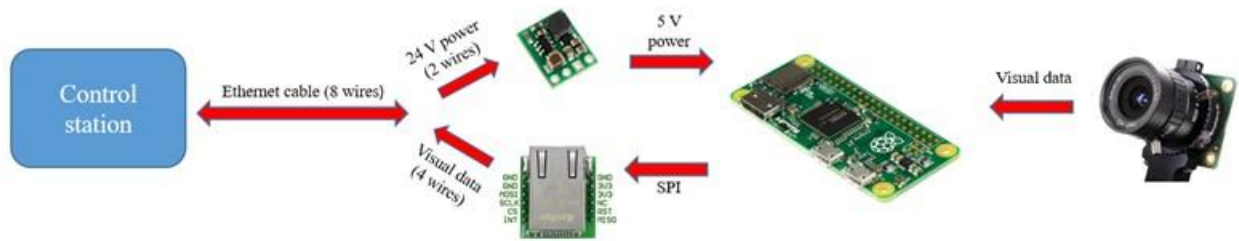


Figure 51. Crawler's power over internet data transmission.

Each module has also been equipped with Inertial Measurement Units (IMU) for attitude estimation, fusing data from accelerometers, gyroscopes, and magnetometer, as sketched in Figure 52.

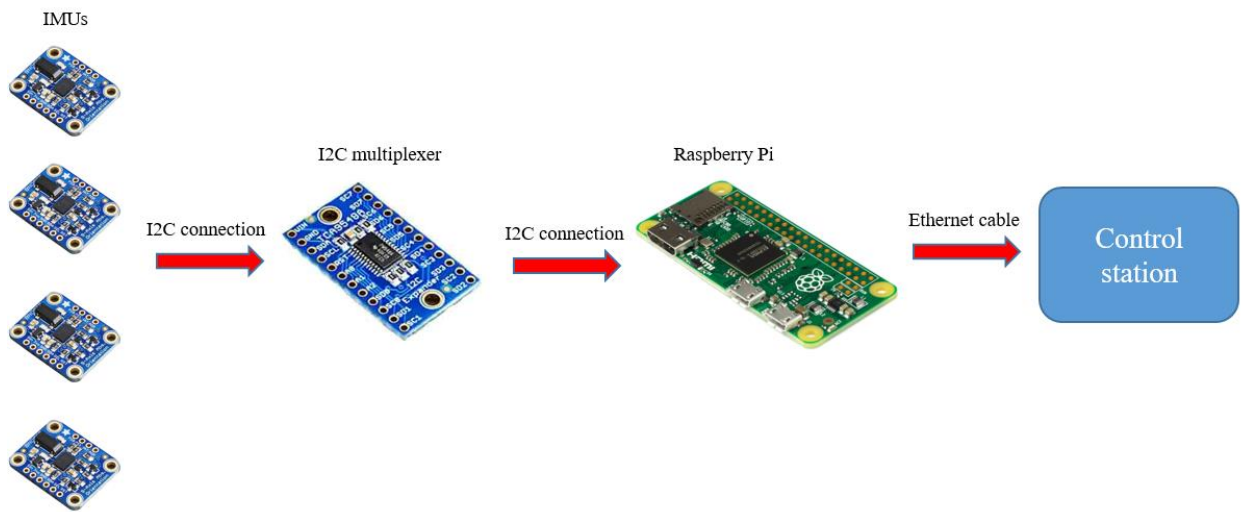


Figure 52. Schematic of IMUs communication

Mockups and Testing

Exhaustive bench-scale and full-scale tests were designed to verify and validate the inspection tool. Testing combined several different scenarios ranging from jammed guide components to adverse weather. Figure 53 shows a full-scale mockup built at FIU to simulate the SST's laterals.

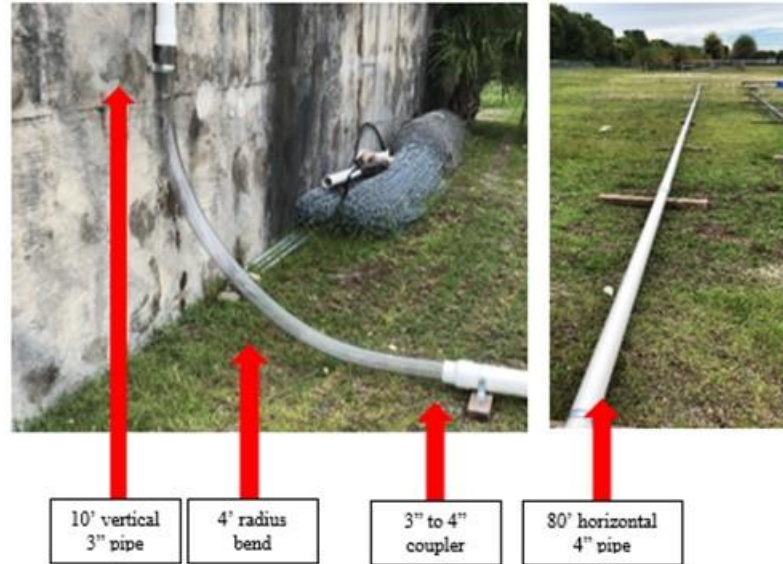


Figure 53. Pipe Crawler Full-Scale Mockup.

Subtask 18.2.4b: Results and Discussion

Figure 54 shows a functional prototype of the pipe crawler that has been rigorously tested to evaluate the unit’s behavior in realistic conditions.



Figure 54. Current pipe crawler prototype.

Figure 55 shows that the current guides improved by adding rolling bearings, significantly reducing contact friction.



Figure 55. Improved guides.

Figure 56 shows the electronics module located at the front end of the pipe crawler, currently housing a range finder, single-board computer, wide-angle camera, and a female Ethernet port. The single-board computer was successfully tested, receiving controls and transferring live video feed.

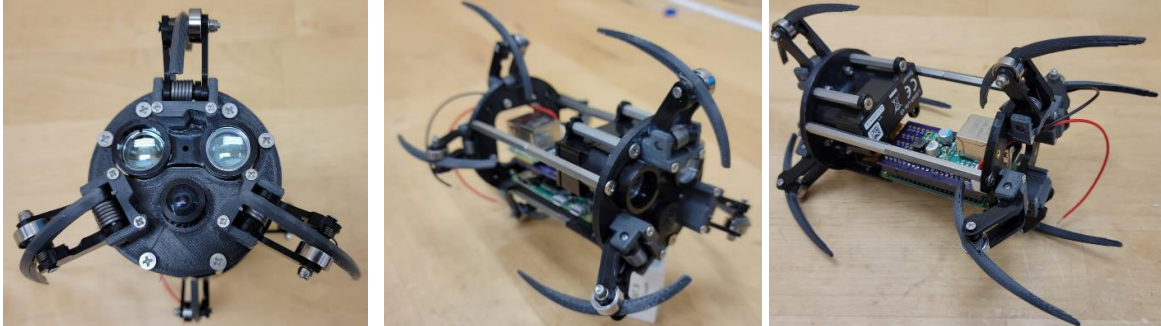


Figure 56. Electronics module with a forward-facing camera and range finder.

Figure 57 shows the pipe crawler successfully being tested in a bench-scale mockup. The mockup was originally designed to test other pipe crawlers developed at FIU.



Figure 57. Pipe crawler bench-scale testing.

Figure 58 shows a portable control box retrofitted to test the pipe crawler.



Figure 58. Pipe crawler portable control box.

Figure 59 shows a motorized tether reel that has been automated to deploy the inspection tool.



Figure 59. Tether reel and potential slip-ring.

Figure 60 shows the integration, disassembly, drilling and reassembly of a slip-ring to provide an Ethernet connection to the reel drum and consequently power the pipe crawler during the deployment.



Figure 60. Ethernet slip-ring integration.

Figure 61 shows the tether assembly with six pneumatic lines, an Ethernet cable, and a retrieval steel wire. The tether will be sleeved using a polyester fray-resistant expandable sleeve.



Figure 61. Tether assembly.

Subtask 18.2.4b: Conclusions

The design efforts will continue streamlining the gamma scanner's delivery pipe crawler. The improvements will include fully automated cable management and payload integration. Based on estimated geometry and weight, a prototype of sensory payload modules will be designed and seamlessly integrated. There are also plans to integrate additional sensory, such as a lidar module, for pipe surface mapping, a temperature, and a humid sensor for environment characterization. Eventual modifications will be made based on the engineering-scale test results, incorporating Hanford deployment requirements coordinated with the site engineers.

Subtask 18.2.4b: References

1. Randall, R. and Price, R. K., 2006, Gamma Surveys of the Single-Shell Tank Lateral for A and SX Tank Farms, CH2M Hill, RPP-RPT-27605, Rev. 0.

Subtask 18.3: Evaluation of Coatings for the H-Canyon Exhaust Tunnel

Subtask 18.3: Introduction

The H-canyon is the only remaining chemical processing facility in America capable of reprocessing plutonium, highly enriched uranium and other radioactive materials [1]. The exhaust air flow from the H-canyon chemical processing areas and HB-line are transported through the H-Canyon Exhaust (HCAEX) tunnel, where radioactive contamination is removed. Robotic inspections of the tunnel have revealed significant ongoing degradation of the reinforced concrete structure that was associated with acid attack. The degradation observed could compromise the mechanical strength of the structure. Hence, the search for solutions to mitigate and prevent further degradation is necessary [2-3]. The application of a protective coating on the degraded tunnel walls could mitigate and prevent further degradation, which constitutes the main goal of this investigation. This research effort has been divided into two phases: 1) Development and evaluation of aged concrete under accelerated aging conditions and 2) Evaluation of potential coatings applied on aged and non-aged concrete under simulated aggressive conditions.

In the preliminary stage of the investigation, a comprehensive literature review was performed and major findings included: 1) the characterization of the tunnel degradation conditions, 2) the identification of the chemical attack and erosion as the primary degradation mechanisms affecting the tunnel concrete walls, 3) the identification of the acid-type immersion tests as a well-known method for evaluating the materials' resistance to acid attack and, 4) the preliminary selection of potential coatings for aggressive environments similar to the tunnel [3].

Lessons learned and research findings of the initial testing of concrete in acid solutions supported the development and ongoing execution of a comprehensive test plan that will be presented in this report. The test plan execution is an ongoing task allowing the development and evaluation of aged concrete surfaces, with 1) protruded aggregates, 2) exposed steel rebar, and 3) chemically damaged, similar to the tunnel walls after more than 60 years of operation. The degraded (aged) concrete surfaces were developed through various accelerated aging conditions including the effect of some variables such as acid concentration, erosion, mode of action of the aggressive agent, and the presence of steel rebar [3]. Finally, the developed aged concrete surfaces will be used as the substrate for the evaluation of potential coatings in a further stage of the investigation. Because this is an ongoing investigation, preliminary results of the accelerated aging of concrete specimens will be presented in this report.

Due to the hostile environment of the HCAEX tunnel, the ability to enter the tunnel and perform any type of investigative, or in this case damage mitigation to the concrete walls, have been restricted to the use of robotic platforms equipped with the tools necessary to accomplish said goals. The robotic platform would need to work in tandem with another larger ground platform capable of traversing the difficult terrain of the tunnel. The ground platform would need to deploy the secondary platform onto the concrete walls to apply a down selected coating.

The secondary robotic platform will need to be capable of traversing the HCAEX tunnel concrete walls in a manner that does not further damage the surface of the walls and allows accurate positioning of the platform to apply the coating. A literature review regarding the different methods

available that would allow a mobile platform to maintain contact with the walls, regardless of the platform's orientation, will be highlighted in this report.

After developing and testing a single fan-based platform, which creates the appropriate adhesion mechanism, the results obtained from constructing a multi-fan omnidirectional platform will be detailed in this report. The goal of the report will also be to show the viability of the platform as an option to a unit capable of traversing a concrete surface without introducing further damage to the wall's surface and at the same time, maneuvering across the surface to reach a desired location when tele-operated.

Subtask 18.3: Objectives

The primary objective is to develop a robotic mobile platform capable of traversing vertical walls with varying surface conditions and applying a coating to the walls with the aim of preventing further surface degradation inside the HCAEX tunnel. The aim is to develop a robotic mobile platform capable of traversing vertical walls with varying surface conditions using a thrust based adhesion mechanism [4,5].

A scaled mockup concrete wall will be constructed using the information from Savannah River Site engineers, and the platform will be evaluated for its ability to maneuver along walls with varying surface conditions. The performance of the platform will also be quantified and used as a baseline to compare to future iterations of the platform as improvements are made during the project cycle.

The platform will be equipped with a coating application system which will be developed for the purpose of applying a selected coating to the concrete walls of the HCAEX tunnel. The application system will be designed to be modular in nature so that it can be incorporated into mobile platforms of varying sizes and configurations.

Subtask 18.3.1: Development and Construction of an Omnidirectional Robotic Mobile Platform

Subtask 18.3.1: Methodology

A platform that included a 90mm electronic ducted fan (EDF) was developed and evaluated for its ability to adhere and traverse along the a concrete surface. The single EDF unit, depicted below in Figure 62, was tested on a small-scale wall mockup with varying surface conditions. The single fan unit was also equipped with an IMU sensor to measure the roll, pitch and yaw of the platform. This sensor information will be used to autonomously control the thrust level of the EDF unit allowing the teleoperator to focus on maneuvering the platform to a desired location.



Figure 62. Single EDF based platform.

In addition to the IMU sensor, the platform is also equipped with a camera, motor encoders, smart motor controller, front light source and onboard processing. Figure 63 gives an overview of the existing technology and capabilities of the single EDF platform. The system is designed to operate via a connected ethernet line or via Wi-Fi and makes use of a middleware ROS for seamless sensor and package integration. ROS provides a paradigm called node, which allows for specific topics or data to be accessed remotely and then processed for an informed action plan. The single EDF unit was also equipped with larger wheels with protruding treads for robustness and adaptability over a surface with varying conditions.

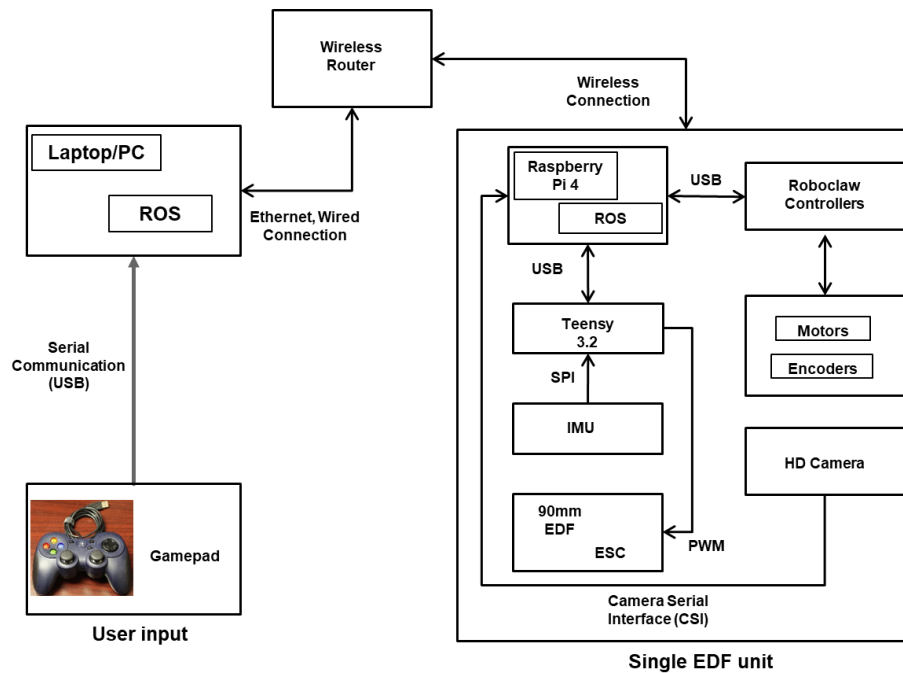


Figure 63. Control system breakdown for the single EDF platform.

With the duct fan approach validated, the next step was to adapt the working thrust-based technology to a multi-fan system capable of carrying larger loads during operational use. The system is detailed in a CAD design, Figure 64, with the aim of minimizing material usage on the

platform and reducing the unit’s weight. Minimizing the weight of the platform increases the payload factor of safety and allows for the necessary systems to be integrated.

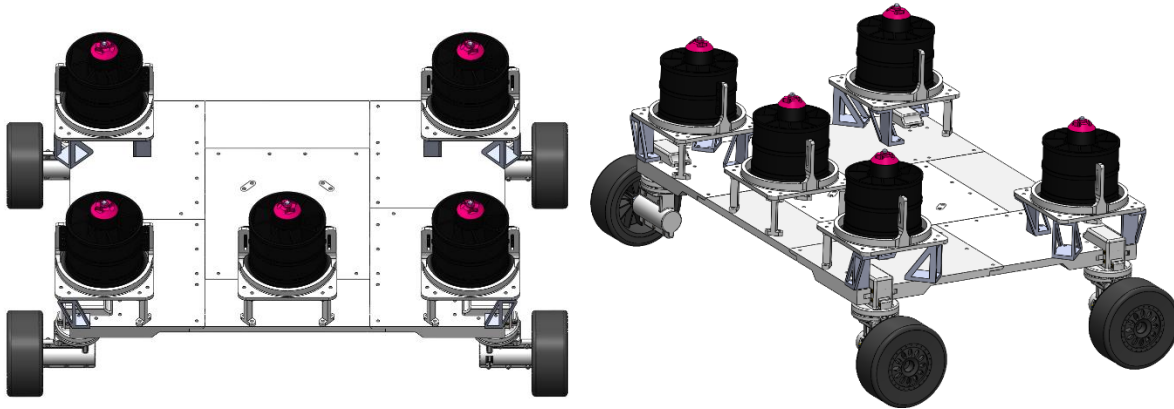


Figure 64. Multi-fan omnidirectional platform.

The multi-fan system was equipped with the same sensors as the single EDF unit platform along with multiple 2-DOF (degree of freedom) drive modules. These drive modules are designed to take advantage of multiple pre-programmed configuration changes which allows the platform to move along a surface omnidirectionally. The modules were also designed to minimize the deflection caused by the force of gravity acting perpendicular to the direction of motion after the platform has transitioned to a vertical surface.

A prototype was constructed of the multi-fan system once the CAD design was finalized. The larger unit consisted of five 90mm EDF units placed in a predefined configuration so as to offset the higher center of gravity and modular control system. The chassis of the system was 3D printed using segmented joints because of the print-bed size limitation. The unit dimensions are 16 inches in width, 22 inches in length and 5 inches in height. Figure 65 and Figure 66 show the fully assembled unit from different vantage points.



Figure 65. Top view of multi-fan platform with control box unit.

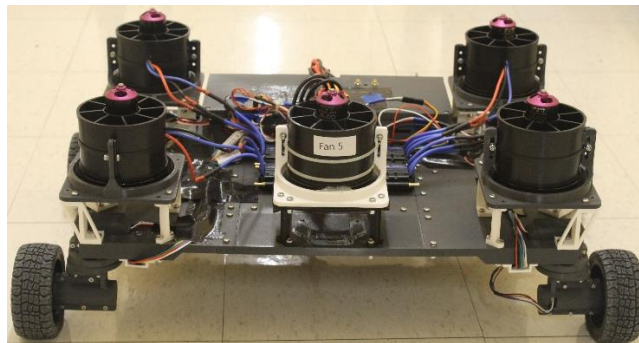


Figure 66. Front view of omnidirectional platform.

The control system for the multi-fan model was derived from the same system used in the single EDF platform but equipped with a higher end computer on a chip - Nvidia Jetson Nano - for onboard processing. The completed control box, Figure 67, is a self-contained system which was designed to be modular. It can function as a plug and play control unit, operating a variety of mobile platforms. The control box can connect and communicate with all the fans and sensors on the platform using a generated PWM signal and serial communication, respectively.



Figure 67. Completed control system unit.

Finally, a safety mechanism was designed and assembled in order to ensure the safety of the team and platform while performing tests. Unistrut pieces were assembled into a rectangular shape with legs which when placed over the top section of a wall ten feet in height, would self-lock. The system, Figure 68, was also equipped with two modified retracting mechanisms which can be locked into position remotely using pneumatic actuators.

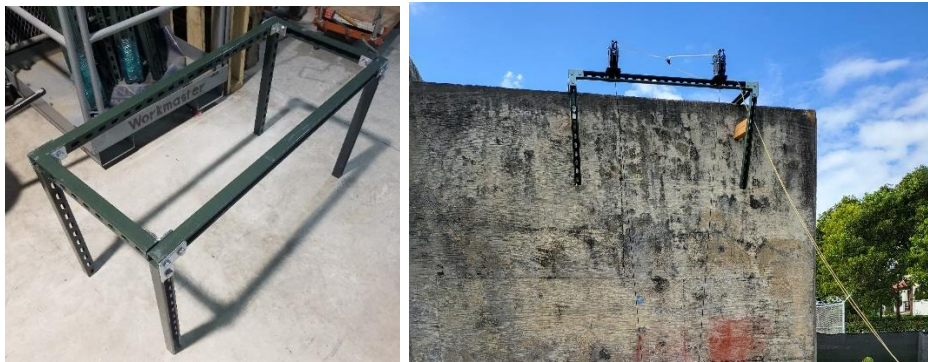


Figure 68. Self-locking safety mechanism secured on testing wall.

Subtask 18.3.1: Results and Discussion

The multi-fan system weighs 17 lbs and is able to generate a combined thrust force of 41.8 lbs when each EDF unit is operating at the maximum input voltage of 25.2V. Using these preliminary values, it was decided to attach individual power sources to each fan since it is not possible to continuously deliver 15.624kW of power to the platform during testing. Therefore, a simple setup using LiPo batteries, Figure 69, was used to power the system, allowing for 2-3 test runs before the batteries effected the performance of the crawler.



Figure 69. Power delivery setup to multi-fan platform.

Initial tests of the platform included test runs on multiple wall conditions ranging from smooth to pitted and rough surface conditions, Figure 70 and Figure 71. It was found that with the current setup of the platform (weighing 17 lbs), it was able to traverse and maneuver along the surface with the EDF units operating 80-90% of the full thrust capacity. This would fluctuate due to the voltage drop along the line. This problem was alleviated with the use of lower gauge lines for power delivery. This change, however, introduced another issue related to the mass of the tether line increasing to the point where it began to affect the performance of the platform.

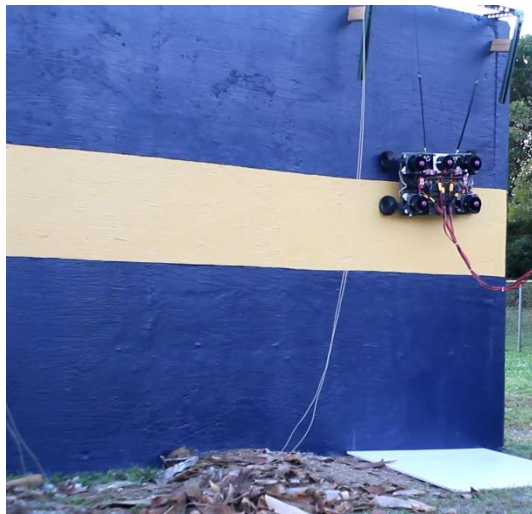


Figure 70. Smooth-like or pristine surface condition.



Figure 71. Rough wall condition with surface debris.

In order to increase the operational safety factor of the system, the 3D printed chassis was replaced with a new chassis fabricated from carbon fiber sheets, Figure 72 and Figure 73. The weight of the new chassis, along with lowering the number of screws and connections reduced the platform's weight by three pounds which in turn allowed the EDF units to operate at a lower thrust level. The reduced thrust level also leads to less power consumption when compared to data from previous test runs. Another benefit of the reduced weight is the lowering of the transverse force acting on the drive modules while adhered to a vertical surface. This leads to the drive modules experiencing less deformation, extending the operational time of the modules.

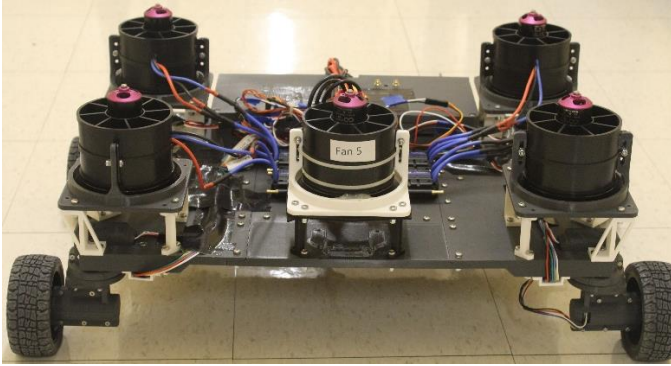


Figure 72. Multi-fan system with 3D printed chassis.

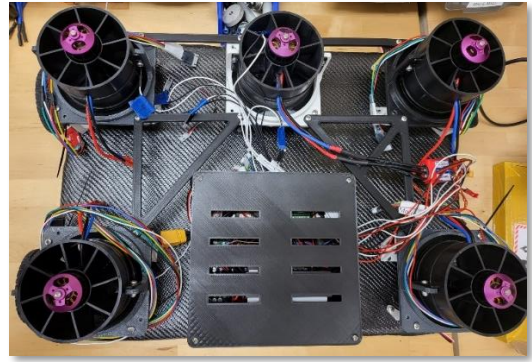


Figure 73. Multi-fan system with chassis fabricated using carbon fiber sheets.

Subtask 18.3.1: Conclusions

A platform capable of crawling along the surface of a concrete wall was designed, prototyped, and tested. The initial design concept used a single EDF to create the thrust necessary for the platform to adhere to a vertical surface. The technology was then expanded with five EDF units along with a 2-DOF drive module which gave the platform the capability of traversing the surface in any direction without needing to rotate the entire chassis. With the platform design and assembly completed, the control system was designed to improve on the sensor integration used with the single EDF platform. By also having a modular control system and independent platform, the ability to upgrade and improve the platform has become a simple process. After full system integration was completed, a pneumatic-based retracting mechanism was assembled to aid in the testing of the platform in accordance with lab safety guidelines. The system was then tested successfully and modified to improve its overall performance and operational factor of safety. Further design considerations for the platform will include incorporating vector thrust capabilities and using a supportive structure to aid in maintaining the restorative force needed to adhere to the concrete surface while the coating application is being utilized.

Subtask 18.3.1: References

1. Gilliam, Bob J., Ray, J., and Giddings, B. "Inspection and assessment of the H-Canyon ventilation system at The Savannah River Site". Phoenix, Arizona. s.n., 2015. Waste Management Conference.
2. Staff Report, Defense nuclear facilities safety board. "H-Canyon exhaust tunnel fragility analysis input and assumptions". 2018.
3. Echeverria, M., Nunez Abreu, A., Lagos, L., McDaniel, D. "Aging of concrete for the evaluation of repair materials to protect the HCAEX tunnel at Savannah River". Waste Management 2020 Conference, Phoenix, AZ, March 2020. (Best Poster of Track). Paper # 20301
4. Telusma, M., Natividad, J., Lagos, L., McDaniel, D. "Development of an Omnidirectional Wall Crawling Mobile Platform, Designed to Aid in the Repair of H-Canyon's Concrete Walls". Waste Management 2021 Conference, Phoenix, AZ, March 2021.
5. Lattanzi, D., Miller, G. "Review of Robotic Infrastructure Inspection Systems". Journal of Infrastructure Systems Vol. 23, Issue 3 (September 2017)

Subtask 18.3.2: Development of a Coating Application System

Subtask 18.3.2: Methodology

Two coating application system designs were developed with one actuated using a lead screw setup, Figure 74, as opposed to a timing belt construction, Figure 75. In the CAD design, there are two leads screws placed perpendicular to one another to allow the adaptor piece to move in a 2-DOF plane. This simpler design will allow for more accurate control of positioning and speed of the adapter piece.

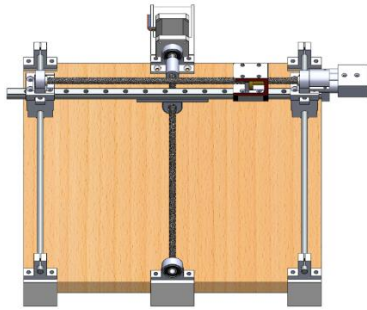


Figure 74. CAD design of coating mechanism.

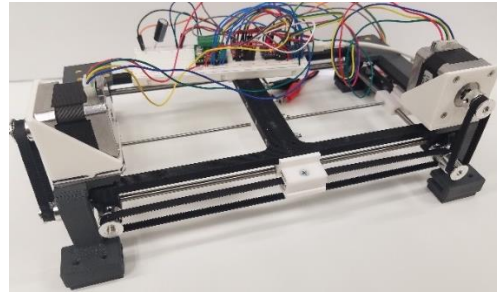


Figure 75. Timing belt and pulley-based coating application system.

A physical mock-up of the lead screw-based coating system was prototyped with the use of basic stepper motors as a placeholder for the motor which must be designed and built in-house for low weight, high torque, and speed control. A simple program was then written to test the initial setup for movement along with Y-direction, as depicted in Figure 76. The CAD design now includes the location of the second motor along with a design of the adaptor for securing a test piece (i.e., a camera or spray nozzle). Figure 77 shows the partially assembled coating mechanism which now includes multiple limit switches to initiate motor shutdown at the extremes and for initializing the system upon boot up.



Figure 76. Lead screw-based coating application system.



Figure 77. Partially assembled coating mechanism with portable power supply.

A CAD design of a motor module, depicted in Figure 78 and Figure 79, was created to have a motorized system capable of creating the necessary torque output in a small package. The dual rail system being used will need to be properly lubricated and protected from incoming dust and larger sized particles. With these protective barriers in place, the unit will allow the single center placed motor to initiate motion along the primary axis while still under load.

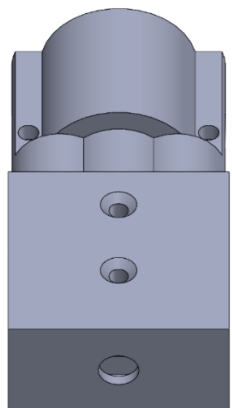


Figure 78. Enclosure unit for the secondary axis motor setup.

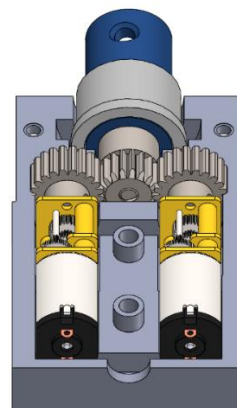


Figure 79. Internal configuration of the gear motor setup for the second axis.

The coating mechanism was further improved by adding limit switches to sections of the base to provide a secondary level of protection against over torque and over current draw due to interactions at the boundary. Figure 80 depicts the connection to the main mechanism and highlights the difference in motor sizes for each of the different drive directions. Figure 81 depicts the dual motor setup in a unique motor housing. The system is also designed to accommodate a gear setup for increased torque output, which will be one of several important parameters needed to ensure the smooth operation of the mechanism during the coating process.

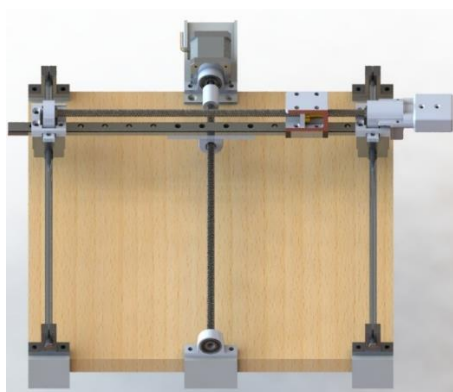


Figure 80. Coating mechanism.



Figure 81. New gear motor module.

Subtask 18.3.2: Results and Discussion

Meetings were held with multiple companies to obtain information regarding coating compounds that may meet the requirements for application in the H-Canyon tunnel. Three companies that provided information were Carboline Company, Sherwin-Williams and Belzona Coating Company.

Notes from the meetings with Carboline included:

1. Concrete surface being wet may pose an issue.
2. Mixing could be done at the nozzle tip depending on coating.
3. Surface preparation is required.
4. Importance of pot life and extending it.

5. Low pressure plural application.
6. Equipment and setup needed to remove the collected debris during surface preparation.
7. Suggestion for possible coatings.

Notes from the meetings with Sherwin-Williams included:

1. Mixing needs to be done in the pressure line instead of nozzle tip.
2. Surface preparation is key to a proper coating being applied with different methods being available:
 1. High pressure water (up to 140 kPSI)
 2. Abrasive blasting
 3. Vapor blasting
3. The suggested coating option is a two-part coating mixture.
4. Discussed the equipment needed along with being able to reach the full length of the tunnel.

Notes from the meetings with Belzona included:

1. For proper coating application a nozzle pressure of 3000 PSI is needed.
2. Multiple layers may be needed depending on the condition of the initial coating layer.
3. Surface preparation would entail leveling the surface to ensure an even coating thickness over surface or applying multiple coatings to increase coating thickness.
4. Mixing cannot be done at the tip but at the Mixing Manifold for proper component mixture.
5. The company has worked with other companies that have used their products via a robotic platform.

Subtask 18.3.2: Conclusions

In conclusion, due to the complexity of the issue of selecting the appropriate coating compound for initial testing, a mechanism capable of handling strong reactionary forces due to the coating process was developed. Further tests will need to be completed to determine the maximum load allowed before component, subsystem, or complete mechanism failure. To model the behavior of the system while under load, a simple system utilizing a load cell will be assembled and used to gather the required force data. Improvements will also be made to the overall design of the coating mechanism to reduce its weight and the number of failure points.

Subtask 18.3.2: References

1. Telusma, M., Natividad, J., Lagos, L., McDaniel, D. " Development of an Omnidirectional Wall Crawling Mobile Platform, Designed to Aid in the Repair of H-Canyon's Concrete Walls". Waste Management 2021 Conference, Phoenix, AZ, March 2021.

Subtask 18.4: Long-Term Surveillance of Nuclear Facilities and Repositories using Mobile Systems

Subtask 18.4: Introduction

Continuous surveillance of nuclear facilities and repositories is a critical element in successfully controlling and understanding radiological environmental impact, planning cleanup efforts, and meeting quality assurance objectives established by the U.S. Department of Energy standards and guidelines. When surveying nuclear facilities and repositories, advanced mobile surveillance systems are safe, efficient, and labor-saving tools that safely deploy state-of-the-art instrumentation without exposing workers to radiation risks. Given the large size of many facilities, coupled with the high cost of radiation sensors and the nature of radiological sources, mobile systems provide a cost-effective solution versus on-site sensor networks or monotonous routine measurements performed by site personnel. In addition, mobile systems deployed in more frequent periodic surveillance missions can provide continuous radiation measurements, simultaneously fusing data from several other embedded sensors, tracking long-term changes in the environment over time, which is needed to assess and document the condition of nuclear facilities during operation, decommissioning, and end state assessments.

In collaboration with Savannah River National Laboratory and Washington River Projection Solution site engineers, this subtask will investigate robotic platforms and state-of-art field-deployable sensory systems suitable for long term monitoring of nuclear facilities and repositories.

Subtask 18.4: Objectives

This task's primary goal is to investigate fully autonomous off-the-shelf multi-use robotics technologies adequate for surveying nuclear facilities and repositories across the DOE complex. Our investigations will pursue the following objectives:

- Develop an agnostic field-deployable sensor package coupled with a robust autonomous radiological survey framework to be deployed at Hanford's mobile platforms during summer.
- Continue customizing and testing in-house ground and aerial mobile platforms, integrating perception sensors to navigate nuclear facilities, developing digital twins, and fusing data from synthetic gamma measurements, surrounding imagery, and LiDAR mapping.

FIU will also employ geospatial data analysis frameworks driven by Machine Learning into our in-house autonomous radiological survey framework in the upcoming performance year. These frameworks will provide site engineers with tools suitable for automating the analyses of massive amounts of data collected over time in subsequent surveillances.

Subtask 18.4.1: Surveillance Literature Review and Assessment

The subtask's primary goal is to automate routine radiation surveillance tasks of exiting nuclear facilities and repositories using fully autonomous mobile platforms. The efforts started with a comprehensive literature review providing insights into the project's significant aspects, such as stochastic processes for spatial data, uncertainty modeling theory, decision-making algorithms, radiation quantification, measurement, and modeling. At the same time, the DOE Fellows working

on the project received hands-on training on diverse topics in robotics, including the Robot Operating System (ROS) and essential point cloud data processing, usually not part of traditional engineering curriculums.

Subtask 18.4.1: Methodology

Conventional methods of taking radiation measurements by hand within or around the containment areas and analyzing the collected data to obtain the result are ineffective and put scientists at risk of unnecessary radiation exposure. On the other hand, the current state of autonomy for field-deployed autonomous radiological survey systems is mobile robots with waypoint navigation capabilities. Usually, a scientist selects a series of waypoints on a map, directing the robot to travel autonomously between points. Advanced systems often support obstacle detection and local collision avoidance using LiDAR imagers. However, current surveillance robots in nuclear facilities and repositories do not have a high degree of onboard autonomy to cope with dynamic environments changing over time due to operations, weather events, and site deterioration currently presented in DOE sites.

As exemplified by Figure 82, changes in Hanford's Tank Farm due to retrieval operations [1] and the constant need to manually reconfigure the surveillance mobile platform's mission plan could become a burden to site engineers, which would also be the case in analyzing the captured data over time.



Figure 82. Hanford's Tank Farm retrieval operations in September 2016 (left) and 2018 (right).

The proposed methodology expands traditional autonomous navigation frameworks implementing a novel onboard information-driven planning and control tailored to radiological surveillance of large facilities. The online adaptive planning algorithm [2] takes into account not only navigation goals and battery constraints but also includes sensing objectives such as increasing coverage and routing the optimal path that would decrease the uncertainty in the overall radiation map as well as reduce geometric uncertainties in the mapped environment over time. The framework will also implement basic terrain risk-awareness and advanced perception, a crucial issue in taking fully autonomous surveillance systems out of the structured laboratory and mockup environments and deploying them into existing facilities and repositories.

The core areas of development of FIU's Mapping and Robust Localization Framework are:

- 1) information-driven planning and control in radiological environments,
- 2) terrain risk awareness in dynamic and unstructured environments, and
- 3) advanced perception in complex environments.

Information-driven planning and control in radiological environments

The proposed framework uses fully autonomous robots as intelligent agents, sensing locations, actively defining an optimal sequence of consecutive measurements and controlling acquisition parameters of the radiation sensor in real-time, basically dwell time and surface proximity, with the objective of improving the accuracy of the radiation map, addressing common issues with irregularly spaced, noisy, low count data, obstructions, and existing background radiation.

Terrain risk awareness in dynamic and unstructured environments

The proposed framework implements a computer vision module, assisted by a semi-supervised machine learning system, that uses video images from surrounding cameras to classify the terrain conditions of the floor segmented by LiDAR data elevation. A convolutional neural network is trained to classify surface types (carpet, vinyl, water, grass), where unknown conditions (low classification probability) are treated as obstacles. Unknown surfaces can be later manually classified by an operator bringing a human in the loop. The terrain awareness improves over time in the proposed framework, keeping the platforms safe in unexpected floor conditions, which is critical in unsupervised robots working in outdoor repositories, especially after weather events.

Advanced perception in complex environments

The proposed framework uses several heterogenous imaging sensors and gamma radiation detectors to construct an immersive environmental map, as illustrated by Figure 83. The framework stores high-resolution maps for digital twin reconstruction and keeps reduced-order ones for navigation and control. The framework also innovates using a robust localization algorithm fusing many sources of odometry (basically ICP, IMU, and visual), suitable in monotonous environments such as hallways and tunnels.

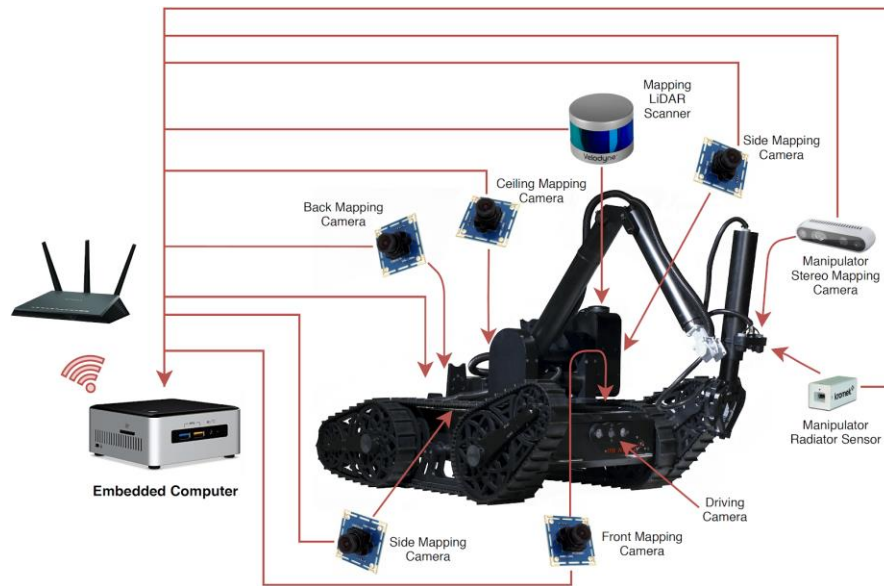


Figure 83. Mobile platform integration.

Robotics Platforms

Figure 84 shows the handheld, ground, and aerial mobile platforms used in our in-house tests. The platforms have been customized, integrating several perception sensors to navigate nuclear

facilities, and generate high-fidelity tridimensional digital twins fused with radiation measurements simulated using synthetic gamma sensors.



Figure 84. FIU's mobile platforms.

Virtual Radiation Sensing Framework

The framework has been developed using synthetic radiation fields, virtual sources, and simulated sensors. During tests and in-house deployments, simulated radiation sensors mitigate the lack of strong radiation sources and relevant radioactive environments at FIU.

Subtask 18.4.1: Results and Discussion

Along with the research, the subtask developed in two major areas:

- a) radiation mapping framework development, and
- b) digital twin capture and reconstruction.

Virtual Reality (VR) and Augmented Reality (AR) were also incorporated into the immersive visualization of captured geospatial datasets.

Radiation Mapping Framework Development

Figure 85 shows indoor and outdoor topographic scans using a mapping framework developed at FIU in previous projects. The seed framework captures point clouds using LiDAR and colorizes them, registering video images from surrounding cameras. The images also illustrate the importance of color perception in feature detection, object recognition, and comparative analyses over time. Combining an efficient navigation algorithm with a robust visual mapping is the foundation for automating the long-term surveillance of facilities and repositories using mobile robotic systems.

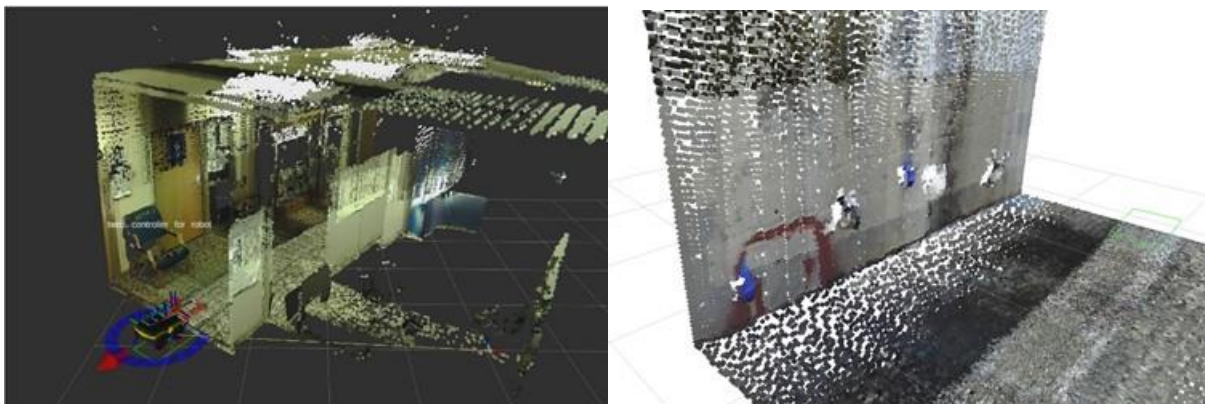


Figure 85. Indoor (left) and outdoor (right) colored point cloud topographic maps.

3D Cameras Integration

Figure 86 shows an Intel RealSense D435 depth camera integrated into FIU's Jackal mobile platform to capture dense colored point clouds. There are plans in the framework to fuse close-range data captured by 3D cameras with mid-range ones imaged by LiDAR, combining local accuracy with far-field awareness.

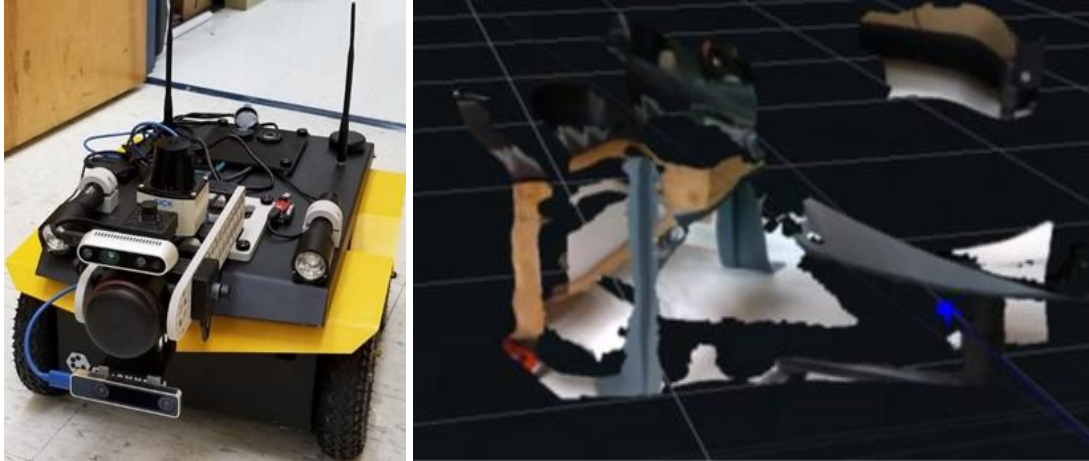


Figure 86. High density colored point cloud from Intel Realsense D435 Depth Camera.

The depth camera was mounted to a lower spot on the mobile platform, improving navigation and capturing floor-level obstacles. After the sensor location tweaking, the robot successfully detected lower height obstacles such as the toolbox shown in Figure 87. Objects with lower height, such as chair legs, were not previously detected by the navigation framework.



Figure 87. Improved object detection.

The framework was enhanced by integrating frontier-based autonomous navigation capabilities. Frontier-based navigation allows the robot to explore, without human input, eliminating new boundaries as it goes, as illustrated in Figure 88.

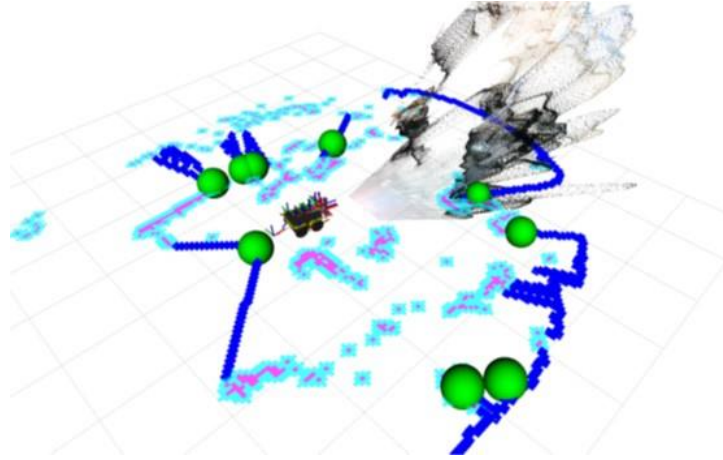


Figure 88. Environmental mapping using the installed depth camera.

The ROS node responsible for frontier-based exploration was also further streamlined and tested to ensure that the mobile platform maps the unknown areas without spending too much time in small and cornered locations.

Figure 89 shows a map capture in the hallway outside the robotics lab. There are plans to construct large-scale maps of the second floor and outdoor parking. The plan also includes implementing multiple depth cameras, improving the SLAM quality, and increasing the level of detail in our maps.



Figure 89. Preliminary hallway map.

Improved Indoor Localization

Our previous localization algorithms rely on sensory fusion odometry from wheels, visuals, and Inertial Measurement Units (IMU), poised by eventual dead reckoning inaccuracies. Adding a 3D camera to our localization algorithm has improved our environmental maps' accuracy, such as in Figure 90. The improved odometry algorithms also incorporate colored point clouds from 3D cameras fused by the Real-Time Appearance-Based Mapping (RTAB-Map) application, which minimizes inaccuracies implementing loop closure in its simultaneous localization and mapping (SLAM) algorithm.



Figure 90. Improved captured map by fused data from a 3D camera.

A line publishing node was implemented to compare different sources of odometry. The sources included the RealSense tracking camera, the depth camera using a simultaneous localization and mapping (SLAM) algorithm, the IMU, and the wheel encoders. Different source combinations were fused and tested by further mapping with the Jackal inside the laboratory. A different odometry fusion ROS program was used, resulting in smoother robot movements. Although the indoor localization issues have been worked on for quite some time, a robust algorithm is crucial for producing high accuracy maps, especially in large environments where sensors possibly deteriorate over time. Overall, the wheel encoder odometry contributes negatively to the localization process. To improve outdoor localization, a global positioning system (GPS) with real-time kinematic positioning (RTK) technology, shown in Figure 91, has been tested for precise outdoor localization. RTK techniques increase the accuracy of GPS positioning using a fixed base station that wirelessly sends out correctional data to a moving receiver providing up to centimeter-level accuracy.

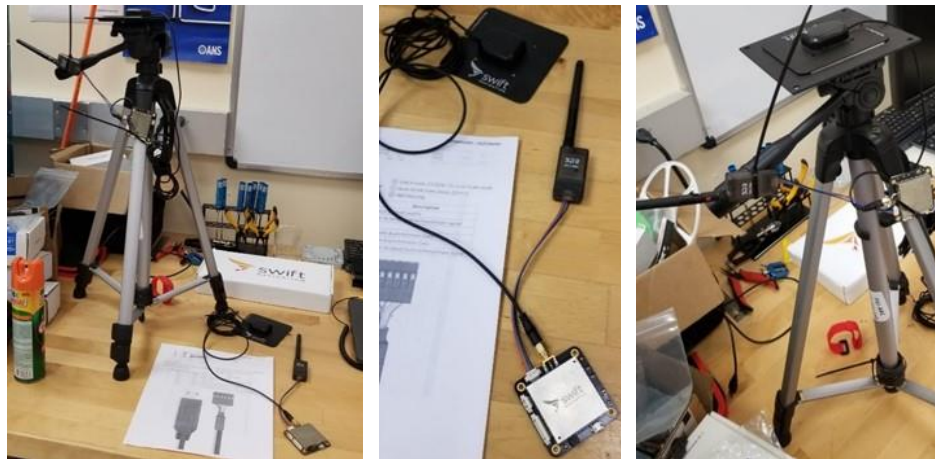


Figure 91. RTK GPS (left), mobile unit (center), and fixed base station (right).

Waypoint Indoor Surveillance

An essential feature in autonomous mobile surveillance systems is implementing robust waypoint navigation. Waypoint navigation is the ability to provide a robot with a set of waypoints (usually GPS latitude and longitude pairs when outdoors) and have the robot autonomously navigate its current location to each of the following defined waypoints in sequence. Robotic platforms usually use an active collision detection and avoidance strategy tackling obstructive geometric features captured during mapping along the way.

Figure 92 shows a preplanned path (green lines) used to tune and evaluate our autonomous mobile platforms' indoor waypoint (red dots) navigation. The chosen route is a loop leaving our laboratory, navigating the hallways, and returning to the starting position. The data captured from routine surveys along this path will develop and test digital twin and "time machine" algorithms over time at FIU.

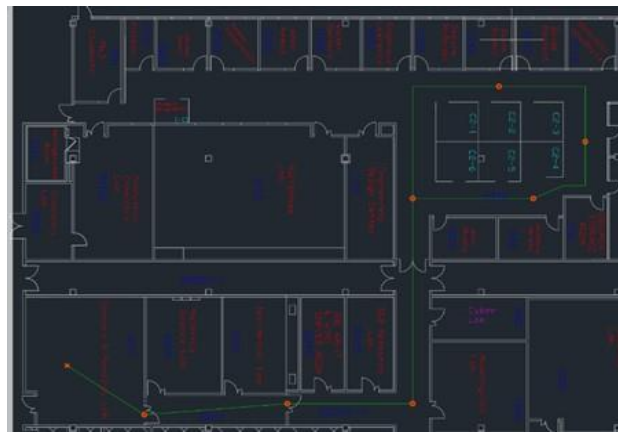


Figure 92. Waypoint autonomous surveillance.

Figure 93 shows a preliminary test of our waypoint navigation algorithm. The red arrow is the next pose in space that the platform is attempting to reach, and the green line is the current local path plan.

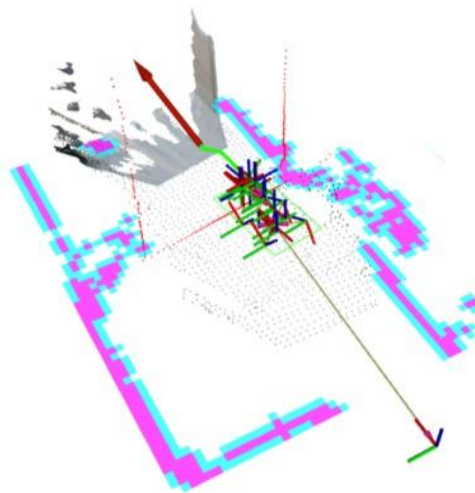


Figure 93. Waypoint navigation algorithm preliminary test.

Multichannel LiDAR Integration

A mid-range LiDAR was integrated into our small mobile platform, designing custom-made brackets 3D printed in ABS thermoplastic. The 32 vertical beams LiDAR, shown in Figure 94, replaces a previous single beam LiDAR, significantly improving our mapping capabilities and resolution. One of the platform's embedded computers was also upgraded to be more suitable for computer vision and machine learning. The upgraded onboard computer significantly improves the platform's overall computational and mapping performance.



Figure 94. Mid-range LiDAR integration.

Figure 95 shows maps with significantly improved accuracy due to the dense point cloud captured by the high-resolution LiDAR. A denser cloud is suitable for implementing an Iterative Closest Point (ICP) scan matching algorithm, ideal for autonomous mapping in large indoor environments, where issues related to error build-up and deviation in further out locations are significant. ICPs algorithms estimate poses between successive sensor images, potentially giving more accurate measurements than traditional odometry techniques.

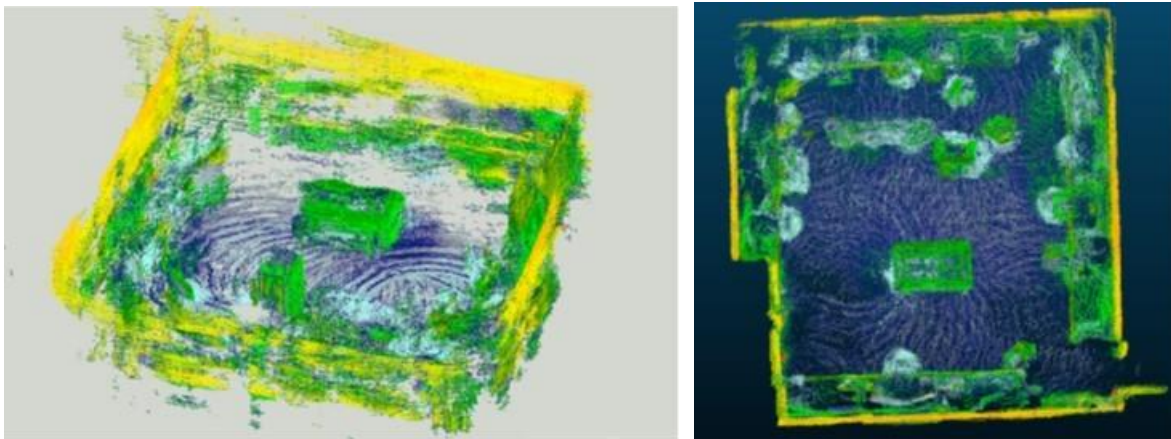


Figure 95. Original ICP point cloud (left) and improved map fusing IMU (right).

Figure 96 shows a map captured from the robotics laboratory's hallways, demonstrating the improvement in long-distance surveys and minimal distortion in right-angle turn, captured as obtuse corners in previous mappings.

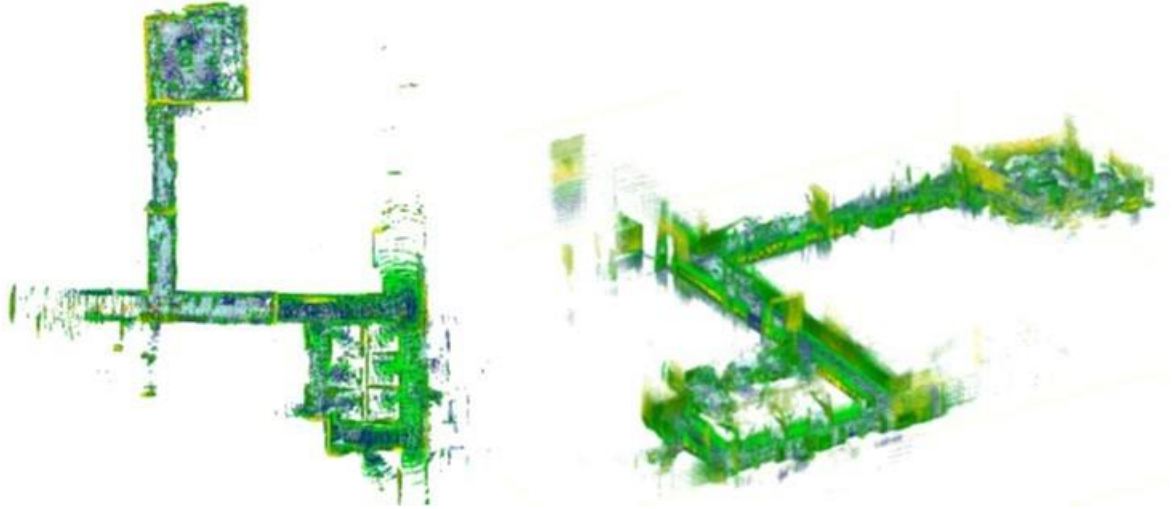


Figure 96. Captured maps from FIU's corridors.

Figure 97 illustrates that our mapping framework needs further tweaking in areas with fewer geometric features despite the improvements. As highlighted, in the case of a specific small hallway, a jump occurred due to loop closure failure in the localization algorithm.



Figure 97. Closed loop failure in the localization algorithm.

State Machine Integration

Figure 98 shows a state machine implemented for a robot equipped with a Geiger radiation sensor by the Fellows during the summer internship at Hanford. State Machine algorithms allow the robot's navigation to interrupt or change in real-time, which helps take radiation measurements for varying durations of time to measure in a single spot, currently being tested at FIU.



Figure 100. Handheld mapping device and captured raw datasets.

Figure 101 shows a preliminary digital twin reconstructed from multiple raw datasets captured with boxy. The raw point clouds were preprocessed in CloudCompare, using several cleaning and filtering algorithms, including Statistical Outlier Removal (SOR) and noise filter, duplicate point, and floating-point removal. Filtering by simple feature (SF) values was also tested to reduce the density and noisy points. The point clouds registration used the picking point pair method for rough registration and ICP for fine registration. The ICP algorithm searches for the nearest points in two adjacent scans and calculates the transformation parameters, but it still requires rough registration before using it. The root means square (RMS), which is the remaining distance between two scans, was minimized tremendously using the ICP algorithm. After merging the dataset scans, the overlapped sections were carefully removed, producing smooth and coherent digital twins.



Figure 101. Processed data after cleaning and registration.

Figure 102 compares different sources of odometry. However, due to instabilities in the localization algorithms, visual odometry gets lost quickly when the mapping device moves with great speed.

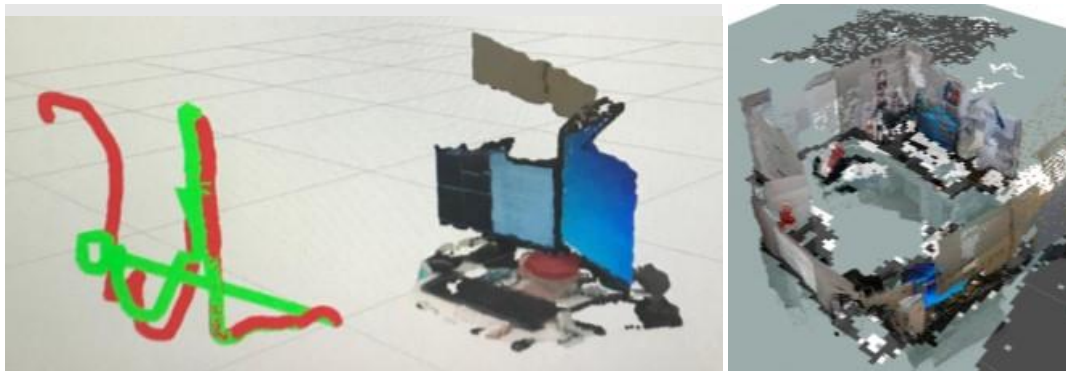


Figure 102. Path of different sources of odometry.

Figure 103 shows CloudCampare's surface reconstruction algorithm preliminary results, generated by the Poisson Surface Reconstruction and Ambient Occlusion algorithm. Surface reconstruction from large-scale sparse point cloud data efficiently reduces computationally expensive dense digital twins [6]. However, these algorithms are not entirely solved and problematic in incomplete, noisy, and sparse data.

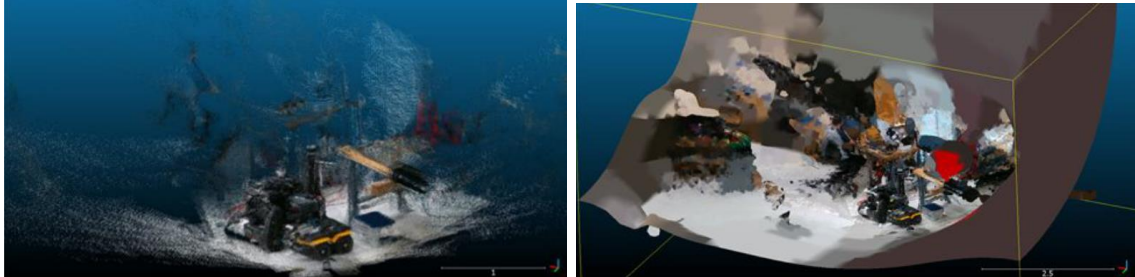


Figure 103. FIU's Robotics Laboratory original point cloud (left) and reconstructed surfaces (right).

Figure 104 shows improvements made to boxy, which has been instrumental for point cloud capturing and testing the performance of sensors and algorithms. The improvements include integrating two additional depth camera models and a solid-state LiDAR into the handheld device. The additional sensors' performance was tested and compared with the existing ones mapping different environments.

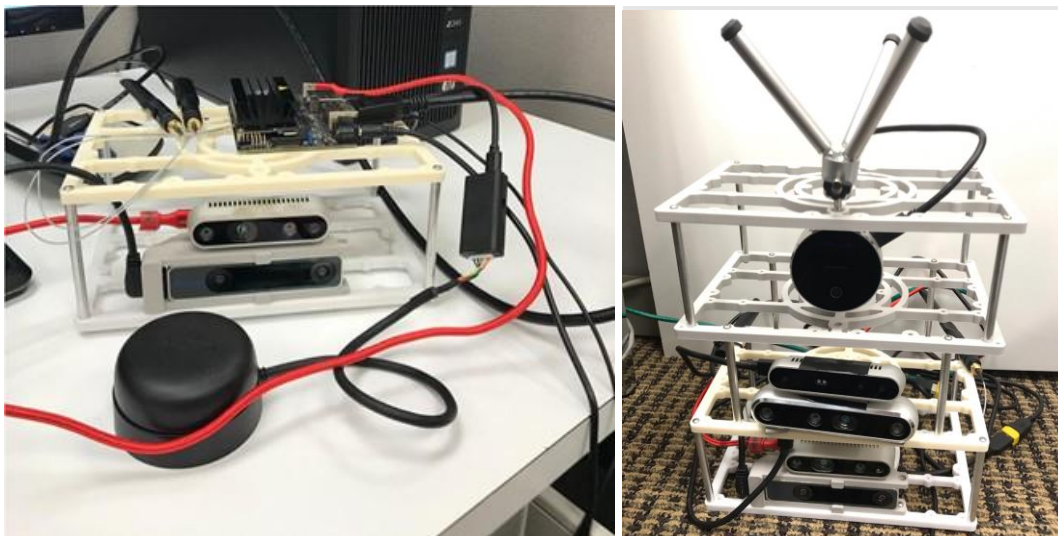


Figure 104. Original (left) and improved (right) "boxy" handheld mapping device.

Previously, our evaluations of preprocessing algorithms, such as the SOR filter, were based on changes in appearance and visual interpretation rather than proper statistics quantification. However, roughness, surface variation, and planarity, among other metrics, are robust statistical dispersion measures that quantify point reliability in captured cloud datasets. Thus, our reconstruction started incorporating thresholds based on these statistical features to improve the quality and reliability of captured surfaces.

Figure 105 shows a surface variation distribution histogram of a point cloud dataset before and after preprocessing. The changes represent a significant reduction in noise and surface deviation, which means increased dataset reliability.

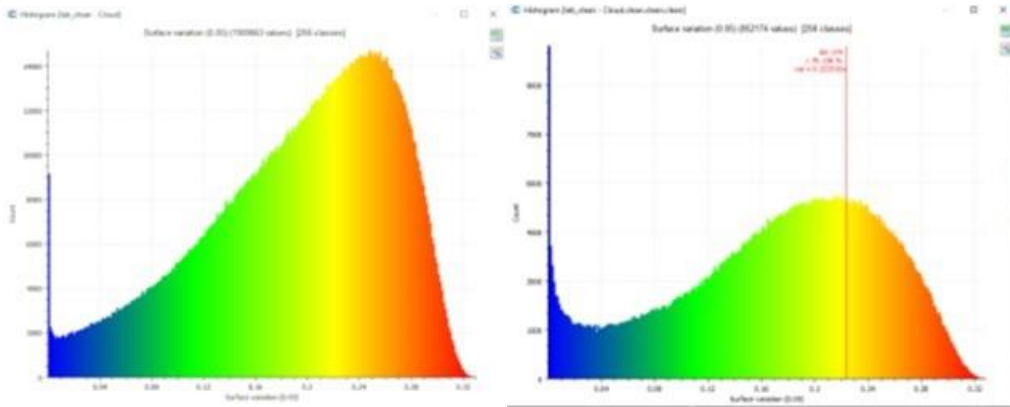


Figure 105. Surface variation histogram a point cloud before (left) and after (right) preprocessing.

Advanced machine learning and computer vision concepts have also been explored to advance the current processing and analysis point cloud framework, involving scene classification, segmentation, object detection, and automatic registration. Traditional ICP requires a priori manually rough registration by picking and aligning equivalent key points in comparing clouds, a very time-consuming procedure in aligning large sets. However, automatic geometric extraction, keypoint detector, and matching using machine learning are promising techniques for automating point cloud registration efficiently.

Virtual Reality Integration

The VR headset system shown in Figure 106 has been used not only for immersive digital twin visualization but will also provide user interaction with our mobile mapping platforms.



Figure 106. FIU's Robotics Laboratory VR headset system.

Figure 107 shows a preliminary VR test, where the DOE Fellow explores her cubicle using the headset's controllers. The Fellow was able to experience stepping in the point cloud dataset and interacting with the cubicle's virtual environment.



Figure 107. Preliminary virtual reality immersion tests.

Digital twin technology involves interpreting large amounts of data to provide insights within DOE facilities or repositories. The capability to visualize the data is equally as important. A combination of digital twins, VR, and AR gives scientists and site engineers the ability to immerse themselves and fully understand the environment, providing the ability to plan and predict, spotting areas of concern before any human [6].

Subtask 18.4.1: Conclusions

The efforts will continue the radiation mapping framework development and digital twin capture and reconstruction, improved by rigorous in-house deployments using our customized ground and aerial mobile platforms. The improvements will include:

- a) integrating additional sensory relevant to surveillance of tank farms,
- b) incorporating Machine Learning into the framework,
- c) automating digital twin tasks such as segmentation, object detection, and automatic registration,
- d) including more sophisticated models to our virtual radiation sensing framework,
- e) implementing information-driven planning and control techniques and comparing their performance with traditional ones, and
- f) fusing close-range data captured by 3D cameras with mid-range ones imaged by LiDAR, combining local accuracy with far-field awareness.

Instructions from the Multi-Agency Radiation Survey and Site Investigation Manual (MARSSIM) will be incorporated in our autonomous mapping algorithms to provide detailed guidance for planning, implementing, and evaluating environmental and radiological facility surveys conducted to demonstrate compliance with a dose-based or risk-based regulation

During the summer, an improved agnostic field-deployable sensor package will be deployed at Hanford's mobile platforms. Lessons learned during the team summer internships, deploying our sensors and algorithm in the Hanford tank farm, and interacting with scientists and engineers are crucial for further improving FIU's autonomous mapping framework, considering actual site challenges and conditions.

Subtask 18.4.1: References

1. DOE (2018, November). Post-Retrieval Activities Changing Hanford Tank Farm Footprint. <https://www.energy.gov/em/articles/post-retrieval-activities-changing-hanford-tank-farm-footprint>
2. S. Ferrari and T. A. Wettergren. (2021). Information-Driven Planning and Control. The MIT Press.
3. C. E. Rasmussen and C. K. I. Williams (2005). Gaussian Processes for Machine Learning. The MIT Press.
4. M. Popovic, T. Vidal-Calleja, J. J. Chung, J. Nieto, and R. Siegwart. (2020). Informative Path Planning for Active Field Mapping under Localization Uncertainty, IEEE International Conference on Robotics and Automation
5. C. Miskinis (2018, January). Combining digital twin simulations with virtual reality – what can we expect?. <https://www.challenge.org/insights/virtual-reality-and-digital-twin>
6. M. Berger, A. Tagliasacchi, L. Seversky, P. Alliez, G. Guennebaud, J. Levine, A. Sharf, C. Silva (2016). A Survey of Surface Reconstruction from Point Clouds. Computer Graphics Forum.

TASK 19: PIPELINE INTEGRITY AND ANALYSIS

Subtask 19.1: Pipeline Corrosion and Erosion Evaluation

Subtask 19.1: Introduction

The Hanford Site Tank Farm has implemented a Fitness-for-Service (FFS) program for the Waste Transfer System. The FFS program, based on API-579-1/ASME FFS-1, examines structural parameters of the waste transfer systems in order to develop erosion/corrosion rates for relevant system components. The FFS information is acquired from opportunistic evaluations of pipelines that have been removed from service. FIU-ARC engineers work closely with key Hanford high level waste (HLW) personnel and the contractor, Washington River Protection Solutions, LLC (WRPS), to support the FFS program, deliver solutions for sensor evaluations, conduct bench-scale testing followed by data acquisition and analysis for corrosion and erosion assessment. Previous efforts at Hanford included the installation of sensors on a number of the POR 104 components, to provide real time pipe wall thickness measurements. Due to various limitations, alternative approaches for remote permanently mounted pipe wall ultrasonic thickness measurement systems are being investigated.

FIU's efforts to support this scope have included investigating key options available in the market for remote, permanently mounted ultrasonic transducer (UT) and other sensor systems for HLW pipe wall thickness measurements and wear. Specific applications include straight sections, elbows and other fittings used in jumper pits, evaporators, and valve boxes. FIU assessed the use of various ultrasonic systems that are either commercially available or used previously at Hanford and selected the most promising systems for further evaluation. One of the two down selected systems (Permasense UT sensor system) was acquired, and initial bench-scale validation testing was conducted. Following the initial bench scale tests, engineering scale testing was implemented on an in-house designed and installed test loop. The design loop has been established using 2- and 3-inch diameter straight and bend pipe sections to mount the sensors. The loop was eroded using sand-water slurry and the Permasense sensors were used for thickness measurements [1,2,3,4]. The sensors were also tested for their performance in extreme environmental conditions under high humidity and temperatures. Finally, the feasibility of conducting radiation testing on the sensors was considered and a test plan was developed for implementation. In addition to the Permasense UT sensors, two other systems were evaluated for erosion, corrosion and anomaly detection in the pipe loop at FIU. These included the SRNL coupons with the Pencil UT sensor and the Fiber optic sensors from CEL [4,5,6].

FIU has successfully completed the sand water erosion tests on both carbon and stainless-steel coupons. Currently, FIU is investigating the effect of caustic simulants on the SRNL coupons. A bench scale mockup has been constructed and static coupon immersion tests are being conducted. Benefits of this research include providing validation for new methods and technologies that will assist engineers in understanding the fault potential of HLW nuclear waste transfer components due to corrosion and erosion. By providing insights into determining if and when lines need to be removed/replaced, the unneeded excavation of transfer lines can be avoided saving valuable time and resources. Also, more detailed and accurate guidelines can be developed governing the life expectancy of the transfer system and its components. By being able to have accurate predictions

of points of failure from erosion, and by being able to monitor an entire pipeline's status in real-time, resources can be targeted to tackle preventative measures instead of reactive.

Subtask 19.1: Objectives

The motivation for this task is to assist DOE and WRPS in providing realistic estimates of the remaining useful life of the components and to incorporate those estimates into future design plans. This task includes the investigation of various sensor systems and fluid flow dynamics to detect thinning in pipes and tanks along with real-time evolution of the wear using SRNL's mass loss/erosion coupons. Hence, there are three objectives for this task for structural health monitoring using various types of sensors. Including:

- Evaluation of SRNL's stainless steel coupons for erosion testing.
- Design and development of a custom bench scale flow loop for caustic simulant testing.

Subtask 19.1.1: Evaluation of SRNL Stainless Steel Coupons for Erosion Testing

Subtask 19.1.1: Methodology

The purpose of this research was to test and demonstrate that the SRNL erosion and mass loss coupons could provide an in-situ method for collecting erosion and mass loss rates from a pipeline using the stainless steel and carbon steel coupons, during operation. Previous work included initial testing with the first set of carbon steel coupons provided by SRNL to FIU [4]. The application of these coupons was experimentally tested in a bench scale pipe loop by circulating sand-water slurries of varying densities and grit sizes. The intended advantage of the replaceable coupons is their ability to easily calculate mass loss/gain and to gain insights into qualitative data such as erosion patterns on the inside of the pipes.

Collaboration with SRNL scientists during the previous years led to the initial testing of SRNL coupons for erosion in pipe sections. The process included use of small coupons of steel (Figure 108a) made of the same material as used in pipelines across DOE nuclear waste sites. The intention was to measure the changes in thickness using UT sensors and to measure the mass loss on a minute level to detect and quantify pipeline wear. By measuring the minute erosion of the coupon, the life expectancy of sections of pipelines in the field may be calculated. The coupon is inserted into a coupling welded to the pipe surface and the head of the coupon is made flush with the inside of the pipe. By being subjected to the same abrasive forces as the pipe walls, the coupon represents a fully observable model of the pipe section. The advantage of the coupon is that it is easily removable. Mass measurements of the coupon before and after testing were taken to provide insights into the degradation of that particular pipeline, or a pipeline made of similar material. To simulate the effects of waste on degradation of a pipeline system, a bench scale pipe loop was constructed of commonly used geometries found in DOE nuclear waste facilities – 50.8mm (2 inch) and 76.2mm (3 inch) carbon steel pipes, elbows, and reducers (Figure 108b).

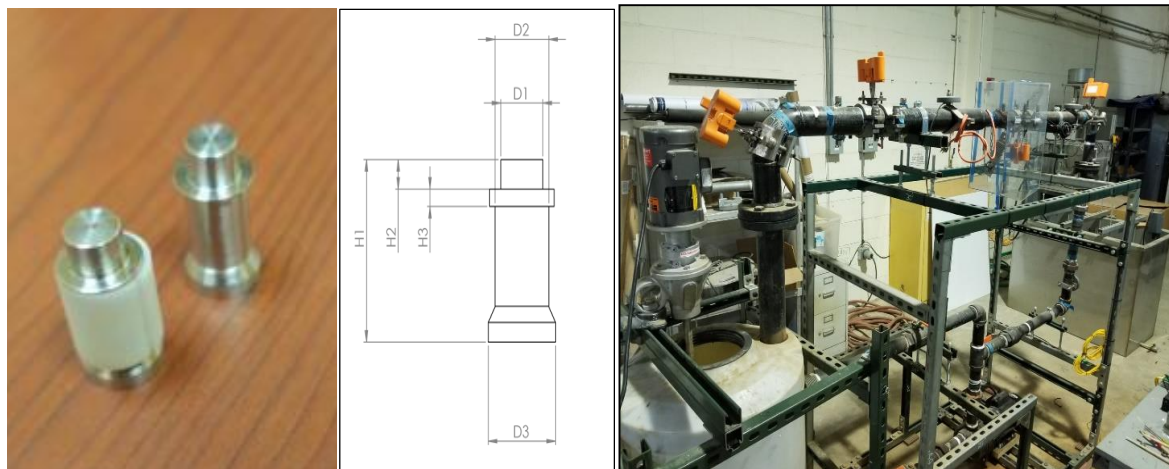


Figure 108. a) SRNL coupon b) dimensions and c) experimental pipe loop.

To quantify the erosion taking place in the pipe, the coupons were weighed and measured using a balance and caliper before being inserted. The surface of the coupon head was also viewed under a microscope and photographed for later comparison after erosion had occurred. During the test, measurements were taken in situ using an Olympus V260-SM UT pencil sensor [5] that was modified to fit specifically in the provided channel within the coupon. Thickness measurements were collected every 30 minutes from both a handheld UT pencil sensor and the permanently mounted UT sensors on the loop. After testing, the coupons were removed from the pipe loop and measurements were taken again in order to quantify mass and height loss, and validate the measurements taken by the pencil sensor. The coupons were tested on the pipe loop with varying sand and water slurry mixtures and grit sizes. Upon completion of the carbon steel coupon testing, this year the next phase of testing has been initiated with stainless steel coupons to evaluate the erosion effects on the stainless-steel material. The pipe loop was thoroughly cleaned by circulating water and the SRNL coupons were inserted. The new coupons were tested using sand and water mixtures. The pipe loop at FIU has been updated with changes to the pump and installation of the coupons. During the process, the coupons were unable to flush with the inner surface of the pipe loop. Hence, the coupons were machined to have a tight fit in the pipe sections for appropriate testing. The borescope images of the coupons in the pipe are shown in Figure 109.



Figure 109. Borecope images of the coupons in the pipe loop.

Subtask 19.1.1: Results and Discussion

Erosion testing was conducted by circulating sand and water mixture with 5-10% volume fraction of sand. The SRNL coupons were placed at the 3-inch elbow and 3-inch straight section (one at the bottom and the other at the top). In the first set of experiments, the other 2 coupon holes were blocked using pipe plugs. During the process, a pencil UT sensor is used to detect the change in thickness. Calibration of the UT sensor and measurement during the testing are as shown in Figure 110.



Figure 110. a) UT sensor calibration and b) real-time coupon thickness measurement.

The next steps included weighing the coupons using a Mettler Toledo scale with an accuracy of 5 decimal places in grams. The weighing process has been described previously and the weights of the three coupons before and after testing are provided in Table 5. It is evident from the table that the coupon at the bottom had the maximum mass loss as expected due to the mass erosion caused by the coarse sand and water at high velocities.

Table 5. Erosion Test results for SRNL Coupons

Coupon Number	Initial Weight (gm) (with sleeve)	Initial Weight (gm) (without sleeve)	Weight (After erosion) (gm) (without sleeve)	Weight loss (gm)
1 (elbow)	8.12616	7.35128	7.34924	0.002
2 (top)	8.30051	7.35125	7.34921	0.002
3 (bottom)	8.26943	7.36321	7.35998	0.003

Erosion of the coupon surfaces and sides for the elbow and the bottom coupons are as shown in Figure 111. The surface erosion was observed to be maximum at the elbow face followed by the bottom face. From the tests, it was concluded that the stainless-steel coupons are not eroded as much as the previous mild steel coupons [4]. Further testing was needed to investigate the erosion characteristics of the stainless-steel coupons.



Figure 111. Eroded Coupon surfaces removed from the elbow and bottom sections of the pipe.

The next set of experiments was conducted with simultaneous use of carbon and stainless-steel coupons to compare and contrast the material erosion effects under the same simulant flow conditions. Several 7-8 hr tests were conducted with 2 SS and 2 CS coupons placed on the top and bottom of the 3-inch pipe section. Visual images were captured before and after the erosion tests. Based on the tests, carbon steel coupons showed a large amount of surface erosion. Sample test results obtained are shown in Table 6 (columns 3 and 4). The top coupon showed erosion and corrosion on the surface contacting the simulant and the periphery around it, while the bottom coupon showed erosion and corrosion both on the top surface and the inner step surface. The phenomena can be attributed to the fluid penetrating into the hole and seeping to the step surface due to gravity. Additionally, the top surface depicted an even and deeper erosion pattern when compared to the bottom coupon with more scarring and uneven erosion corrosion. Hence, the location of coupon placement affected erosion in varied surface images.

Table 6. SRNL Coupon Test Results (Images)

	Pre-test Image	Post-test Image	High Resolution Surface Image (post-test)
Carbon Steel (Bottom)			



Coupon weights and heights were also measured under pre- and post-test conditions. Test results are listed in Table 7 and Table 8 for the pre- and post-testing respectively. Geometric dimensions for the coupon are shown in Figure 108. The parameters of importance are H1, H2 and D1. Considering the coupon heights, it is observed that there was no significant change in the SS coupons as expected, while the CS coupons reduced in height explaining the surface erosion. It is evident from the tables that all the coupons show mass gain except for one of the stainless-steel coupons. Hence, the mass gain in this case can be explained as particle agglomeration and corrosion effects. Also, it was noticed that the other geometric dimensions (diameters D2 and D3, height H3) did not change indicating intact fit of the coupon in the pipe hole.

Table 7. Coupon Geometry and Weight Conditions (Pre-Test)

Coupon	Carbon Steel (top)	Carbon Steel (bottom)	Stainless Steel (top)	Stainless Steel (bottom)
Weight (gm)	6.921	8.171	7.377	7.1886
Height (H1)* (inch)	25.273	25.819	24.689	25.210
Height (H2)* (inch)	6.718	5.486	5.525	5.779

* Refer Fig. 1a

Table 8. Coupon Geometry and Weight Conditions (Post-Test)

Coupon	Carbon Steel (top)	Carbon Steel (bottom)	Stainless Steel (top)	Stainless Steel (bottom)
Weight (gm)	6.933	8.175	7.3480	7.2046
Height (H1)* (inch)	25.248	25.794	24.689	25.210
Height (H2)* (inch)	6.693	5.461	5.525	5.779

* Refer Fig. 1a.

Ultrasonic thickness measurements were also taken in real-time (30-minute intervals) during the tests. A typical 7-8 hr test indicated an average erosion rate of 0.01 mm in thickness for carbon steel coupons in about 4 hrs, depending on a mixture of coarse and medium sands. It was noticed that for short duration tests, some tests indicated thickness increases while some others indicated not much effect on the overall thickness. This could be due to the sand starting to settle in the pipes (bottom) over time (approx. 3-4 hrs) and fewer particles floating at the top (lower density). The change in thickness values over 6 experiments are analyzed next. The test matrix for conducting the tests is given in Table 9.

Table 9. Test Matrix for the Engineering Scale Coupon Testing

Test	Coupons	Fine Sand (40F) (gallons)	Medium Sand (30/65) (gallons)	Coarse Sand (20/30) (gallons)	Very Coarse Sand (6/20) (gallons)
Test 1	3 SS	1	0	0	3
Test 2	3 SS	2	0	2	2
Test 3	3 SS	0	0	6	2
Test 4	3 SS	4	0	2	2
Test 5	2 SS and 2 CS	0	3.6	2.4	0
Test 6	2 SS and 2 CS	0	2	4	0

* SS – Stainless Steel and CS – Carbon Steel.

In Test 1, a mixture of very fine and very coarse sand with a ratio of 1 to 3 respectively, totaling 4 gallons was used to generate the simulated abrasive waste mixture. Results (Figure 112) show some change in thickness early in testing with the elbow coupon and change in the bottom coupon after 4 hours of test. The top coupon recorded no change over the duration of this test. In Test 2, a mixture of fine, coarse, and very coarse sand in equal parts with a total of 6 gallons was analyzed. Results of this test (Figure 112) showed some gradual change in thickness with both the elbow and top coupons, a slight variation in the measurements of the bottom coupon likely due to deposition of sand particles. Also, it is to be noted that the initial coupon thicknesses differ in the graphs, as they were chamfered for precise fit in the pipe holes.

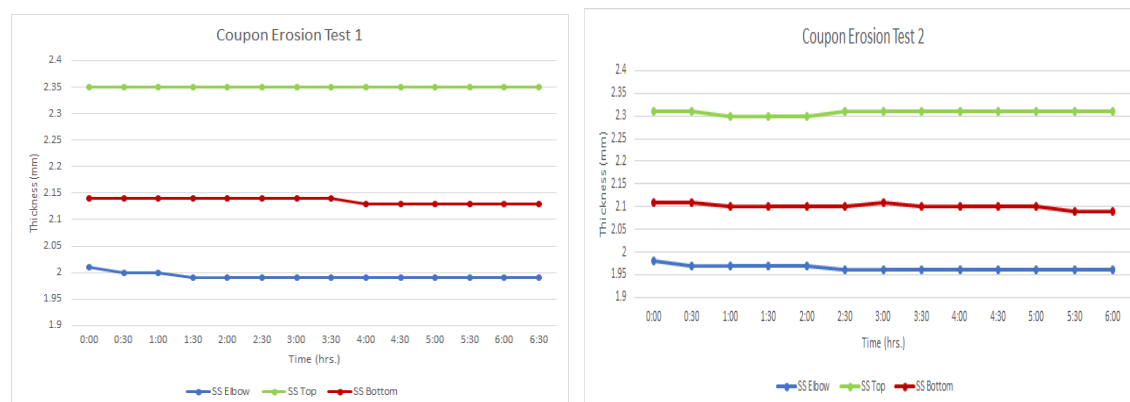


Figure 112. Results of Coupon Erosion Test 1 and Test 2.

In Test 3, a mixture of coarse and very coarse sand with a ratio of 6 to 2 respectively, totaling 8 gallons was used. Results (Figure 113) of this test show an increase in thickness on both the elbow and top coupon which can only be explained by sand particle deposition in these areas. The coupon in the bottom position recorded no change. In test 4 a mixture of fine, coarse, and very coarse sand with 4, 2, and 2 respectively, totaling 8 gallons was analyzed. Results of this test (Figure 113) show no change in thickness throughout. This mixture was ineffective and seems to settle in the pipes and tank quickly, not allowing for any erosion to take place.

Results from erosion Tests 1-4 can be compared based on the number of coupons and their respective positions. The sand grit was altered to see how results varied. Comparing Tests 1-4, it can be observed that the most erosion occurs in Test 2 with a mixture of equal parts of fine, coarse, and very coarse sand, totaling 6 gallons. Results of Tests 1, 3, and 4 do not provide any sort of consistency with thickness change. Following these 4 tests, it has also been determined that the

very coarse sand (6/20 grit) erodes the carbon steel piping at a considerable rate. Due to that effect, future tests will discontinue the use of this particular grit size.

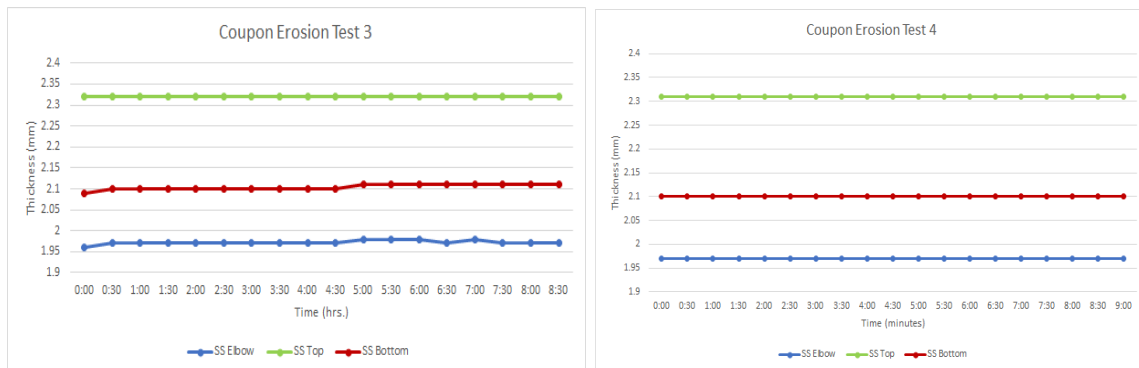


Figure 113. Results of Coupon Erosion Test 3 and Test 4.

In Test 5, a mixture of medium and coarse sand with a ratio of 60/40 respectively, totaling 6 gallons was analyzed. Results (Figure 114) show some thickness change for the carbon steel top coupon at a constant rate. However little to no erosion occurs in the other positions and evidence of disposition of particles can be noted throughout the test. In Test 6, a mixture of medium and coarse sand with a ratio of 2 to 4 respectively, totaling 6 gallons was analyzed. Results (Figure 114) show little to no evidence of erosion at any of the 4 positions. This mixture does not stay in circulation long enough to effectively erode the coupons. The data does show an increase in thickness throughout the test similar to Test 5 where evidence of disposition is observed.

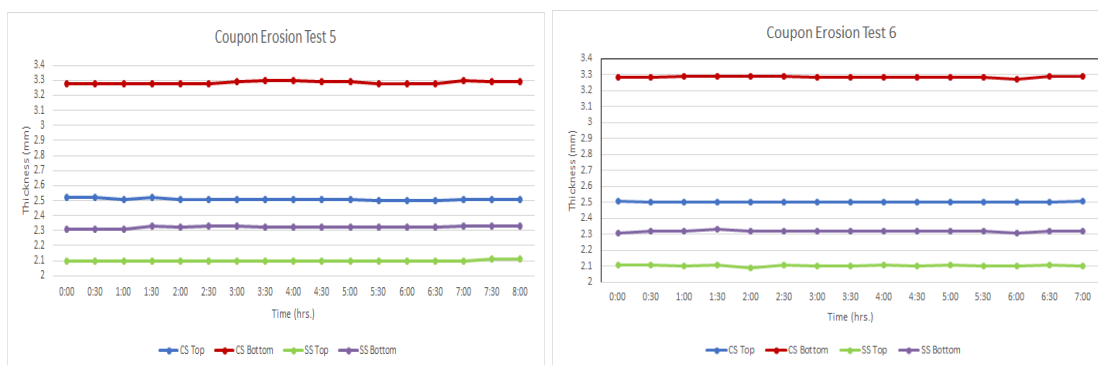


Figure 114. Results of Coupon Erosion Test 5 and Test 6.

Tests 5 and 6 have the same configuration of coupons in regard to material and position. Comparing these two tests, similarities were noticed in the bottom coupons where clear evidence of disposition of sand particles can be seen. In Test 5 promising erosion was observed in the carbon steel coupon over time. From these 2 tests, after excluding the very coarse sand (6/20), the most effective mixture contains a majority of medium sand in combination with coarse sand at a ratio of 60/40.

Subtask 19.1.1: Conclusions

In conclusion, the SRNL coupons have been verified and validated on an engineering scale test bed for their ability to detect pipe wear and erosion on a minute level in real-time. Initial experimental results showed much less change in erosion in stainless steel when compared to the carbon steel coupons. The location of the coupon effected the erosion pattern on the coupon

surface. Additionally, the UT measurements (thickness) showing wear were affected by the sand proportions, grit size and the time of addition of the sand particles in the simulant mixture. In future, the sand testing will be continued for longer durations and addition of DWPF glass frit will be considered for erosion.

Subtask 19.1.1: References

1. Aravelli A., McDaniel, D., Davila, C., “Real-time Erosion-Corrosion Detection in Waste Transfer Pipelines using Guided Wave Ultrasonic Sensors”, Proceedings of the Waste Management Symposia 2018, Phoenix, AZ, March 18-22, 2018.
2. Aravelli, A., Thompson, M., McDaniel, D., Krutsch, M., McNeilly, M., Imrich K., Wiersma B., “Advanced Fiber Optic and Ultrasonic Sensor Systems for Structural Health Monitoring of Pipes in Nuclear Waste Sites”, IMAPS 52nd International Symposium on Microelectronics (IMAPS), Boston, MA, Sep 30-Oct 3, IMAPS (2019).
3. https://srnl.doe.gov/tech_transfer/tech_briefs/SRNL_TechBriefs_UltrasonicThicknessMassLossMeasurement.pdf.
4. Aravelli, A., McDaniel, D., Thompson, M., Imrich, K., Wiersma, B., “Erosion-Corrosion Detection in Carbon Steel Pipe Loops using SRNLs Thickness and Mass Loss Measurement Coupons”, Waste Management 2020 Conference, Phoenix, AZ, March 2020.
5. <https://www.olympus-ims.com/en/shop/item/269-productId.570437480.html>
6. Thompson, M., McDaniel, D., Wiersma, B., Aravelli, A. “Structural Health Monitoring Technologies for Wear and Anomaly Detection in Nuclear Waste Transfer Systems”, Waste Management 2021 Conference, Phoenix, AZ, March 2021.

Subtask 19.1.2: Design and Development of a Bench Scale Flow Loop for Caustic Simulant Testing

Subtask 19.1.2: Methodology

Bench Scale Loop Development

A bench scale flow loop has been developed with a smaller footprint to test the effect of caustic flow in the pipe components. The bench scale chemical test loop has been designed as a closed loop system with simulants circulating between a tank and a pump. The pump was down selected from several pumps (available in the market) to the required flow and size parameters. It is a Dayton 1/3 HP pump with stainless steel impeller and casing suitable for caustic solutions and has a maximum flow rate of 21gpm @ 5 ft of head. The test loop mainly consists of 2- and 3-inch diameter schedule 40 carbon steel straight sections. The elbows are made of stainless steel to reduce the overall weight of the loop. The test section of 3-inch nominal diameter is made modular with 3 inches to 2-inch reducers on both sides. The test section will be used for testing the SRNL coupons (both SS and CS). The loop’s footprint consists of about 5 ft length and 2 ft width with the overall pipe length about 13 ft. It is rested on and clamped to a Unistrut framework. Initially, 6 designs were made, and one was down selected based on the test variables and physical laboratory accommodation. Solidworks software was used to draw the designs. Final loop design and the assembled loop is shown in Figure 115. Modifications to the loop will be made, if any, according to the feedback provided from the SRNL team.

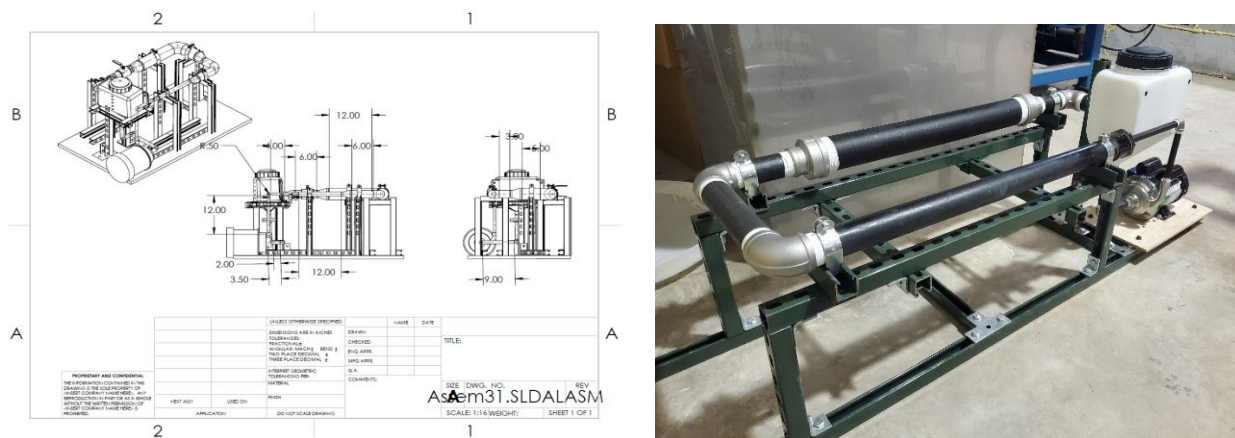


Figure 115. a) Bench scale loop development CAD drawing and b) assembled loop.

Static Immersion Testing of SRNL Coupons (chemical corrosion)

This subtask also included initiation of static testing with SRNL coupons using caustic simulants. A chemical recipe was developed by SRNL scientists and provided to FIU, that requires preparation of 2, 4 and 6 M concentrations of the chemicals – mainly salts of sodium. The subtask was initially designed to conduct the chemical simulant immersion testing of the SRNL coupons under static conditions. Two cases were suggested - complete immersion and partial immersion. Complete immersion samples are to be placed in a beaker with the prepared 2M, 4M or 6M simulant solutions and the new stainless steel and carbon steel coupons immersed in them. The beakers will be covered. In the case of the partial immersion testing, a Petri dish with top removed, is used to pour a certain volume of the prepared simulant. The coupons are then vertically placed for partial dipping to half their height (@ 0.5 inch) in the solution. This process will be useful to distinguish the chemical corrosion characteristics of the coupon’s peripheral surface with and without chemical contact. A proposed initial test matrix with various test options is shown in Table 10.

Table 10. Test Matrix for Salt Simulant Testing of the SRNL Coupons

Salt Simulant (concentration)	2M	4M	6M	2M	4M	6M
Coupon Test Type	Partial Immersion			Complete Immersion		
	Time (months)			Time (months)		
Stainless Steel	6/10	4/8	2/6	6	4	2
Low Carbon Steel	2	1	0.5/4	2	1	0.5

Testing was conducted in 2-3 stages. The first stage included partial and complete immersion, while stages 2 and 3 were complete immersion. For the test, two stainless steel coupons and one carbon steel coupon were initially used for complete immersion testing and partial immersion testing respectively. The caustic solution consisted of a 2M concentration of the mixture of chemicals as suggested by SRNL scientists. The coupons were observed for about 5 weeks. Visual and weight inspections were conducted. Based on the results, tests 2 and 3 were conducted, hence, 6 coupons (CS and SS) were used for static testing. Results are discussed in the next section.

Subtask 19.1.1: Results and Discussion

Leak tests on the developed bench scale loop

Construction of the caustic loop was followed by conducting leak tests (water) on the loop to assess the functionality of the loop at its current configuration. After running the test for approximately 2 hours, a small leak at the bulk-head fitting that joins the steel pipe section to the simulant tank was observed. As this loop will be used to test chemical solutions, it is crucial that all issues are completely resolved before chemical testing is conducted. Potential solutions to the current leak challenge included alternative bulk-head fitting, additional gaskets, sealant, and pipe length adjustments. The test loop, water testing and the pipe leak junction are shown in Figure 116. All required components were procured, and the test loop was repaired, and water leak testing was conducted. Currently, the loop is functional without any leaks. Additional efforts include drilling holes on the 3-inch test section (30 inches long) to house SRNL coupons for testing.



Figure 116. a) Bench scale loop, b) water testing and c) pipe leak.

Static Coupons Test Results

Sample images of the immersion tests are shown in Figure 117. It is evident, based on the color change in the solution, that the carbon steel coupon has corroded more than the stainless-steel coupon as expected. Also, the coupons were removed from the solution for physical inspection and weight changes. Shown in Figure 118 are the inside images. It can be concluded that the CS coupon (brown) underwent maximum corrosion followed by the partially immersed SS coupon and the completely immersed SS coupon. The phenomena can be explained with atmospheric oxidation leading to greater corrosion than the 2M salt solution in the case of SS coupons. Additionally, Table 11 provides the results for weight changes as a measure of oxidation levels. In this case as well, the CS and SS (partial immersion) coupons gained greater weight when compared to the fully immersed SS coupon indicating greater corrosion.



Figure 117. SRNL coupon immersion tests initial (Day 1) (left) and current (Day 35) (right).



Figure 118. Visual corrosion inspection of the CS and SS coupons (2M).

Table 11. Static Immersion Test Results (Test 1)

Coupon	Initial Weight (gm) 05 / 07 /2021	Current Weight (gm) 06/15/2021	Weight Change (gm)	Immersion Level
Stainless Steel #4	9.228	9.256	0.028	Partial
Stainless Steel #10	9.131	9.147	0.016	Full
Carbon Steel	9.652	9.698	0.046	Full

Following initial testing with 2M concentration, 4M and 6M solutions were also prepared, and coupons were immersed in the solution bottles. The caustic simulant static testing continued for about 4 months and test data was collected every 2 weeks. The latest sample set is shown in Table 12. In this period, a new method has been adopted to remove any additional liquid in the sample. A hair drier is utilized for approximately 5 minutes to fully remove the solution from inside the coupons. In addition to the images, mass loss/gain and the pH of the solution is also being measured. This is to detect the corrosion effect in the caustic solution over time. A sample pH set measured is shown in Table 13. Basic solutions have higher pH, hence, the 6M solution is the highest in the table. It is observed that there is an anomaly between 2M and 4M solutions, possibly due to the 2M sample being heavily corroded in carbon steel. This behavior will be closely

monitored in the upcoming months to confirm or deny this relationship. There are clear signs of pitting corrosion found inside of the 6M coupon, indicated by the holes near the bottom. The 2M coupon is an anomaly thus far, since it shows corrosion scale developing inside the carbon steel coupon. For the 6M and 4M carbon steel coupons, mass reduction is an anomaly in this trial, due to the mass loss caused by the salt removal. Mass loss over a longer period (6 weeks) is shown in Figure 119. It is evident, the 6M solution has a higher mass loss over time compared to the 2M solution. This is due to the greater levels of corrosion with higher causticity.

Table 12. Static immersion visual test results of the SRNL coupons.

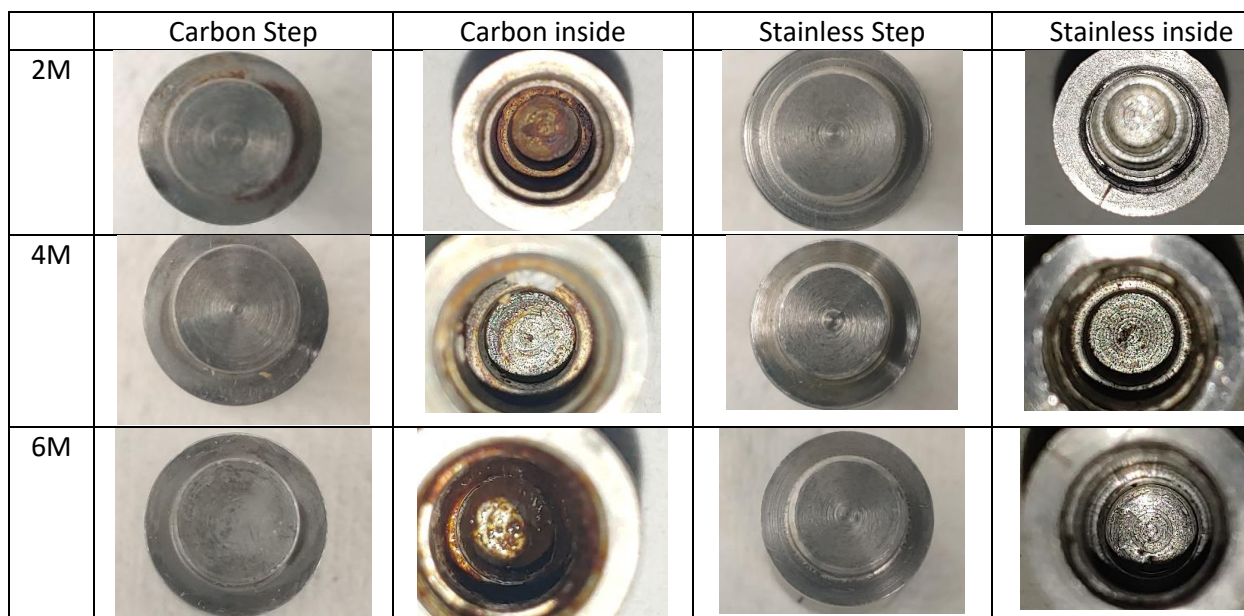


Table 13. pH Variation in 2M, 4M and 6M Solutions

Molarity	Coupon Material	pH
2M	CS	13.19
2M	SS	13.21
4M	CS	13.15
4M	SS	13.08
6M	CS	13.30
6M	SS	13.26

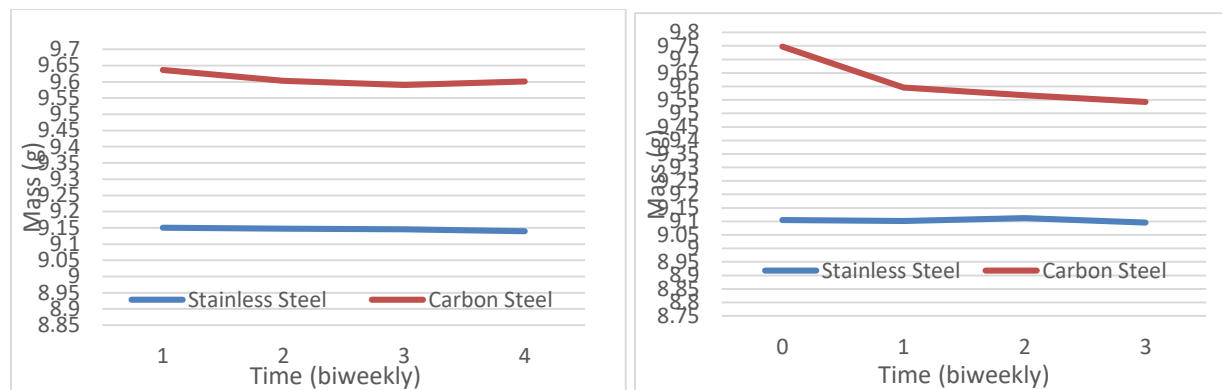


Figure 119. Mass change in 2M and 6M solutions.

Currently, FIU is continuing the static experiments with the coupons and will initiate the dynamic testing using the flow loop in the upcoming year.

Subtask 19.1.2: Conclusions

In conclusion, the erosion and corrosion effects on carbon and stainless pipe material and the SRNL coupons is being investigated under this subtask. The work involves testing the coupon/UT sensor in representative environments anticipated in the transfer lines at SRS. Therefore, SRNL provided recipes for waste simulants that is utilized in the flow loops at FIU. Dr. Thomas Peters has developed three salt solution recipes for consideration. The initial stage included conducting static immersion tests using the 3 recipes (2M, 4M and 6 M concentrated salt solutions). Results indicate chemical corrosion in terms of visual images, mass loss and height/dimensional changes. Additionally, FIU has developed a bench-scale pipe loop for dynamic/real-time testing of the chemical simulant effect on corrosion. The loop has been successfully tested with water for leaks and is ready for the chemical simulants. The next steps involve continuation of the static immersion tests and the dynamic salt simulant testing using the newly built loop under a fume hood.

Subtask 19.1.2: References

1. Wiersma, B. J., Peters, T. B., Poirier, M., “Simulant Recipes for Flow-loop Testing at Florida International University”, SRNL-L3000-2020-00017, December 18, 2020.
2. Aravelli, A., McDaniel, D., Thompson, M., Imrich, K., Wiersma, B., “Erosion-Corrosion Detection in Carbon Steel Pipe Loops using SRNLs Thickness and Mass Loss Measurement Coupons”, Waste Management 2020 Conference, Phoenix, AZ, March 2020.

Subtask 19.2: Evaluation of Nonmetallic Components in the Waste Transfer System

Subtask 19.2: Introduction

Nonmetallic materials are utilized in the waste transfer system at the Hanford tank farms; these include the inner hose of the hose-in-hose transfer lines (HIHTLs), Garlock[®] gaskets and ethylene propylene diene monomer (EPDM) O-rings. These materials are exposed to simultaneous stressors including β and γ radiation, elevated temperatures, caustic supernatant as well as high pressures during normal use. In 2011, the Defense Nuclear Facilities Safety Board recommended to the U.S.

Department of Energy (DOE) to conduct post service examination of HIHTLs to improve the existing technical basis for component service life. Suppliers of the nonmetallic components often provide information regarding the effects of some of the stressors, but limited information is available for simultaneous stressor exposure.

An extensive test plan was developed by Sandia National Laboratories to understand the simultaneous effects of the aforementioned stressors [1]; however, this test plan was never executed. Additional studies conducted by Lieberman provide information on HIHTLs at elevated temperature and pressure, but little information is gained regarding the synergistic effects with the caustic supernatant [2]. Florida International University (FIU) has been tasked with supporting this effort by conducting multi stressor testing on typical nonmetallic materials used at the Hanford tank farms. Previous years' research efforts focused on evaluating the aging behavior of EPDM by exposing samples of HIHTLs as well as EPDM dog-bone shaped specimens to a 25% sodium hydroxide (NaOH) solution at (100°F), operating (130°F) and design temperatures (170°F) for 6 months and 12 months. In addition, HIHTL and the EPDM dog-bone specimens were also exposed to only hot water at 170°F for a duration of one year. After analyzing the data from the previous phase, it became apparent that the synergistic effects of NaOH with high temperature had a significant effect on the degradation of the specimens. After discussing the findings with the site engineers, it was decided to conduct additional aging of HIHTL and EPDM dog-bone specimens at various concentrations of NaOH as well as water only at the elevated temperatures. Four test loops were developed at FIU allowing for the aging of HIHTL as well as dog-bone specimens utilizing 6.25%, 12.5% and 25% NaOH and water only at 170°F for a duration of one year. After aging, the test specimens had their material properties measured and compared to the baseline (unaged) values. The material properties measured included the burst pressure of the HIHTL specimens as well as the tensile strength of the EPDM dog-bones. This report presents the initial results of the material property tests of the specimens that were done at the time this report was compiled.

Subtask 19.2: Objectives

In order to reinforce the findings from the previous phase of testing, HIHTL coupons as well as EPDM material coupons were used to run additional aging experiments. FIU engineers worked with Hanford personnel to develop experimental combinations that involve aging HIHTL and EPDM material coupons for one-year utilizing sodium hydroxide at concentrations of 6.25%, 12.5% and 25% at 170°F as well as water only at 170°F. Comparing the results of this testing with previous data will provide a better understanding of how the elevated temperature and the sodium hydroxide affect the material properties of the components.

Subtask 19.2.: Phase 3 Testing for HIHTL

Subtask 19.2: Methodology

In order to perform this research, four sets of HIHTLs as well EPDM dog-bone specimens were aged in four aging test loops that utilized sodium hydroxide at concentrations of 6.25%, 12.5% and 25% at 170°F as well as water only at 170°F, respectively, as the circulating solution. After aging, the material properties of the specimens were measured and will be compared to the values of the baseline (unaged) specimens.

Burst pressure testing

Figure 120 shows an image of the HIHTL burst pressure test apparatus with the acrylic safety cover removed. The test apparatus consists of a hydraulic pump, pressure gauge, and a pressure transducer with a range of zero to 48 MPa with an accuracy of 0.25% of full-scale output.

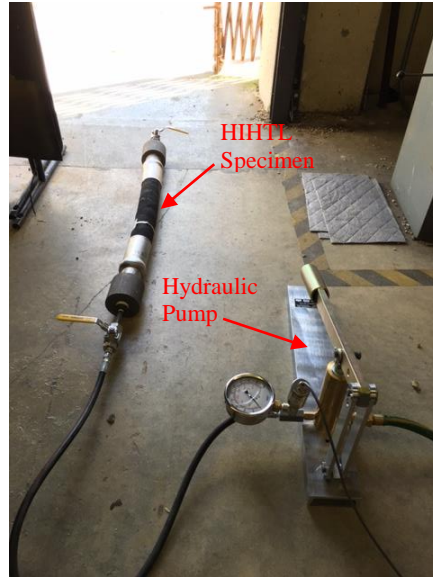


Figure 120. HIHTL burst pressure test apparatus.

Tensile strength testing

Figure 121 shows an image of the tensile strength test apparatus. The tensile strength test apparatus consists of an MTS Criterion™ Model 43 tensile testing machine with a force accuracy of $\pm 0.5\%$ of the applied force.

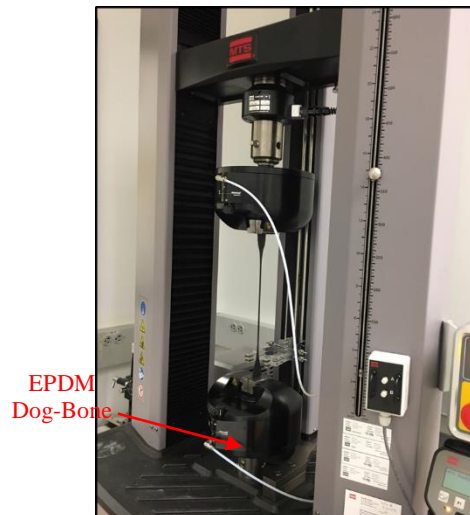


Figure 121. Tensile strength test apparatus.

Subtask 19.2: Results and Discussion

The one-year aging of the test specimens ended on September 21, 2021 and material testing of the specimens started shortly after. For that reason, a limited number of data points were collected at the time this report was compiled. Figure 122 shows the tensile strength test results of the dog-bones aged with a 25% NaOH solution. The results show a variation in the tensile strength of the dog-bones. This is believed to be due to the dog-bone specimens adhering to each other, which results in the two outermost specimens being aged more than the specimens on the inside of the pile. Figure 123 shows the results of the burst pressure testing of the HIHTL specimens. The results show that the burst pressure of the three specimens are very similar to each other.

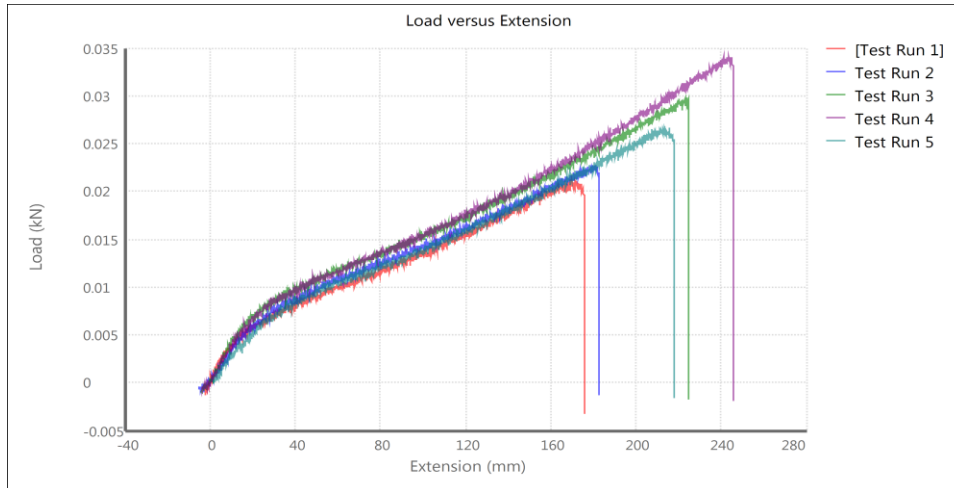


Figure 122. Tensile strength results for dog-bones aged with 25% NaOH.

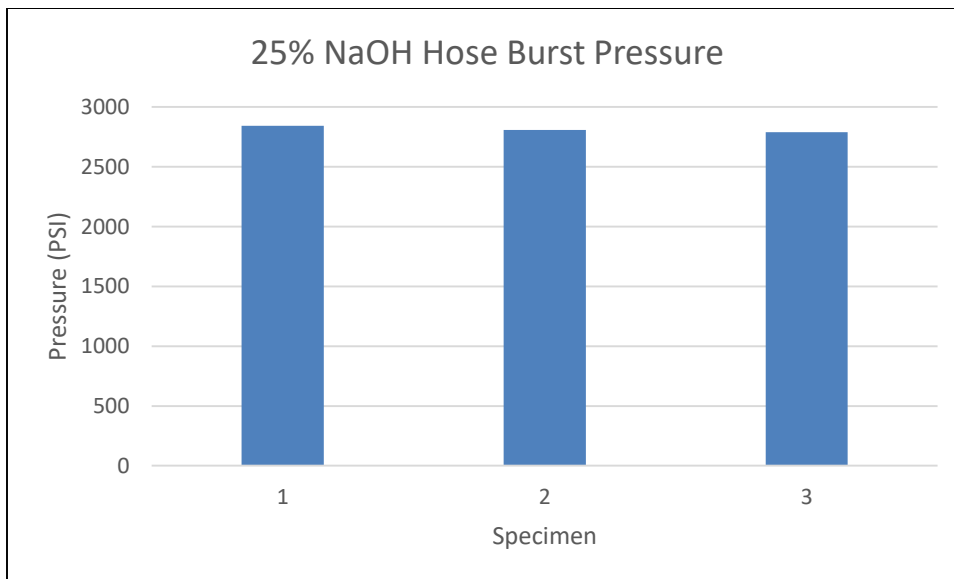


Figure 123. Hose burst pressure for specimens aged with 25% NaOH.

Subtask 19.2: Conclusions

The one-year aging of the HIHTL and EPDM dog-bone specimens has been completed. The testing of HIHTL burst pressure and the tensile strength of the EPDM dog-bones has commenced. Results will be compared to results from the baseline (unaged) specimens.

The next phase of testing will include burst and tensile strength testing of the remaining HIHTL specimens and EPDM dog-bones. In addition, SEM-EDX analysis will be conducted on the HIHTL and EPDM dog-bone specimens.

TASK 20: CORROSION PROTECTION AND CHARACTERIZATION OF EM INFRASTRUCTURE

Subtask 20.1: Evaluation of Coatings for the H-Canyon Exhaust Tunnel

Subtask 20.1: Introduction

The H-Canyon is the only remaining chemical processing facility in America capable of reprocessing plutonium, highly-enriched uranium and other radioactive materials. The H-Canyon Exhaust (HCAEX) Tunnel is used to contain and direct the exhaust air flow from the canyon chemical process areas to the sand filter system, where radioactive contamination is removed. After several structural integrity inspections of the HCAEX tunnel, mandated by mission requirements at the Savannah River Site, there is a great concern about the concrete structure degradation. Videos/pictures taken during inspections evidenced significant degradation of the interior concrete walls characterized by surface erosion exposing concrete coarse aggregates, rebars exposed in some tunnel sections and significant amount of concrete loss, all promoted by the aggressive environment inside the tunnel (primarily nitric acid vapors).

Subtask 20.1: Objectives

The objective of this task is to investigate protective coatings that can be used to mitigate and prevent further degradation of concrete walls exposed to adverse environments in the HCAEX tunnel. Potential coatings will be evaluated and applied on aged concrete surfaces similar to the tunnel degraded walls. Last year, initial immersion-type tests with nitric acid solutions of varying concentrations were performed for aging concrete surfaces. Also, a comprehensive test plan for the development and evaluation of aged concrete surfaces through accelerated aging tests combining the effect of acid concentration, erosion, action mode of the aggressive agents and rebar presence in the concrete, was developed. The execution of the test plan and results analysis were initiated. In line with the objective, the following subtasks will be executed to support the effort:

- Complete the execution of the test plan allowing the development and evaluation of aged concrete surfaces similar to the tunnel walls with protruding aggregates, exposed steel rebar and chemical damage. Based on research findings and lessons learned during the testing, identify the aging conditions of the test plan that reflects the degradation of the HCAEX tunnel and prepare a number of replicates for the evaluation of potential coatings.
- Develop and execute a test plan for the evaluation of potential coatings to protect the degraded tunnel walls. Lessons learned and research findings related to concrete aging will support this subtask. Based on research results, a ranking of the coatings' behavior to accelerated aging conditions will be established that will enable an in-depth selection including aspects such as cost, surface preparation and application methods.

Subtask 20.1.1: Execution of Test Plan for Aging Concrete Surfaces

Subtask 20.1.1: Methodology

Test plan

A comprehensive test plan summarized in Table 14 below was developed for the accelerated aging of concrete surfaces.

Table 14. Test Plan for Accelerated Aging of Concrete

Test number	Acid concentration	Mode*	Erosion	Steel Rebar
1	Low	Std. aging	Erosion	No rebar
2	Low	Std. aging	No erosion	No rebar
3	Low	Enhanced aging	Erosion	No rebar
4	Low	Enhanced aging	No erosion	No rebar
5	High	Std. aging	Erosion	No rebar
6	High	Std. aging	No erosion	No rebar
7	High	Enhanced aging	Erosion	No rebar
8	High	Enhanced aging	No erosion	No rebar
9	High	Std. aging	Erosion	Rebar
10	High	Std. aging	No erosion	Rebar
11	High	Enhanced aging	Erosion	Rebar
12	High	Enhanced aging	No erosion	Rebar

The 4 variables being studied are 1) acid concentration, 2) mode of action of the aggressive agent (enhanced and standard), 3) erosion and 4) presence of steel rebar. The individual and synergistic effect of these variables on the concrete degradation process was evaluated. The various aging conditions of the test plan are not intended to simulate the tunnel conditions but are considered the primary variables affecting the concrete degradation process.

Specimen preparation

Concrete specimens with and without embedded rebar were developed for this study. A concrete mix design believed to be used in the H-Canyon construction was utilized for preparing the specimens. Concrete cylinders without rebar and dimensions of 4 in in diameter and 8 in in height were prepared following ASTM C192/C192M-18 [1]. These specimens were used for compression testing and the generation of smaller specimens of 4 in in diameter and 2 in in height, utilized for concrete aging. Also, small cylinders of 4 in in diameter and 2 in in height, with the rebar placed at 0.5 inch of one cylinder end were developed and used for the aging tests. The cylinder end closest to the embedded rebar was exposed to the aging conditions. At least 6 replicates were used for each aging condition, facilitating a representative sample and the development of different measurements over time. Selected specimens not exposed to the aging conditions were used as control specimens for baseline comparison. Before the aging process, specimens were labelled,

visually inspected, photo documented, dimensions were taken (diameter and height), as well as the weight. All the recorded information was considered as the as-received or initial condition. The concrete samples (except the reference samples) were then exposed to the various aging conditions listed in the test plan.

Accelerated aging conditions

The various accelerated aging conditions being studied are summarized in Table 14. Two modes of the aggressive agents were utilized, enhanced and standard aging. Enhanced aging consisted of the continuous immersion of the specimen’s top surface in the acid solution and was considered the worst-case scenario at the highest acid concentration. Standard aging was based on a cyclic experiment including three consecutive steps: 1) immersion in acid solution, 2) exposure in a humidity/temperature chamber (100°F and 90% relative humidity) and 3) exposure to an erosive environment (selected cases). Two concentrations of the nitric acid solution were considered for the study, 0.5M and 0.025M. The acidic aging was combined with and without the effect of erosion, simulated with a stainless-steel wire brush. The intention of the erosion is to eliminate all removable particles. Figure 124 shows the experimental setup used for the exposure of the specimen to the acid solution. Only one end of the concrete cylinders, the top surface, was exposed to the aging conditions. Experiments with the acid solutions were performed inside the fume hood to reduce the risk of operator exposure to nitric acid fumes.

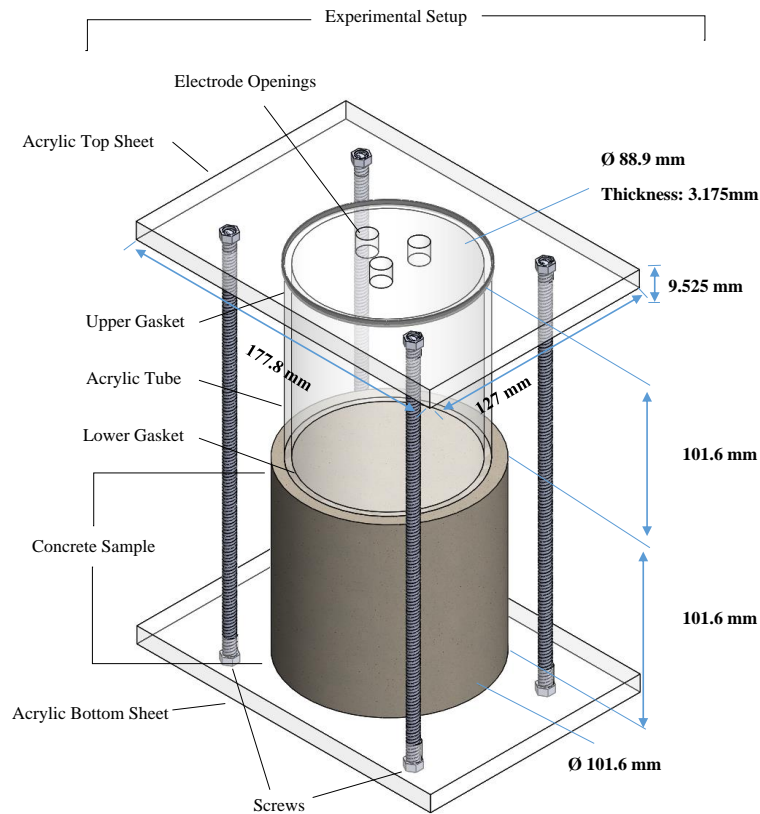


Figure 124. Schematic of test setup for concrete exposure to acid solutions.

Measurements

Several mechanical and durability measurements such as compressive strength, visual inspection, weight, protrusion height of coarse aggregates, pH changes of the acid solution, porosity, water absorption, as well as surface characterization were performed for evaluating the concrete degradation. Visual inspection of the concrete specimens was conducted before, during and after the aging tests and images, the weight and protrusion height were recorded for each time. Mass loss was determined over time using the gravimetric method. Capillary absorption, porosity and density of hardened concrete before aging were determined following the procedure described in ASTM C642-13 [2]. The pH of the acid solutions was measured with time in order to control and keep the concentration constant. Concentrated nitric acid was added when required to keep the concentration of the solution constant.

The chemistry and morphology of the concrete surfaces were characterized by x-ray diffraction (XRD). Samples of matrix material (fine powder), excluding coarse and fine aggregates, were analyzed before and after the aging process. Samples before aging were used as reference for comparative purposes.

Subtask 20.1.1: Results and Discussion

Characterization of reference concrete

Concrete specimens developed in the laboratory were characterized before being exposed to the various aging conditions. Several measurements were performed such as compressive strength, density, water absorption and voids.

Compression test

Crack formations were observed on the concrete surface indicating the end of the compression test. The calculated average compressive strength of the concrete was approximately 25 MPa (3625 psi), slightly higher than the value reported by the Savannah River engineers (17.24 MPa = 2500 psi) for a similar concrete mix. This value is acceptable, considering the composition of the raw materials used for the specimen's preparation is likely different than the material used for preparing the concrete at the H-Canyon 60 years ago.

Density, water absorption and voids (porosity)

The calculated average values of the density, water absorption and voids were 5.58%, 2.31 mg/m³ and 13.36%, respectively. A recent study investigated the positive effect of the addition of nanomaterials on the material's properties such as porosity, water absorption, weight loss and compressive strength. In general, the concrete specimens with nanomaterials showed a decrease of porosity and water absorption, with values less than 7% and 3%, respectively, compared to concrete without nanomaterials [3]. The porosity and water absorption values of the developed concrete specimens are greater (~ 13% and ~6%, respectively) than the former values reported in the literature. These results may lead to a faster degradation of the material after being exposed to aggressive conditions. It is well established that the increase of concrete porosity has a negative effect on the strength and durability.

Enhanced aging: Test 7, Test 8, Test 11, and Test 12

Visual inspection

Figure 125 shows a comparison of images of selected concrete specimens of Test 7, 8, 11 and 12 exposed to 0.5M nitric acid solution and erosion over time.

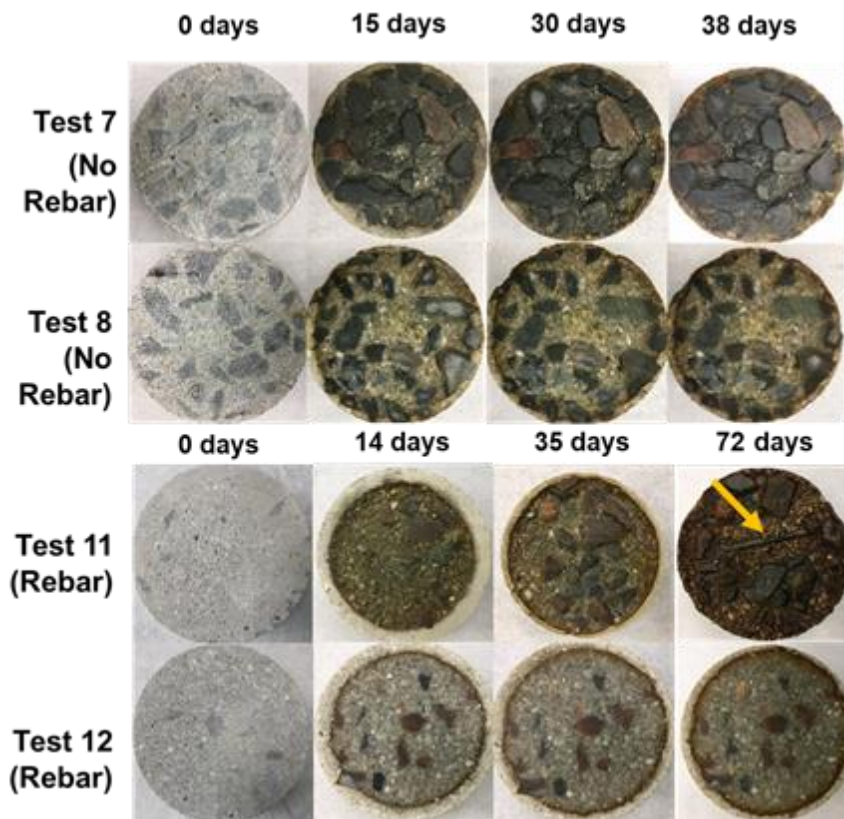


Figure 125. Comparative images of the top view of concrete specimens before and after enhanced aging conditions of Test 7, Test 8, Test 11 and Test 12. The arrow on Test 11 points to the exposed rebar.

Only Test 7 and Test 11 specimens were subjected to erosion with a wire brush. Also, only the replicate 1 of each test is shown in the figure, selected as representative of the tested specimens. The progress of the degradation for all concrete specimens is evident from the figure above. The greatest and fastest degradation was observed on concrete surfaces exposed to the aging conditions of Test 7 and Test 11, due to the synergistic effect of the acid solution and erosion. The degradation was characterized by the loss of material from the matrix, protrusion of the coarse aggregates, as well as exposure of the steel rebar (Test 11). Also, the steel rebar was covered with a film of rust due to the oxidation, changing the color of the concrete surface between brown and reddish. In addition, the action of the steel wire brush on the aged surface exposed to the acid solution accelerated the aging process by eroding the surface and eliminating all removable particles. Test 8 and Test 12 concrete specimens, not exposed to erosion, showed a slight degradation of the surface exposed to the acid solution, but it is not as evident as in specimens of Test 7 and Test 11 (Figure 125). Also, no protrusion of the coarse aggregates was found, although a slight loss of material from the matrix was observed over time.

Concrete specimens developed in the laboratory were characterized before being exposed to the various aging conditions. Several measurements were performed such as compressive strength, density, water absorption and voids.

Weight loss

Weight loss is a quantitative parameter that measures the degradation of the material. As a general trend, the weight loss increased with time for concrete specimens exposed to the enhanced aging conditions of Test 7, Test 8, Test 11 and Test 12. The greatest weight loss was confirmed for those samples exposed to the Test 7 and Test 11 enhanced aging conditions (i.e., 0.5M nitric acid solution and erosion), with average weight losses of 8.5% (77.5 g) and 17.9% (173.8 g) in 38 days and 72 days, respectively. However, specimens submitted to the enhanced aging conditions of Test 8 and Test 12 without erosion, experienced a slower weight loss, up to 2.5% (23.4 g) and 2.2% (21.7 g) of their average weight in 36 and 73 days, respectively. The greater weight loss of concrete specimens of Test 7 and Test 11 is due to the combined effect of the acid solution and erosion, compared to specimens of Test 8 and Test 12 exposed to the single effect of the acid solution. These results agree with the visual inspection findings. Concrete specimens with rebar, Test 11 and Test 12, were exposed to the aging conditions for more time, compared to specimens of Test 7 and Test 8 without rebar, in order to get a degraded concrete surface with the embedded rebar exposed. For this reason, a greater weight loss and number of days were necessary for the concrete specimens of Test 11 and Test 12.

Distance of the protruded aggregates

The distance of the protruded aggregates and rebar exposure is also a quantitative parameter that directly relates to the degradation and durability of the concrete. These two parameters were only tracked on specimens exposed to erosion, i.e., Test 7 and Test 11 concrete specimens. The rest of the samples, Test 8 and Test 12, not exposed to erosion, did not show significant protrusion of the coarse aggregates and consequently the rebar was not exposed. The distance of protruded aggregates for concrete specimens of Test 7 and Test 11 increased with time, with an average value of 0.29 in and 0.33 in after 38 days and 72 days of aging conditions, respectively. The steel rebar was partially exposed in 4 of the 6 replicates after 49 days of enhanced aging and erosion. The steel rebar shows oxidation due to the acid attack, promoting a faster degradation of the sample.

Standard aging: Test 5, Test 6, Test 9 and Test 10

Visual inspection

Figure 126 shows images of selected concrete specimens, exposed to the standard aging conditions of Tests 5, 6, 9 and 10, i.e., exposure to 0.5M nitric acid solution, temperature/humidity and erosion (selected cases). The progress of the concrete aging was characterized by the loss of material from the matrix and protrusion of the coarse aggregates, which was less significant and slower than the enhanced aging cases previously analyzed (Test 7 and Test 11). The brushing of the concrete after each standard aging cycle, promoted the erosion of the surface through the elimination of all removable particles. On the contrary, specimens that were not exposed to erosion, Test 6 and Test 10 specimens, depicted a slower degradation (Figure 126) with almost no protrusion of the coarse aggregates and a slight loss of the concrete matrix with time. This result demonstrates the key role of the erosion in the concrete aging/degradation process. These results agree with the previous

findings of specimens exposed to the “enhanced aging” condition, with and without erosion, Test 7 & Test 11 and Test 8 & Test 12, respectively.

It was observed that concrete specimens with embedded rebar and not exposed to erosion (Test 10) showed formation of superficial cracks. The cracks formed, not found before in other aging conditions, seem to be related to the wetting (acid exposure) and drying (chamber environment) process of the specimens during the aging condition of Test 10. This phenomenon was not observed on concrete specimens without rebar subjected to similar aging conditions.

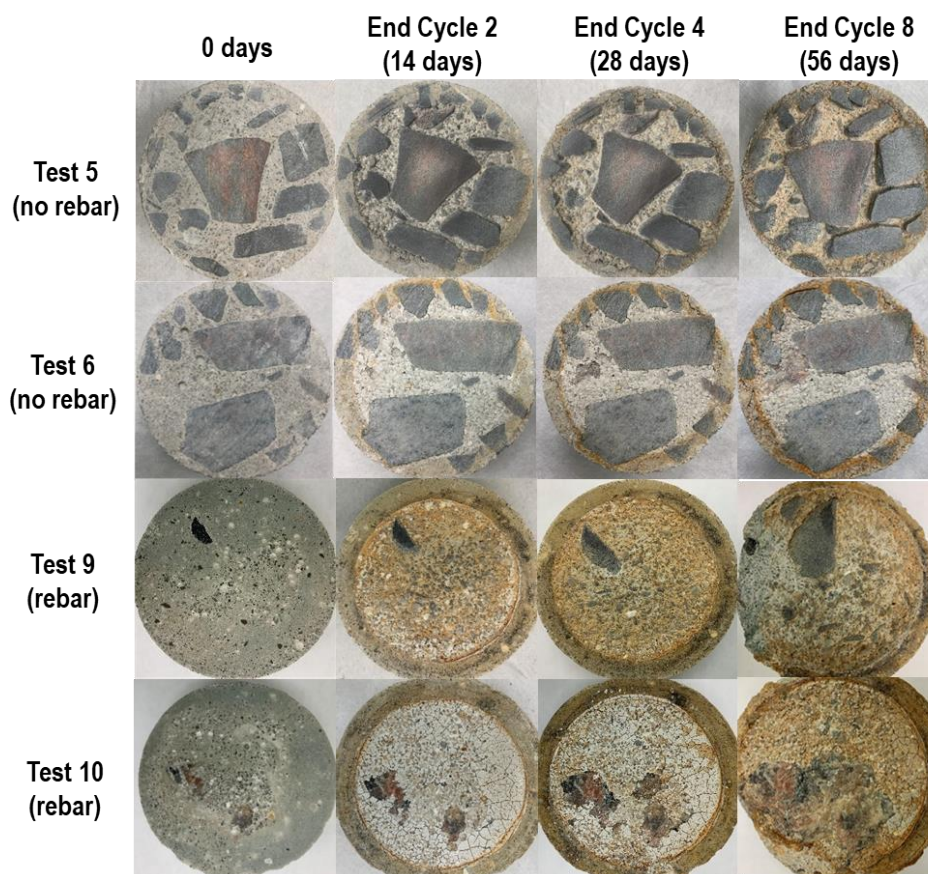


Figure 126. Images of the top view of concrete specimens before and after the end of each standard aging cycle of Test 5, Test 6, Test 9 and Test 10.

Weight loss

As expected, the weight loss increased with time for all the test cases, but the greatest weight loss was confirmed for those samples exposed to the Test 5 and Test 9 standard aging condition and erosion that lost an average of 5.1% (46.0 g) and 6.0% (60.1 g) of their weight in 56 days (8 cycles), respectively. However, specimens submitted to the standard aging conditions of Test 6 and Test 10 without erosion, experienced a slower weight loss, up to 2.7% (24.4 g) and 3.9% (51.0 g) of their average weight in 56 days (8 cycles), respectively.

Distance of the protruded aggregates and steel rebar exposure

The distance of protruded aggregates for concrete specimens of Test 5 and Test 9 increased with time with an average value of 0.3 in, and 0.1 in, respectively, after completing 8 cycles, i.e., 56 days of standard aging and erosion. The degradation observed was not as intense and fast as in the enhanced aging tests cases, Test 7 and Test 11. Concrete specimens of Test 9, exposed to the standard aging and erosion, did not show the steel rebar after 8 aging cycles. For that reason, the experiment was continued until the rebar was exposed, which is the main goal of this research, to develop degrading concrete surfaces with protruded aggregates, exposed rebar, and chemical damage, similar to the tunnel walls. Previous results provide evidence of erosion being the enhanced aging condition that causes the greatest and fastest degradation, Test 7 and Test 11.

Surface characterization by X-ray diffraction

Concrete samples representative of the various aging conditions studied were selected for XRD analysis, including Test 5, standard aging, and Test 7, enhanced aging. For comparative purposes, a concrete specimen not exposed to aging, identified as reference, was also analyzed. Figure 127 shows the XRD spectra of concrete samples before and after aging conditions of Test 5 and Test 7 aging conditions. The XRD spectrum of the reference sample shows a greater amount and more intense peaks including quartz, portlandite and gypsum, compared to aged samples exposed to Test 5 and Test 7 aging conditions. The XRD spectra of the aged samples of Test 5 and Test 7 depict a reduction of portlandite and quartz peaks, which is related to the chemical attack of concrete, leading to the loss of calcium hydroxide (Portlandite) and silicon oxide (Quartz).

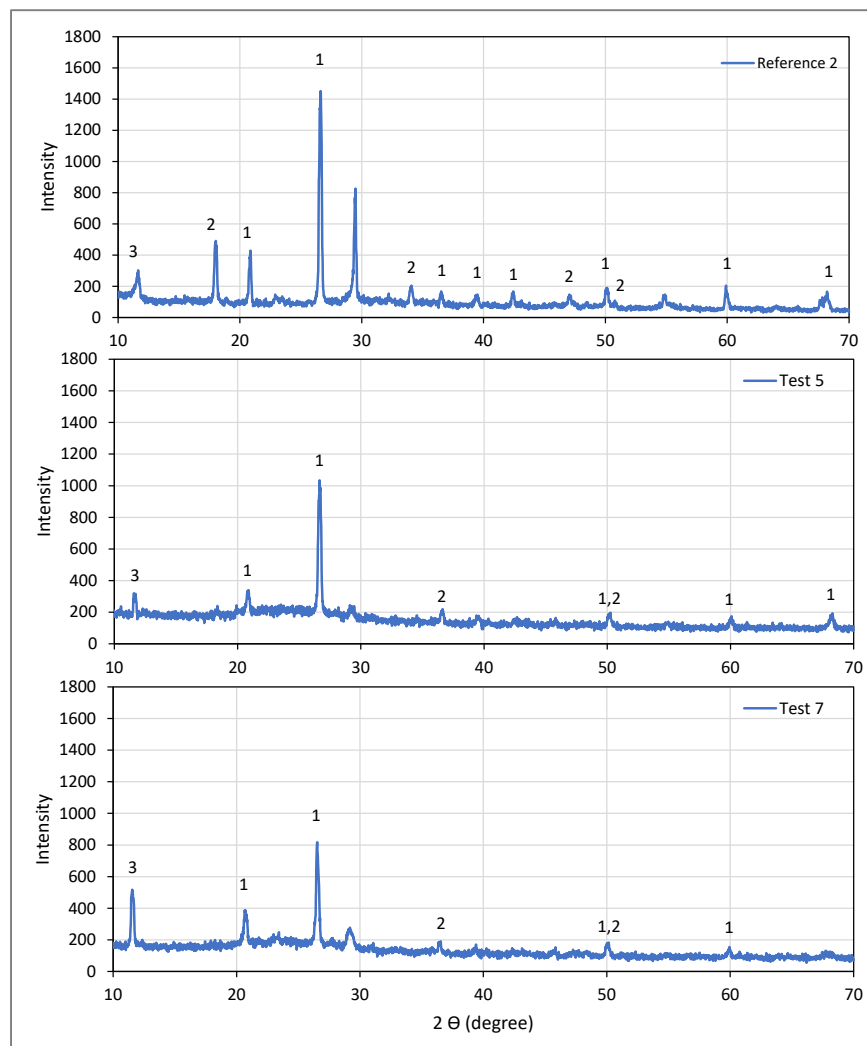


Figure 127. XRD spectra of concrete matrix samples before (reference) and after (Test 5 and Test 7) aging. 1-Silicon oxide (Quartz), SiO_2 , 2-Calcium hydroxide (Portlandite), $\text{Ca}(\text{OH})_2$ and 3-Calcium sulfate hydrate (Gypsum), $\text{CaSO}_4(\text{H}_2\text{O})_2$.

Subtask 20.1.1: Conclusions

Porosity, water absorption and density results of concrete specimens in the as-received conditions showed a more porous and less dense surface, prone to greater water and aggressive agents' entry. Concrete specimens exposed to the enhanced aging condition and erosion, with and without embedded rebar (Test 7 and Test 11), showed the fastest and greatest degradation and constitute the worst-case scenario of all under study. The significant role of the erosion on the concrete degradation process was demonstrated. Durability and surface characterization tests confirmed previous findings.

Subtask 20.1.1: References

1. ASTM C192/C192M-18. Standard Practice for Making and Curing Concrete Test Specimens in the Laboratory. 2018.

2. ASTM C642-13. Standard Test Method for Density, Absorption, and Voids in Hardened Concrete. 2013.
3. Diab, Ahmed et al., "Effect of nanomaterials additives on performance of concrete resistance against magnesium sulfate and acids". Const. Build. Mater. 210 (2019), pp. 210-231.

Subtask 20.1.2: Development and Execution of a Test Plan for Coatings Evaluation

Subtask 20.1.2: Methodology

Test plan

Based on lessons learned and results of the concrete aging process, the enhanced aging condition was selected for the accelerated aging of the coatings. The enhanced aging conditions consists of exposing the surface of the specimen to a 0.5M nitric acid solution. Once a week the surface in contact with the acid solution is exposed to erosion by using a wire brush. This aging procedure combines the chemical and physical effect of the acid solution and the erosion, respectively. Concrete specimens with and without embedded rebar will be used for the bench-scale testing. Table 15 below shows the test plan with the experiments that will be performed for each protection system under study. Protection systems may include coating systems or a combination of repair material and coatings systems. The experiments of the table will be performed for each protection system under study.

Table 15. Test plan for the Accelerating Aging of Coatings

Test number	Surface Preparation	Surface Moisture	Steel Rebar*
1	No preparation	No moisture	No rebar
2	No preparation	No moisture	Rebar
3	No preparation	Moisture	No rebar
4	Preparation	No moisture	No rebar
5	Preparation	Moisture	Rebar
6	Preparation	Moisture	No rebar
7	Preparation	No moisture	Rebar
8	No preparation	Moisture	Rebar

*: Steel rebar exposed on the surface

The 3 variables being studied are 1) surface preparation, 2) surface moisture, and 3) presence of exposed steel rebar on the surface. The individual and synergistic effect of these variables on the performance of the protective properties of the coatings will be investigated. Two levels of each variable were included in the test plan.

Specimen preparation

Aged concrete surfaces developed through the enhanced aging condition and erosion of Test 7 and Test 11, with and without rebar, respectively, will be the substrate for the application of selected coatings. These degraded concrete surfaces have similar composition and morphology of the degraded walls of the HCAEX tunnel. For comparative purposes, non-aged concrete surfaces will be also coated and will be denoted as reference. FIU continued preparing more concrete specimens that will be later aged and used for the evaluation of coatings.

Potential coatings will be applied on aged and non-aged concrete surfaces following the manufacturer requirements. Following the test plan, the aged concrete surfaces will have different surface conditions (e.g., exposed rebar, surface moisture, surface prepared and others) before applying the coating.

Accelerated aging conditions and measurements

Coatings will be exposed to the aggressive conditions of Test 7 and Test 11, “enhanced aging” conditions and erosion, which was the worst-case scenario used for the concrete aging (see section 20.1.1). FIU and Savannah River Site engineers agreed to use the enhanced aging method due to the greatest and fastest degradation of the concrete specimens. The enhanced aging condition combined the exposure of the specimen to a 0.5M nitric acid solution and erosion.

Once a week, the weight and protrusion of the aggregates is measured and annotated. Also, the visual inspection is performed and pictures of different views of the specimen are taken. The erosion is carried out before taking the weight by using a wire brush. The objective is to remove all particles that are not attached to the sample. The pH of the acid solution is measured, at least two times a week. In case the pH has changed, concentrated acid is added based on calculations to adjust to the initial value. The same experimental setup used for aging the top concrete surfaces will be used for aging the selected coatings (Figure 124).

Several durability measurements such as visual inspection, pH changes (acid solution), water adsorption, adhesion, impedance (resistance), surface characterization (SEM-EDS) and others will be used for evaluating the protective properties of the coatings over time. Table 16 summarizes a group of measurements that will be used to evaluate the coating performance.

Table 16. Details of Bench-Scale Testing Measurements

Test	Age	Method
Visual inspection (failures)	Over time	Visual
Coating thickness	Over time	Coating Thickness Gauge
Water absorption	Over time	Electrochemical
Coating protective properties (impedance)	Over time	Electrochemical
pH change (solution)	Over time	pH measures
Adhesion	before/after test	Pull-off test
Surface characterization (SEM-EDS, XRD, IR.)	before/after test	

Coatings

FIU has been working on the preparation of a potential list of coatings that will be evaluated. To that end, several coating companies with experience in the nuclear sector, and with coatings resistant to aggressive environments have been contacted. Three companies have shown interest in the investigation including 1) Sherwin-Williams, 2) Carboline and 3) Belzona. FIU engineers have had email communications and meetings with the companies explaining the aggressive environment of the tunnel, the conditions of the degraded walls, as well as other limitations for the future application using robotic units. With that information, some of the companies have provided the coatings options that they propose to protect the tunnel walls, which will be evaluated in the lab and others are still working on this.

Carboline is coordinating an in-person meeting and product application demonstration with Champion Specialty Services, experts in coatings applications with experience in nuclear facilities and using robotic devices. Carboline proposed a protection system including a resurfacer, which is a cementitious material to repair and level the surface, followed by a coating protective system of three different layers to offer corrosion protection against chemical and hot environments like the tunnel.

FIU also met with representatives from Sherwin Williams and Graco, a coating applicator company with experience in the nuclear sector, to discuss a list of questions FIU prepared. Based on FIU’s inputs, they agreed to send a revised list of coatings with details about the coating, surface preparation requirements and application details. They offered support to prepare the samples.

Subtask 20.1.2: Results and Discussion

The evaluation of the coatings has not started. As soon as FIU prepare enough concrete samples for the coatings application, the coating companies provide the potential list of coatings and prepare the specimens, the accelerated aging of the coatings will start.

Subtask 20.1.2: Conclusions

The test plan for the evaluation of the potential coatings have been prepared. Also, several coating companies have been contacted and a potential list of coatings is under preparation. FIU has prepared and continues to prepare aged and non-aged concrete surfaces that will be used as the substrate to evaluate the coatings.

Subtask 20.2: Corrosion Evaluation of Steel Canisters for Hanford Integrated Disposal Facility

Subtask 20.2: Introduction

A current challenge for DOE and relevant DOE sites is to understand the durability of the steel canisters/containers that will contain low-activity waste (LAW) and secondary waste forms, encapsulated in glass and grout respectively, and that will be placed within the Integrated Disposal Facility (IDF) at Hanford. Currently, corrosion data of the steel and weld regions of the canisters at Hanford that is exposed to groundwater is limited. In addition, there is limited information on groundwater in contact with waste forms. The primary technical need is to study the corrosion rate of the steel canister's exterior that is exposed to Hanford groundwater and determine how well it shields the waste form that is inside the canister from exposure. Additionally, FIU will investigate how the corrosion rate varies in situations where groundwater has also contacted the waste forms.

Subtask 20.2: Objectives

The objective of this subtask is to evaluate material (steel 304, carbon steel, mild steel and weld regions) behavior of the canisters in environments similar to IDF conditions and obtain site-specific corrosion data through electrochemical measurements. Obtaining such data can be used to predict the canister's useful life. The following subtasks will be executed to meet this objective:

- A literature review of the corrosion of the typical canister/container material exposed to groundwater as well as a review of groundwater in contact with encapsulated waste forms. We will identify research gaps by evaluating relevant corrosion studies in this area.
- Development of a test plan to obtain site-specific corrosion data of the canister/container materials exposed to simulated IDF conditions by using electrochemical techniques. The test plan will include the research scope, the experimental design, data collection approaches, and an estimated timeline for the effort.

Subtask 20.2.1: Literature Review for Steel Corrosion Study at Hanford

Subtask 20.2.1: Methodology

FIU initiated this year's efforts by conducting a literature review to identify research gaps and evaluate relevant corrosion studies that support DOE's research efforts to better understand the durability of the steel canisters/containers that will contain low-activity waste (LAW) and secondary waste forms, encapsulated in glass and grout respectively, and that will be placed within the Integrated Disposal Facility (IDF) at Hanford.

Subtask 20.2.1: Results and Discussion

Background

In 1993, Jenkins reported the corrosion behavior of three different alloys, HY-80 steel, 304 SS and Inconel alloy 600, at a burial ground location at Hanford site, Washington [1]. The objective of the investigation was to predict the release rate of nickel into the environment due to the corrosion of these alloys in soils at Hanford. To do this, the corrosion of HY-80 steel, 304 SS and Inconel alloy 600 and other similar materials at other burial sites and in other environments was evaluated. The Hanford location used for the study was identified as Trench 94.

No site-specific corrosion data for the alloys at the Hanford location were available at the beginning of the study. However, a conservative prediction of the corrosion of the alloys in Trench 94 was established through an evaluation of the behavior of the materials in other environments. This comparison was accomplished by using values for sites (for example, Salt Lake City, Utah; Springfield, Ohio; and Los Angeles, California) most similar in corrosivity to Trench 94 and normalizing the data to account for the differences in corrosivity between the test sites and Trench 94. The use of a lower soil resistivity value added an extra measure of conservatism to the predictions [1]. However, no site-specific measurements were made, and soil resistivity was the only measure used. The chemistry of the IDF water will also heavily influence the corrosion behavior of the steels.

The conservative values of the corrosion rate predicted for the HY-80 steel, 304 SS and Inconel alloy 600 in Trench 94 were 70 mg/sq dm/yr, 0.02 mg/sq dm/yr and 0.01 mg/sq dm/yr, respectively. These values were recommended for use in the calculation of the amount of material entering the environment from the alloy in the form of corrosion products. The differences in the predicted values were related to the corrosion resistance of each alloy, the most resistant, being the Inconel alloy 600, followed by the 304 SS and finally the HY-80 steel [1]. Note the very low corrosion rate of stainless steel 304, the material use for construction of the ILAW glass canister.

According to the consulted literature [1-2], there is lack of real site-specific corrosion data of alloys at Hanford site, which constitutes a technical gap in the conservatism built into the IDF PA. Also, there is no site-specific corrosion data at Hanford, where the effect of welds and thermal history of the steel have been investigated. Hence, there is a need for conducting studies and getting site-specific corrosion data of potential canister/container materials having undergone aging cycles of interest. This evaluation will set up the basis of canister/container representation within a PA as a sensitive case to consider the possible prevention of exposure of the waste forms to infiltrating water. This data can also be used for the development of models to predict the canisters/containers durability in shallow subsurface disposal scenarios.

Integrated Disposal Facility

The IDF has been designed to receive immobilized LAW and other low-level waste from the Hanford site Waste Treatment and Immobilization Plant (WTP) and provide permanent and environmentally safe disposition of the waste. This facility is in the 200 East area near WTP. The IDF is an engineered surface barrier, located approximately 85 m above the water table and 12-13 miles away from the Columbia River. Figure 128 shows the IDF features [3].

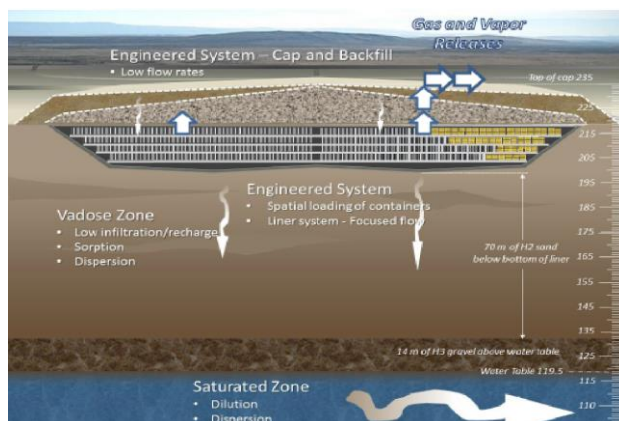


Figure 128. Features of the Integrated Disposal Facility [3].

In case of failure of the IDF surface barrier, the infiltrating water will reach the canisters/containers stored, leading to corrosion problems and failure of the material, although at an unknown rate. Depending on the material of construction and chemistry of the infiltrating water, this corrosion process may be exceedingly slow, isolating the waste forms from the infiltrating groundwater. Following the breach of the canister/container wall, the waste form inside the canister/container will be exposed to the surrounding environment, leading to the dissolution/diffusion processes that control contaminant/radionuclide release [3]. In the IDF PA, it is important to highlight that the corrosion rate of the canister/container material was not considered in the time for the waste form to be exposed to infiltrating water.

The knowledge of the composition and conditions of the infiltrating IDF waters is crucial to gather site-specific data. Regarding the backfill at the IDF, an updated measure of resistivity and composition from actual IDF backfill is expected to be available from the Pacific Northwest National Laboratory lysimeter test in this year [4].

Groundwater/vadose zone pore water characteristics in the IDF

The Hanford site was dedicated to reprocessing of spent nuclear fuel from 1943 to the 1980s. Consequently, process chemicals and radioactively contaminated liquids have been released to the environment and migrated through the vadose zone to the groundwater [5]. The vadose zone, consisting of a porous material and rocks, extends from the surface of the soil to the water table (limit between the vadose zone and the groundwater). The vadose zone has low water content relative to the saturated zone below the water table, where the groundwater is. Because the IDF is a shallow disposal facility, it is in the vadose zone. The remediation of the site, including the contaminant plumes, has been a top priority of Hanford since 1989. Groundwater remediation activities are ongoing and vadose zone characterization and monitoring results have been reported over the years [4].

Serne et al. (2016) developed a recipe to prepare Hanford IDF vadose zone pore water (VZP) for leaching tests. The VZP recipe is in Table 17. The values were obtained through several measurements of VZP collected from Hanford sediments, from boreholes in the 200 E area [5].

Table 17. Vadose Zone Pore Water Simulant [5]

Order to Dissolve	M	Reagents Available	MW	g/L	g for 150 L	g for 600 L	g for 900 L
1	0.012	CaSO ₄ •2H ₂ O	172.1723	2.0661	309.910	1239.641	1859.461
2	0.0017	NaCl	58.4430	0.0994	14.903	59.612	89.418
3	0.0004	NaHCO ₃	84.0068	0.0336	5.040	20.162	30.242
4	0.0034	NaNO ₃	84.9948	0.2890	43.347	173.389	260.084
5	0.0026	MgSO ₄	120.3660	0.3130	46.943	187.771	281.656
6	0.0024	MgCl ₂ •6H ₂ O	203.3034	0.4879	73.189	292.757	439.135
7	0.0007	KCl	74.5515	0.0522	7.828	31.312	46.967
Adjust pH to 7.0 to 7.2 with sodium hydroxide or sulfuric acid.							

The previous recipe will be used to simulate the Hanford IDF groundwater for bench-scale testing of various steel in this environment. This simulant will be informed based on new data collected in the PNNL lysimeter tests. This simulant is the current approximation of the infiltrating water that would reach the container/canister if the IDF surface barrier fails.

Localized Corrosion: Types and Mechanisms

The most damaging and prevalent type of corrosive attack that is most likely to breach the container walls is localized corrosion [6]. The main forms of this kind of attack of importance to nuclear waste problems are pitting, crevice corrosion, stress corrosion cracking and intergranular corrosion. The metals contain defects such as dislocations, voids, stressed areas of the material, and others, each of these factors having influence on the electrochemical properties and possibly leading to localized corrosion phenomena [6].

Pitting corrosion

One form of localized corrosion by which cavities, or holes, are produced in the material is known as pitting corrosion. Pitting is more dangerous than uniform corrosion damage because it is more difficult to detect and predict. Corrosion products often cover the pits. A small, narrow pit with minimal overall metal loss can lead to the failure of an entire engineering system. Pitting is almost a common denominator of all types of localized corrosion attack [7].

Pitting corrosion occurs when discrete areas of a material undergo rapid attack while most of the adjacent surface remains virtually unaffected. Such localization of the anodic and cathodic corrosion processes is characterized by the surface area ratio (S_a/S_c) for these two processes, where S_a and S_c are the areas supporting, respectively, the anodic and cathodic reactions. [7]. Passive metals exhibit a low corrosion rate in aqueous environments due to the formation of a thin passivating oxide film on their surface. Pitting corrosion arises when passivity is lost at localized points on the metal surface, resulting in accelerated dissolution of the underlying metal [7].

Corrosive microenvironments, which tend to be very different from the bulk environment, often play a role in the initiation and propagation of corrosion pits [8]. For a pit to undergo sustained growth, the pit surface must be kept in the active state and prevented from repassivating. The active pit growth requires the maintenance of a local aggressive environment, for example, with chloride ions. Pitting corrosion by the action of active ions, such as chloride ions on passive metals, is the

most frequent case of this type of localized corrosion. It is characterized by a very small anodic area, often imperceptible to the naked eye, with a very large cathodic area (passive area), producing a very intense attack [8].

Crevice corrosion

Another form of localized corrosion is called crevice corrosion, usually related to a stagnant solution on the microenvironmental level. The stagnant microenvironments can be formed in crevices (shielded areas) such as those formed under gaskets, insulation material, surface deposits, disbanded coatings, threads, etc. Another case of possible microenvironment, where crevice corrosion could occur, is welded regions of the canister/container material or even just accumulation of corrosion products or contaminants on the metal surface, with possible stagnation of solution and/or electrolyte [7].

The crevice microenvironment restricts the oxygen diffusion creating a differential aeration cell between the crevice (microenvironment) and the external surface (bulk environment). The cathodic oxygen reduction reaction cannot be sustained in the crevice area, giving it an anodic character in the concentration cell. This anodic imbalance can lead to the creation of highly corrosive microenvironmental conditions in the crevice, conducive to further metal dissolution [7]. The formation of an acidic microenvironment, together with a high chloride ion concentration, is depicted in Figure 129.

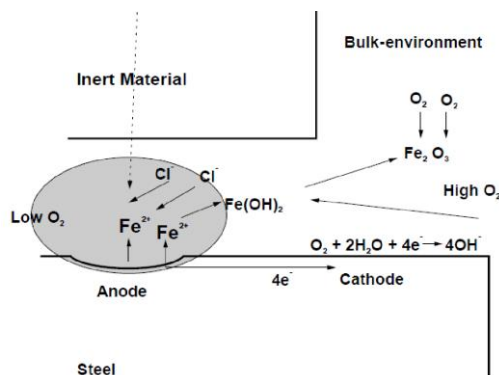


Figure 129. Schematic of the crevice corrosion [7].

Certain alloys such as 304SS and Inconel alloy 600 have reported crevice corrosion signs in microenvironments with insufficient oxygen access. Oxygen is necessary for the stability of the passive films on these alloys, particularly in the presence of chlorides. The local reduction in oxygen access may be caused by a mechanically formed crevice like for example a flange or threaded joint or direct contact with nonporous material such as rock in soil exposure [1]. These and other alloys are planned to be used for the construction of the canister/container and that is why will be investigated through bench-scale testing in a further stage of the project.

Corrosion Cases of Canister/Containers Materials

Case 1: Corrosion of steel canisters contacting encapsulated high-level waste

Localized corrosion was detected at the interfaces between SS and a model nuclear waste glass and between SS and a ceramic waste form. The accelerated corrosion could be related to changes of solution chemistry and local acidity/alkalinity within a confined space (inside of a crevice), which significantly alter the corrosion of both the waste-form materials and the metallic canisters. However, the true impact of this process on the bulk canister or waste form is unknown as this crevice effect is likely to shut down once the surfaces recede from one another. Hence, when different materials are in direct contact in an aqueous environment, their corrosion products may create feedback effects that could further influence their corrosion behaviors. These research findings will support further studies, which could increase the accuracy of predictive models. Finally, the compatibility of different barrier materials should be carefully examined and may be optimized, especially the hydrolysis of ions that may be released and accumulated at the materials interfaces [9].

Case 2: Corrosion of B-25 steel containers containing grout encapsulated waste

Hot-rolled carbon steel is a potential material used for the construction of the B-25 containers that may be used for storing grout waste forms. This type of materials requires an internal and external protection with coatings to increase the corrosion protection. A destructive examination of a B-25 waste storage container, buried in a shallow non-radiological land burial facility for approximately 8 years, showed that pitting was the most prevalent form of corrosion and suggested that continued burial would result in through-wall pits after 30 years [10]. Figure 130 below shows images of large areas of macroscopic pitting corrosion on the lid surface.

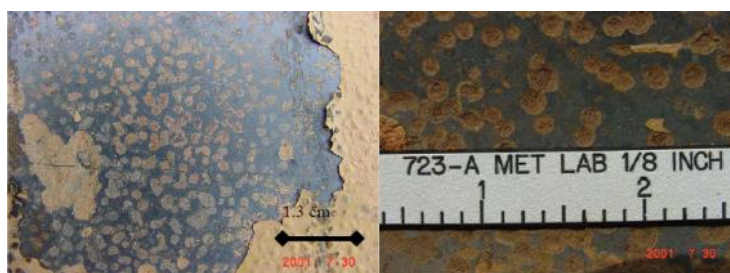


Figure 130. Large areas of macroscopic pitting on lid surface of B-25 container [10].

Corrosion of the lid, vertical walls, and bottom was present in varying degrees. Several areas were not affected at all by corrosion while others lost up to 30% of the wall thickness. This result suggests that through wall pits could provide a path for water flow into and out of similar B-25 containers after approximately 30 years of burial. The presence of chlorides in the surrounding environment may stimulate pit initiation and growth. However, the water extracted from the soil, around the excavated B-25, did not indicate unusually high concentrations of Cl⁻ ions. This suggests that the pits nucleated in the B-25 container because of local defects and/or weaknesses in the protective coating [10]. Figure 131 shows the presence of blistering in the protective coating that may lead with time to corrosion failure of the material. However, it must be noted these measurements were not performed in the Hanford subsurface, with little control and without constant monitoring.

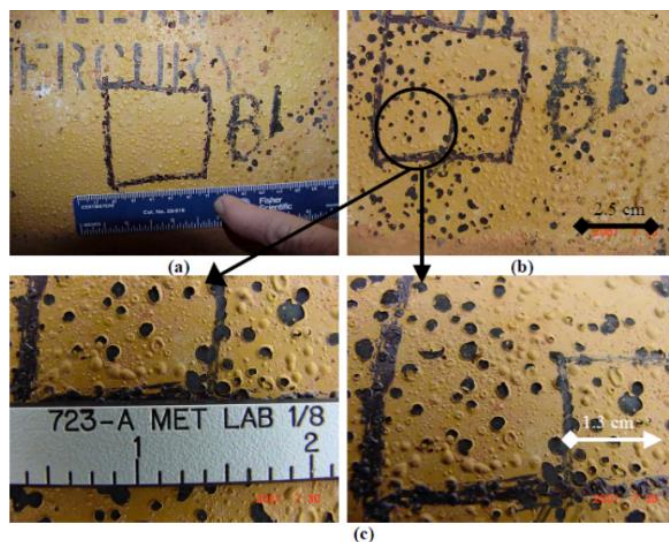


Figure 131. Coating blisters on the surface of B-25 container (a) Intact blisters, (b) broken blisters, (c) broken blisters showing intact primer [10].

Subtask 20.2.1: Conclusions

Research gaps were identified by reviewing relevant corrosion studies in this area and the main findings were summarized and reported here.

Currently, corrosion data of steel in site specific conditions of the IDF is very limited. Previous corrosion studies developed by Jenkins [1-2], in supposed Hanford burial condition, investigated the corrosion behavior of three different materials, HY-80 steel, 304 SS and Inconel alloy 600. A conservative prediction of the corrosion of the alloys in Trench 94 at Hanford was established through an evaluation of the behavior of the materials in other environments. This comparison was accomplished by using values for sites most similar in corrosivity to Trench 94 and normalizing the data to account for the differences in corrosivity between the test sites and Trench 94. The predicted data was normalized by using the resistivity value of the Hanford location and of the selected sites. Hence, no real site-specific data was obtained in this study [2].

Serne et al. (2016), developed a recipe to prepare Hanford IDF vadose zone pore water (VZP) for leaching tests [5]. This recipe will be used to simulate the Hanford IDF groundwater for bench-scale testing of various steel in this environment. This simulant is the current approximation of the infiltrating water that would reach the container/canister if the IDF surface barrier fails.

However, the most damaging and prevalent type of corrosive attack that is most likely to breach the container walls is localized corrosion. The main forms of this kind of attack of importance to nuclear waste problems are pitting, crevice corrosion, and others. Finally, selected cases of localized corrosion on canisters/containers of interest for this study were reported.

Subtask 20.2.1: References

1. Jenkins J.F. "Corrosion behavior of HY-80 steel, type 304 stainless steel, and Inconel alloy 600 at 218-E-12B burial ground, Hanford, WA". TR-2001-SHR. December 1993.

2. Jenkins, J F. "Naval civil engineering laboratory. Prediction of corrosion performance of submarine reactor compartments after burial at Trench 94, Hanford Washington". January 1992.
3. Lee K. Patrick. "Results for Hanford's integrated disposal facility performance assessment". Washington River Protection Solutions. TOC-PRES-18-4190. October 2018.
4. <https://www.osti.gov/biblio/1460055-field-scale-lysimeter-studies-low-activity-waste-form-degradation>
5. Serne R.J. et al. "Extended leach testing of simulated LAW cast stone monoliths". Pacific Northwest National Laboratory. RPT-SWCS-010, Rev. A. June 2016.
6. Marcus P. "Corrosion mechanisms in theory and practice". Taylor & Francis Group, 2012.
7. Roberge, P.R. "Handbook of Corrosion Engineering". McGraw-Hill, 1999.
8. Dhawan S.K. et al. "Corrosion Preventive Materials and Corrosion Testing". Taylor & Francis Group, LLC, 2020.
9. Guo X. Nature Materials. 310 (2020) 310-316.
10. Dunn K.A. "B-25 Corrosion evaluation summary report". WSRC-TR-2001-00587. Jan 2002.

Subtask 20.2.2: Development of a Test Plan and Initial Testing for the Steel Corrosion Study

Subtask 20.2.2: Methodology

A test plan for the corrosion study of various canister materials was developed in collaboration with engineers from PNNL. Table 18 below shows the test plan developed including candidate materials, test and description, as well as reason for the test.

Table 18. Test Matrix for Corrosion Study of Canister/Container Materials

	Test	Potentiodynamic Polarization		Corrosion Potential 7-28 day		Polarization Resistance during Ecorr		Post-corrosion Examination with SEM	
	Description	Provide Tafel plots, base corrosion rates, passive regions		Long term evolution of corrosion potential, can be extended if needed with intermittent monitoring		Measure surface resistance during Ecorr measurements to get estimate of corrosion rate evolution with time		Determine location of corrosion attack (grain boundaries) and mechanism (pitting vs general)	
Candidate Sample Type	Reason	GW A	GW B	GW A	GW B	GW A	GW B	GW A	GW B
SS 304	Glass container base material								
Heat Treated SS 304	Base canister material with glass poured within								
Welded SS304	Represent canister lid (weak point)								
Welded SS304 – Heat Treat	Represent canister lid (weak point) after heat cycle								
ASTM A-569-93 Carbon Steel	B-25 box steel type								
high carbon steel	Worst case scenario								
Hastelloy	Best case scenario for a container but expensive								
316 SS	55-gallon drum material								
409 SS	55-gallon drum material								

GW A and GW B: two representative Hanford groundwater simulants; SS: stainless steel

Specimen preparation and materials

A list of necessary materials and chemicals for the beginning of the corrosion tests was prepared and most of the items have been procured. The list of materials includes electrodes, corrosion cells, cables for connections, and others. Also, various chemicals have been procured for the testing. Most of the chemicals will be used to prepare a solution that will simulate the Hanford Integrated Disposal Facility (IDF) groundwater. This solution simulates the infiltrating water that would reach the containers/canisters if the IDF surface barrier fails.

Figure 132 shows a view of the glass vertical cell and a typical sample arrangement that will be used for the testing.

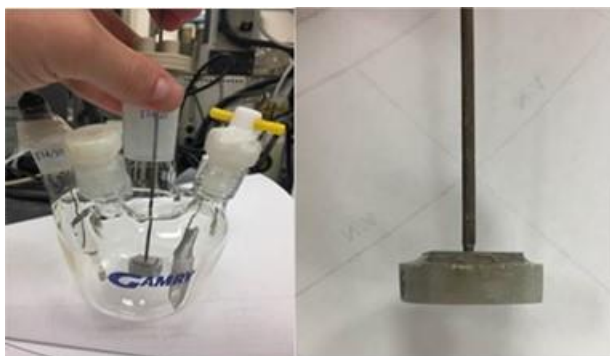


Figure 132. Experimental setup (left) and the sample (right) for electrochemical measures.

The specimen will be fixed in a cold resin that will allow only one side of the cylinder (bottom) to be in contact with the solution. The glass cell will be filled with the testing solution and the bottom surface of the sample will be immersed in the solution during the test. Some rubber stoppers for the glass cell were ordered.

FIU has procured some 304 stainless steel (SS) square bars and threaded 316 stainless steel rods for the preparation of the initial specimens. The material under study is the 304 SS. The 304 SS bar was cut to the dimensions of 0.75-inch height, 0.5-inch width and 0.5-inch thickness. The back of the sample was threaded, and a piece of 316 SS rod screwed to it to facilitate the electrical connection between the sample and the cables connected to the rod. Only the bottom area, squared section, of the 304 SS sample will be under study. The preparation of the samples was carried out at an FIU machine shop. The surface of the samples was prepared following recommendations by the Hanford site point of contact.

A three-electrode arrangement can be used to perform the electrochemical measurement. A reference electrode (saturated calomel), a working electrode (the 304 stainless steel sample) and the counter electrode (a platinum mesh) will be used. Several options of platinum mesh were identified and will be procured. The calomel reference electrode was recently procured.

Equipment for corrosion studies

A potentiostat was procured for electrochemical testing. The equipment was installed and connected to the computer through the VersaStudio software. In addition, FIU has been working on a design of a Faraday cage necessary for the electrochemical measurements. Figure 133 shows the schematic of the Faraday cage that will be manufactured.

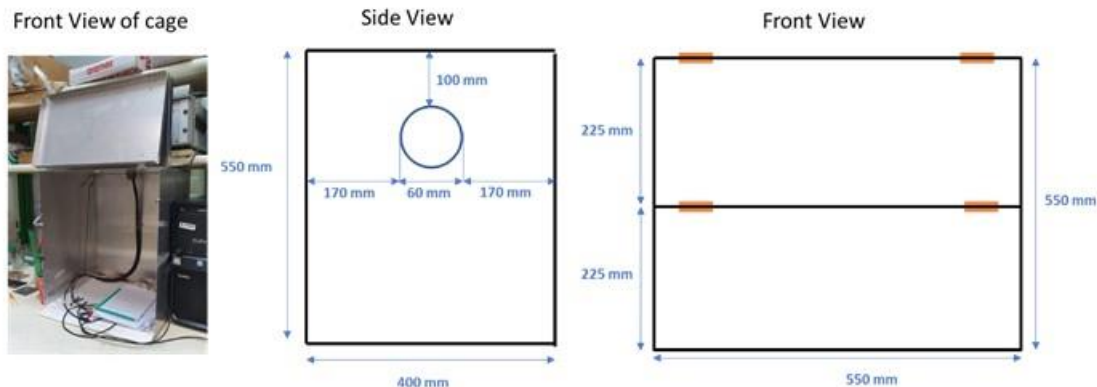


Figure 133. Schematic of the Faraday cage. Image of similar cage (left), Side view (middle) and front view (right).

The manufacture of the Faraday cage was completed, and it was placed in the lab next to the potentiostat.

Subtask 20.2.2: Results and Discussion

The experiments have not started and consequently there are no result at this time.

Subtask 20.2.2: Conclusions

FIU has prepared conditions in the lab for the beginning of the corrosion study of various canister/container materials. The equipment for the electrochemical measurements, as well as the materials and chemicals necessary for the testing were procured. Also, the software for the measurements was installed, and the setup of the equipment was performed. In addition, the test matrix for the evaluation of the materials' performance when exposed to the simulated IDF groundwater was prepared. FIU is currently working on the identification of counter electrodes necessary for the measurements.

CONFERENCE PARTICIPATION, PUBLICATIONS, AWARDS & ACADEMIC MILESTONES

Peer-reviewed publications

A. Awwad, D. McDaniel, L. Lagos, B. Tansel, "Aging characteristics of ethylene propylene diene monomer (EPDM) nonmetallic components used in caustic liquid waste transfer lines: effect of temperature and exposure time", Engineering Failure Analysis, (Accepted 7/21).

A. Baharanchi, J. Coverston, M. Poirier, D. McDaniel, "Numerical Simulation of High Level Waste Simulant Flushing in Pipelines", Fluids - MDPI (under review).

Oral and Poster presentations (presenter is underlined)

M. Boan, R. Ocampo (DOE Fellow), L. Lagos, D. McDaniel. "Accelerated Aging of Concrete for the Study of Coatings to Protect the Aged Walls of the HCAEX Tunnel at Savannah River" Paper 21245 (Oral presentation). Waste Management 2021 Virtual Conference, Phoenix, AZ, March 2021.

M. Telusma, J. Natividad (DOE Fellow), L. Lagos, D. McDaniel, "Development of an Omnidirectional Wall Crawling Mobile Platform Designed to Aid in the Repair of H-Canyon's Concrete Walls", Proceedings of the Waste Management Symposia 2021, Phoenix, AZ, March 7-12 2021.

D. Martin, S. Tashakori, L. Lagos, D. McDaniel, "Development and Testing of a Miniature Inspection Tool for Hanford DST's", Proceedings of the Waste Management Symposia 2021, Phoenix, AZ, Mach 7-12 2021.

M. Thompson, D. McDaniel, B. Wiersma, A. Aravelli, "Structural Health Monitoring Technologies for Wear and Anomaly Detection in Nuclear Waste Transfer System", Proceedings of the Waste Management Symposia 2021, Phoenix, AZ, Mach 7-12 2021.

WM Student Posters

Jeff Natividad: Collaboration for Improving Safety and Efficiency: Guidance for Autonomous Robotics Use at Hanford (21438)

Joel Adams: Autonomous Surveillance of Nuclear Facility and Repositories (21435)

Raymond Piloto: Flow-Induced Erosion Detection in Stainless-steel Coupons from SRNL (21423)

Sebastian Story: Inspection rover for Leak Detection Channels within Double-Shell Tanks at the Hanford Site (21436)

Awards

Best Poster Presentation and Paper-ASME AWARD. M. Echeverria Boan, A. Nunez Abreu, L. Lagos, D. McDaniel. "Aging of Concrete for the Evaluation of Repair Materials to Protect the Walls of the HCAEX Tunnel at Savannah River". Waste Management 2021 Virtual Conference, Phoenix, AZ, March 2021.

Academic Milestones

Christopher Excellent (DOE Fellow) graduated with B.S. degree in Mechanical Engineering in Fall 2020.

DOE Fellow Brendon Cintas graduated with B.S. degree in Mechanical Engineering in Spring 2021 and continued to pursue a Ph.D. in Mechanical Engineering at FIU.

ACKNOWLEDGEMENTS

Funding for this research was provided by U.S. DOE Cooperative Agreement #DE-EM0005213. FIU's Applied Research Center would like to acknowledge the commitment of DOE-EM to this Chemical Process Alternatives for Radioactive Waste project and to all the research being conducted as part of the Cooperative Agreement. The partnership between DOE EM and FIU has resulted in the development and training of outstanding minority STEM students that will benefit this country as a whole.

APPENDIX

The following documents are available at the DOE Research website for the Cooperative Agreement between the U.S. Department of Energy Office of Environmental Management and the Applied Research Center at Florida International University: <https://doeresearch.fiu.edu>

FIU Year 1 Annual Research Review Presentations:

1. FIU Research Review - Project 1
2. FIU Research Review - Project 2
3. FIU Research Review - Project 3 – D&D
4. FIU Research Review - Project 3 – IT ML
5. FIU Research Review - Project 4 & 5
6. FIU Research Review - Project 4 - DOE Fellow Aurelien Meray
7. FIU Research Review - Project 4 - DOE Fellow Gisselle Gutierrez
8. FIU Research Review - Project 4 - DOE Fellow Jeff Natividad
9. FIU Research Review - Project 4 - DOE Fellow Mariah Doughman
10. FIU Research Review - Project 4 - DOE Fellow Philip Moore
11. FIU Research Review - Project 4 - DOE Fellow Sebastian Story
12. FIU Research Review - Project 5 - DOE Fellow Eduardo Rojas
13. FIU Research Review - Project 5 - DOE Fellow Olivia Bustillo
14. FIU Research Review - Wrap Up - Project 1
15. FIU Research Review - Wrap Up - Project 2
16. FIU Research Review - Wrap Up - Project 3 – D&D
17. FIU Research Review - Wrap Up - Project 3 – IT ML
18. FIU Research Review - Wrap Up - Project 4
19. FIU Research Review - Wrap Up - Project 5